Ocean biogeochemistry in the coupled ocean-sea ice-biogeochemistry model FESOM2.1-REcoM3

Özgür Gürses[1], Laurent Oziel[1], Onur Karakuş[1], Dmitry Sidorenko[1], Christoph Völker[1], Ying Ye[1], Moritz Zeising[1], and Judith Hauck[1]

[1]Alfred-Wegener-Institut, Helmholtz-Zentrum für Polar- und Meeresforschung

Correspondence: Özgür Gürses (ozgur.gurses@awi.de)

Abstract.

The cycling of carbon in the oceans is affected by feedbacks driven by changes in climate and atmospheric CO_2. Understanding these feedbacks is therefore an important prerequisite for projecting future climate. Marine biogeochemical models are a useful tool there, but as any model is a simplification, need to be continually improved. In this study, we coupled the
5   Finite-volumE Sea ice-Ocean Model (FESOM2.1) to the Regulated Ecosystem Model version 3 (REcoM3). FESOM2.1 is an update of the Finite Element Sea ice-Ocean Model (FESOM1.4) and operates on variable mesh resolution. Unlike standard structured-mesh ocean models, the mesh flexibility allows for a realistic representation of small-scale dynamics in key regions at affordable computational cost. Compared to the previous coupled model version FESOM1.4-REcoM2, the model FESOM2.1-REcoM3 utilizes a new dynamical core based on a finite volume discretization instead of finite elements, but
10   retains central parts of the biogeochemistry model. As a new feature, carbonate chemistry including water vapor correction is computed by mocsy-2.0. Moreover, REcoM3 has an extended food web that includes macrozooplankton and fast-sinking detritus. Dissolved oxygen is added as a new tracer. In this study we assess the ocean and biogeochemical state simulated with FESOM2.1-REcoM3 in a global setup at relatively low spatial resolution forced with JRA55-do atmospheric reanalysis. The focus is on the recent period 1958-2021, to assess how well the model can be used for present-day and future climate
15   change scenarios on decadal to centennial timescales. A bias in global ocean-atmosphere preindustrial CO_2 flux present in the previous model version FESOM1.4-REcoM2 could be significantly reduced. In addition, the computational efficiency is 2–3 times higher than that of FESOM1.4-REcoM. Overall, it is found that FESOM2.1-REcoM3 is a skillful tool for ocean biogeochemical modelling applications.

1   Introduction

20   There is an unequivocal consensus and concern about the effects of increasing greenhouse gases in the atmosphere due to human activities. Since the beginning of the preindustrial era, 1750, the concentration of carbon dioxide (CO_2) in the air has substantially risen from 277 ppm to 417.2 ppm in 2022 (Friedlingstein et al., 2022b). The ocean took up anthropogenic carbon at a rate of 2.9 PgC yr^{-1} (26% of total CO_2 emissions) in 2021 (Friedlingstein et al., 2022b). Simultaneously, the terrestrial CO_2 sink is estimated to be 3.5 PgC yr^{-1}. The total air-to-land CO_2 flux is, however, lower by 1.1 PgC yr^{-1} because of

25 emissions from land-use change, mainly deforestation. The ocean carbon sink has grown over the past decades in response to the near-exponential rise in CO_2 emissions (Friedlingstein et al., 2022b). While the global ocean carbon sink estimate is assigned an uncertainty of 0.4 PgC yr^{-1} and medium confidence, regional patterns of the sink differ more strongly. This points to the balance between physical and biological processes, which are more difficult to model as also illustrated in model deficiencies of the seasonal cycle of pCO_2 and CO_2 fluxes (Mongwe et al., 2018). Both climate change and rising atmospheric

30 CO_2 feed back on the fraction of CO_2 emissions that will end up in the ocean over the next century (Friedlingstein et al., 2003; Canadell et al., 2021). Models are important tools in estimating how large these feedbacks are.

The flux of CO_2 between atmosphere and ocean is controlled by two main mechanisms: the solubility pump and the biological pump. The solubility pump describes the air-sea CO_2 exchange that occurs to satisfy a thermodynamic equilibrium, and the subsequent transport of carbon from the surface to the deep ocean with the overturning circulation. This leads to CO_2

35 uptake at mid- to high latitudes through high solubility in cold waters and large vertical motion in deep water formation regions. In contrast, warm ocean regions in the tropics and subtropics as well as upwelling regions lose carbon to the atmosphere (Takahashi et al., 2009; Wanninkhof et al., 2013). The solubility pump is responsible for anthropogenic carbon uptake. The biological carbon pump comprises the fixation of CO_2 into biomass by phytoplankton and the subsequent downward transfer of dead organic material (Boyd et al., 2019). The biological carbon pump is responsible for 75% of the natural vertical carbon

40 gradient (Sarmiento and Gruber, 2006), and for the large-interbasin gradient between the deep Pacific and Atlantic. Without the biological carbon pump, atmospheric CO_2 would be higher by 200 ppm (Maier-Reimer et al., 1996), and perturbations thereof can have large effects on atmospheric CO_2 (Kwon et al., 2009; Lauderdale and Cael, 2021) as also known from paleo evidence (Galbraith and Skinner, 2020).

Global ocean biogeochemistry models (GOBMs, Fennel et al., 2022) are used to assess the global ocean carbon sink (Hauck

45 et al., 2020), its regional patterns (Fay and McKinley, 2021), and effects of climate change and variability on the ocean carbon sink (Le Quéré et al., 2010; Hauck et al., 2013; DeVries et al., 2019; Bunsen, 2022). By their representation of pH, the marine oxygen cycle and phytoplankton primary production as the base of the marine food web, they also offer information about the environmental conditions for marine life and how these will develop under climate change (Bopp et al., 2013; Laufkötter et al., 2015; Kwiatkowski et al., 2020). One such ocean biogeochemistry model is the Regulated Ecosystem Model (REcoM)

50 that describes the lower trophic levels of the marine ecosystem using the plankton functional type approach, and that bases its description of primary production on a physiological model for phytoplankton growth that takes into account nutrient availability effects on photoacclimation (Geider et al., 1998) and, for diatoms, on the relative frustule weight (Hohn, 2009). One specificity of REcoM is the representation of flexible stoichiometry, which leads to a description of elemental fluxes that can deviate from the fixed Redfield ratios often used in models (Redfield et al., 1963).

55 Modeling the marine biogeochemistry of the ocean is subject to several sources of uncertainties: First, GOBMs are expensive with respect to the computational cost due to the advection of a large number of tracers and therefore, often demand low spatial resolution. This leads to deficiencies in the representation of significant physical processes such as (sub)mesoscale currents (McWilliams, 2016) which can have large impacts on transport and mixing processes that strongly affect biological productivity (Lévy et al., 2018; Keerthi et al., 2022). Second, the descriptions of ecological interactions and of the physiology of primary

60   and secondary producers in GOBMs are still mostly based on empirical or semi-empirical mathematical descriptions, such as
e.g., the dependency of zooplankton grazing rates on prey abundance (Doney et al., 2001; Rohr et al., 2022). These contain a
large number of parameters that are only partly constrained from observations, making it necessary to tune these parameters in
GOBMs to some extent. Choices in these parameters can have strong effects on the biological carbon pump (e.g. Lauderdale
and Cael, 2021). It has been demonstrated that the largest source of uncertainty for projections of net primary production (NPP,
65   Tagliabue et al., 2021) comes from model uncertainty, not scenario uncertainty (Frölicher et al., 2016).

Ocean circulation models formulated on unstructured meshes have become an alternative to existing structured global ocean
models (Danilov, 2013). The Finite-Element Sea ice–Ocean Model (from now on FESOM1.4, Wang et al., 2014) is one of
the first global models with multiple resolutions designed to simulate the large-scale ocean circulation. While it has already
been used in numerous applications (Sidorenko et al., 2015; Wekerle et al., 2017), another dynamical core, the Finite-volumE
70   Sea ice-Ocean Model version 2.1 (FESOM2.1), has been developed (Danilov et al., 2017). The advantages of a finite volume
formulation are (a) better throughput and scalability as a result of a more efficient data structure (Koldunov et al., 2019), (b) the
availability of clearly defined fluxes, and (c) the possibility to choose from a selection of transport algorithms, which was very
limited before (Danilov et al., 2017). Furthermore, the arbitrary Lagrangian Eulerian (ALE) vertical coordinate is introduced
which provides different types of vertical coordinates (Scholz et al., 2019).

75   Here we document the ocean biogeochemistry in the Regulated Ecosystem Model version 3 (REcoM3) coupled to the ocean
and sea ice model FESOM2.1, and assess its performance in reproducing carbon and nutrient biogeochemical fluxes as well as
the distribution of phytoplankton and zooplankton. Our aim is to analyze the new setup regarding the coupled model state under
historical atmospheric CO_2 forcing and the associated model bias and drift from the experiment with constant preindustrial
(PI) CO_2 level. We thus focus on evaluating model aspects with regard to the effects of climate change and CO_2 increase on
80   carbon fluxes on century-scale time-scales. We exclude in our analysis the deep-sea distribution of carbon and nutrients, which
would require model runs over at least 500 to two thousand years (Séférian et al., 2020), which will be done in follow-up work.

2   Methods

2.1   Model Description

We present the coupled ocean-sea ice-biogeochemistry model FESOM2.1-REcoM3. The previous model version FESOM1.4-
85   REcoM2 has been described by Schourup-Kristensen et al. (2014). Unlike its predecessor FESOM1.4 which uses a finite
element formulation, the ocean model is now based on a finite volume discretization, which makes tracer conservation much
easier to achieve. FESOM2.1 was described by Danilov et al. (2017) and evaluated in Scholz et al. (2019, 2021). The ocean
biogeochemistry is simulated by the Regulated Ecosystem Model version 3 (REcoM3), which builds upon the previous version
REcoM2 (Hauck et al., 2013; Schourup-Kristensen et al., 2014). The advection and diffusion of 28 passive biogeochemical
90   tracers is handled by FESOM2.1, whereas REcoM3 calculates sources and sinks, driven by biological interactions or biogeo-
chemical exchange processes.

2.1.1 Ocean Model FESOM2.1

FESOM2.1 solves the hydrostatic primitive equations under the Boussinesq approximation (Danilov et al., 2017). This equation set in differential form is discretized on a finite set of points (nodes). As a first step of mesh generation, a 2-dimensional grid is created by combining these nodes in triangular shapes (elements). At this stage, mesh resolution (i.e., the size of triangles) can be adjusted in areas of interest without requiring a nesting approach. A 3-dimensional mesh is produced by projecting triangles in vertical direction forming prisms. The scalar quantities (tracers, pressure) are located at nodes while the horizontal velocities are defined at centroids of elements (See Figs. 1 and 2 in Danilov et al., 2017). A pair of control volumes are defined. The vector control volumes are the prisms based on elements. The scalar control volumes are formed by connecting cell centroids with edge midpoints (Fig. 1). Integration is carried out on a staggered Arakawa B type of mesh (Scholz et al., 2019).
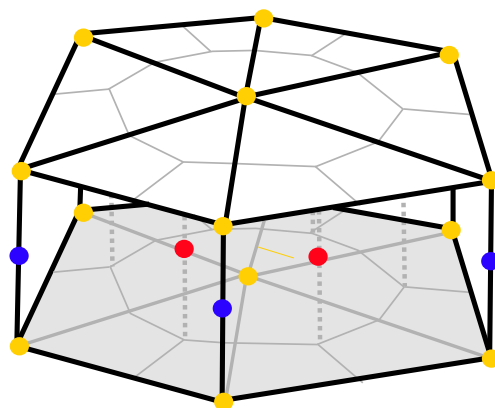
Figure 1. Scheme of the cell-vertex discretization in 3-dimensional space. Blue dots correspond to scalar quantities including REcoM2 state variables, located at the mid-layer vertices of triangles. Red dots represent horizontal velocities located at mid-layer cell centers of the triangles. Yellow dots depict vertical transfer velocities, placed at the layer boundaries aligned with scalar quantities in vertical.

We use FESOM2.1, an updated version of FESOM2.0. The updated model features include several developments, such as parallel and asynchronous output writing. An important new feature that we applied is the kinematic backscatter parameterisation. This method takes into account the scales at which energy is scattered back to the resolved flow by introducing a negative viscosity term (Juricke et al., 2020). This greatly improves the simulation of eddy effects in coarse resolution mesh setups (Juricke et al., 2020). The model code also includes representation of ice-shelf cavities (Timmermann et al., 2012), which has been used in regional studies with FESOM1.4-REcoM2 (Nissen et al., 2022). Ice-shelf cavities are, however, not used in this study. Isoneutral tracer diffusion (Redi, 1982) and the Gent-McWilliams (GM, Gent and McWilliams, 1990; Griffies, 1998) eddy stirring parameterization are applied. Both GM and Redi are scaled with horizontal resolution with a maximum value of 2000 m^2 s^{-1} at 100 km horizontal resolution, and decrease linearly below a resolution of 40 km to reach zero at 30 km resolution effectively switching the parameterization. As vertical mixing parameterization, the K-profile scheme is used (KPP, Large et al., 1994) with a background vertical diffusivity of 1 x 10^{-4} m^2 s^{-1} for momentum and 1 x 10^{-5} m^2 s^{-1} for tracers.

Furthermore, the Monin-Obukhov length dependent vertical mixing parameterization is applied in the surface boundary layer south of $50°$S (Timmermann and Beckmann, 2004).

Regarding the vertical discretization, FESOM2.1 is formulated with an arbitrary Lagrangian-Eulerian (ALE) scheme, a syn-
thesis of different types of vertical coordinates. In the model configuration used here, we apply a full free-surface formulation and thus permit the vertical movement of the surface and of all other layers (referred to as zstar, Scholz et al. (2019)). This dras-
tically improves tracer conservation properties (Campin et al., 2004). Partially filled cells are used at the ocean floor resulting in a smoother representation of the bathymetry.

The sea ice component (Finite-Element Sea Ice Model, FESIM version 2) solves for sea ice concentration, ice and snow
thickness, as well as ice drift velocity (Danilov et al., 2015). It is discretized on the same unstructured horizontal mesh as the ocean model. The elastic-viscous-plastic solver and flux corrected transport scheme are used for sea ice advection (Danilov et al., 2015). The formulation of sea ice thermodynamics follows the work of Timmermann et al. (2009).

2.1.2 Biogeochemistry Model REcoM3

REcoM3 is a water column biogeochemistry and ecosystem model which incorporates cycles of carbon and nutrients (ni-
trogen, iron, and silicon) with varying intracellular stoichiometry in phytoplankton, zooplankton and detritus (see Appendix for detailed description and equations). Starting from the work by Schartau et al. (2007), REcoM was first used to describe carbon overconsumption in mesocosm experiments. After coupled to the ocean and sea ice model MITgcm (Marshall et al., 1997), the previous version (REcoM2) with two phytoplankton classes, one zooplankton and one detritus class was applied to study the cycling of marine carbon on present (Hauck et al., 2013, 2018) and glacial time-scales (Du et al., 2022; Völker
and Köhler, 2013), as well as the marine iron cycle (e.g., Völker and Tagliabue, 2015; Tagliabue et al., 2016; Ye and Völker, 2017; Pagnone et al., 2019). Moreover, REcoM2 was employed in assessments on the efficiency of ocean alkalinity enhance-
ment (Köhler et al., 2013; Hauck et al., 2016), in data assimilation studies (Pradhan et al., 2019) and as a test bed for model development, e.g., for development of a parameterization of iron-ligand binding based on pH (Ye et al., 2020) among others. Simultaneously, REcoM2 was coupled to FESOM1.4 (Schourup-Kristensen et al., 2014). These coupled model set-ups were
used either in a global configuration (e.g., Schourup-Kristensen et al., 2014; Hauck et al., 2020) with a regional focus on the Arctic or the Antarctic (Hauck et al., 2015; Schourup-Kristensen et al., 2018; Oziel et al., 2022; Nissen et al., 2022) or in regional configurations (Taylor et al., 2013; Losch et al., 2014). Recently, the model has matured to include two groups of each classes of phytoplankton, zooplankton and detritus (REcoM3, Fig. 2).

Marine primary production is computed through representation of two phytoplankton functional types (PFTs), namely di-
atoms and small phytoplankton. The diverse group of small phytoplankton comprises a wide range of taxa, including, for instance, non-silicifying and calcifying and non-calcifying haptophytes and green algae. The model allows PFTs to adapt their internal stoichiometry (C:N:Chl:$CaCO_3$ ratios for small phytoplankton and C:N:Chl:Si for diatoms) to nutrient levels, ambi-
ent light and temperature, based on the photoacclimation model by Geider et al. (1998). Si uptake by diatoms is regulated as well, based on the internal Si:N quota, following Hohn (2009). This parameterization takes into account the strong decoupling
between Si and N metabolism (e.g., Claquin et al., 2002), and prescribes the observed change in Si:N ratios under Fe and
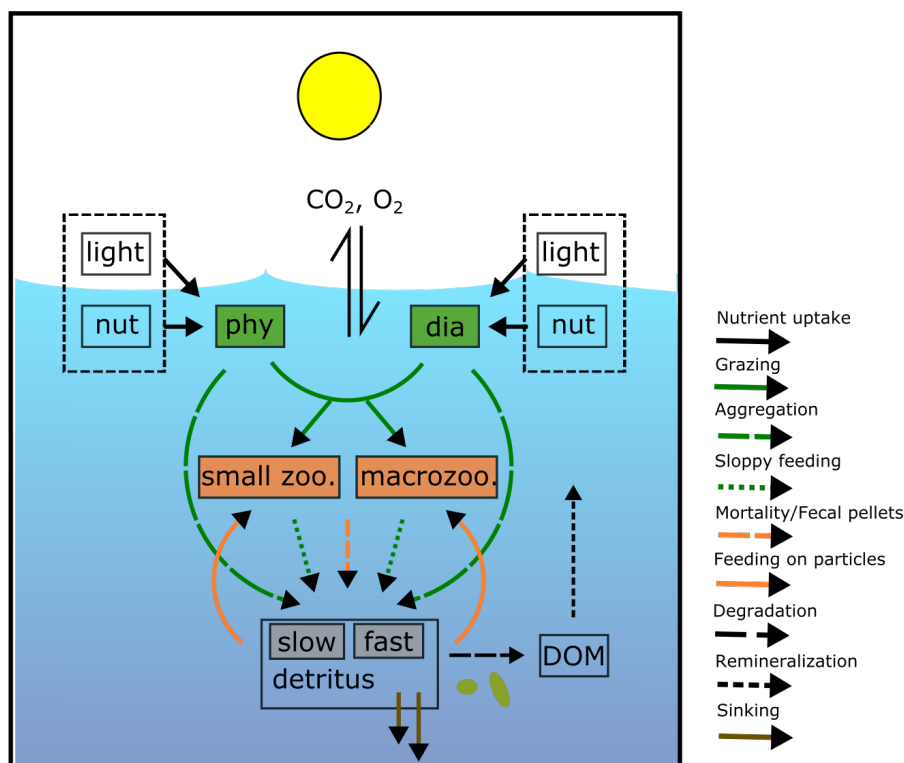
Figure 2. Schematic diagram of the components and interactions in the REcoM3 model. Small phytoplankton (phy) and diatoms (dia) take up inorganic nutrients (nut). Small zooplankton (small zoo.) and macrozooplankton (macrozoo.) consume phytoplankton and particles. Macrozooplankton feeds on small zooplankton. Phytoplankton aggregation, zooplankton sloppy feeding, mortality and fecal pellets generate sinking detritus (slow and fast). Sinking detritus degrades to dissolved organic carbon and nitrogen. Dissolved organic material (DOM) then remineralizes to dissolved inorganic carbon and nitrogen. The number of tracers and the other processes are shown in the appendix (Fig. A2).

N limitation. The intracellular iron pool is derived from intracellular nitrogen with a fixed Fe:N ratio, based on the fact that intracellular iron is mostly associated with the photosynthetic electron transport chain and nitrogen metabolism (Geider and La Roche, 1994; Raven, 1988). REcoM3 also includes the photo-damage parameterization by Álvarez et al. (2018). Calcium carbonate production is assumed to be linearly dependent on the gross small phytoplankton production. $CaCO_3$ dissolution is
150   described by a depth-dependent dissolution rate.

     Zooplankton is represented by two groups, small zooplankton and polar macrozooplankton (Karakuş et al., 2021) and each group has a carbon and a nitrogen tracer. The small zooplankton group in the model is associated with relatively higher grazing rates compared to macrozooplankton and is widely spread in the global ocean. The polar macrozooplankton is mainly present in the Southern Ocean and northern high latitudes. The respiration rate is described mechanistically for macrozooplankton taking
155   into account reduced metabolism in winter and increased metabolism at high grazing rates (Karakuş et al., 2021). For small zooplankton, respiration is calculated with a fixed respiration rate constant and biomass in contrast to the previous version

REcoM2 where respiration was used to drive zooplankton C:N back towards Redfield ratio (Hauck et al., 2013; Schourup-Kristensen et al., 2014). Grazing is computed by applying a sigmoidal function with variable preferences on both phytoplankton and detritus (Fasham et al., 1990).

160   Particulate organic matter (detritus) is split into two groups. The sinking speed of the first detritus group increases linearly with depth (from 20 m day^{-1} from the surface to 192 m day^{-1} at 6000 m depth; Kriest and Oschlies, 2008). The sinking speed of the second group (fast-sinking detritus) is constant throughout the water column (200 m day^{-1}, Karakuş et al., 2021). Remineralisation of carbon and nitrogen occurs in two steps. Detrital material is first degraded to dissolved organic matter and then remineralised to the inorganic forms (dissolved inorganic carbon and nitrogen, DIC, DIN). For iron, it is assumed that the
165   organic form is directly bioavailable, so it enters the dissolved iron pool in one step.

    REcoM3 comprises a single-layer sediment pool for nitrogen, silicon, dissolved inorganic carbon and calcium carbonate. The sinking detritus and associated minerals are accumulated in this layer when they reach the ocean floor. This material is subsequently returned back to the water column to the pools of dissolved inorganic nitrogen, carbon and silicon, as well as alkalinity with a fixed remineralisation rate. The release of iron to the bottom layer of the ocean is assumed to be proportional
170   to the release of inorganic nitrogen (Elrod et al., 2004).

2.1.3   Updates to previous REcoM version coupled to FESOM1.4

There are numerous improvements relative to the previously documented version FESOM1.4-REcoM2 (Schourup-Kristensen et al., 2014), and the main changes are listed below:

REcoM

175   1. The routines for calculating carbonate chemistry and air-sea CO_2-exchange used in FESOM1.4-REcoM2 which followed the guidelines provided by the Ocean Carbon Model Intercomparison Project (Orr, 1999) were replaced by the mocsy-2.0 scheme of Orr and Epitalon (2015). While both use the same thermodynamic equilibrium to calculate surface pCO_2 and CO_2 flux, mocsy-2.0 uses the faster and more accurate algorithm SolveSAPHE (Munhoven, 2013). Among other differences, it follows best practice guides and uses recommended equilibrium constants. The gas exchange formu-
180   lation is updated to Wanninkhof (2014), which is largely equivalent to Ho et al. (2006). The computed fluxes are scaled with the ice-free area.

  2. Dissolved oxygen was added as a new tracer in REcoM3. The air-sea O_2 flux is calculated using the mocsy-2.0 routines (Orr and Epitalon, 2015). Photosynthesis, respiration and remineralisation change oxygen with a fixed O_2:C ratio, and remineralisation does not depend on O_2 levels in the current model version.

185   3. A second zooplankton group and a fast-sinking detritus class were added. The second zooplankton group represents a slow-growing polar macrozooplankton with a feeding preference on diatoms which produces fast-sinking and carbon-rich fecal pellets (Karakuş et al., 2021).

4. Intracellular iron concentration is connected to intracellular nitrogen via a constant ratio Fe:N leading to some variation in the Fe:C ratio, as briefly presented in Tagliabue et al. (2016) and Pagnone et al. (2019).

5. Sedimentary release of iron was added to the model (Tagliabue et al., 2016), in addition to the previously considered Fe input with dust deposition.

FESOM

Biogeochemical fluxes returned back to the ocean from the benthos are treated with a specific bottom boundary condition. Variable bottom topography leads to a smaller scalar control volume located at the lowermost level. This is because scalar control volumes are obtained by connecting the areas from the elements they are attached a constant level (see Fig. 1 in Danilov et al., 2017). Therefore, the number of elements around a single surface node may vary with depths when it meets non-flat topography. We thus computed the control volume and associated fluxes for each node by considering all surrounding elements at different depth levels.

Forcing

Our simulation was forced by the atmospheric reanalysis JRA55-do data set (Tsujino et al., 2018) instead of the CORE-II data set (Large and Yeager, 2009) that was used in previous assessments (Schourup-Kristensen et al., 2014). JRA55-do is a blend of reanalysis data and satellite observations and has the advantage to provide regularly updated near real time data up to present day with higher temporal (3-hourly) resolution.

2.2 Experimental setup and data

In this study, we used a mesh with a nominal resolution of 1 degree as a background. The horizontal resolution is enhanced on the equatorial belt and in the region north of 50°N to match 1/3 degree and 25 km, respectively. The mesh has 48 unevenly spaced vertical layers where the layer thickness ranges from 5 m in the surface to 250 m in the deep ocean (Scholz et al., 2019).

Initial fields for temperature and salinity were taken from the Polar Science Center Hydrographic Climatology (PHC3, updated from Steele et al., 2001). Total alkalinity (Alk) and preindustrial dissolved inorganic carbon (DIC) were initialized from version 2 of the Global Ocean Data Analysis Project (GLODAPv2) data set (Lauvset et al., 2016). Dissolved inorganic nitrogen (DIN) and dissolved silicic acid (DSi) were started with values from the Levitus World Ocean Atlas climatology of 2013 (Garcia et al., 2014). We used the Levitus World Ocean Atlas climatology of 2018 for dissolved oxygen (Garcia et al., 2019a) (See Table 2).

Due to scarcity of observations, the iron field (DFe) was initialized with output from the Pelagic Interaction Scheme for Carbon and Ecosystem Studies (PISCES) model (Aumont et al., 2003) which was corrected using observed profiles for the Southern Ocean (de Baar et al., 1999; Boye et al., 2001). Sensitivity tests indicated that high values stemming from a hydrothermal vent in the Eastern Equatorial Pacific lead to unreasonably large values in the interior Pacific Ocean due to advective fluxes. Therefore, the region spanning the latitudes of 12.5°S - 9.5°N, longitudes 72°W - 106°W was masked to a maximum value of 0.3 μmol m^{-3} (below 2000 m). All other tracers were initialized with small values.

220   Iron was supplied to the ocean by dust deposition and from sediments. The sedimentary flux was assumed to scale with organic nitrogen flux into the sediment, as found in Elrod et al. (2004). REcoM3 used monthly averages of dust deposition (Albani et al., 2014). We assumed that 3.5% of the dust field consists of iron of which 1.5% dissolves into a bio-available form when deposited in the surface ocean. We did not include aeolian nitrogen deposition in our simulations.

Table 1. List of simulations performed in this study.

Experiment	Period	Atmospheric CO_2	Atmospheric Forcing
pre-spinup	1611 – 1799	constant (278 ppm)	RYF61
A_{spinup}	1800 – 1957	increasing	RYF61
B_{spinup}	1800 – 1957	constant (278 ppm)	RYF61
A	1958 – 2021	increasing	JRA55-do
B	1958 – 2021	constant (278 ppm)	RYF61

The atmospheric reanalysis data sets of JRA55-do v.1.5.0 (Tsujino et al., 2018) were used to force the model for the period
225   1958-2021 (hereafter, JRA55-do). A single repeating annual cycle of all forcing fields (year 1961) was used to perform the spinup simulations and a control experiment. This is referred to as Repeat Year Forcing (hereafter called RYF61). We have deliberately chosen the year 1961 as it had rather neutral El Niño conditions and further contained a low amount of anthropogenic perturbation as compared to the years 1990 and 1991 recommended by Stewart et al. (2020).

A series of experiments was carried out in a global setup to investigate the performance of the coupled FESOM2.1-REcoM3
230   model. The experiments follow the definitions used in the Global Carbon Budget (Friedlingstein et al., 2022a) and in the RECCAP (Regional Carbon Cycle Assessment and Processes, https://reccap2-ocean.github.io/) projects and are summarized in Table 1. Our first experiment was forced with varying climate from the JRA55-do data set, and varying atmospheric CO_2 levels (hereafter referred as A). Atmospheric CO_2 mixing ratio (xCO_2) values are taken from the Global Carbon Budget (Joos and Spahni, 2008; Ballantyne et al., 2012; Friedlingstein et al., 2022a). A second simulation was forced by RYF61
235   atmospheric reanalysis fields and a preindustrial atmospheric CO_2 mixing ratio of 278 ppm. This configuration, here termed as B, is considered as the control run. Using these two simulations, the global ocean anthropogenic CO_2 sink was estimated by taking the model biases and drift from the control run into account. We used a coupled system spinup (i.e., a direct strategy, Séférian et al., 2016). Before starting simulations A and B, we performed spinup experiments in two stages. In the first stage, a 189-year long (equivalent to three cycles of JRA55-do forcing) preindustrial spinup simulation (named as pre-spinup) was
240   conducted using RYF61 atmospheric forcing and a preindustrial atmospheric CO_2 mixing ratio of 278 ppm until the air-sea CO_2 reaches a quasi-equilibrium state. The A_{spinup} and B_{spinup} simulations are a continuation of the pre-spinup simulation with either increasing (A_{spinup}) or constant (B_{spinup}) atmospheric CO_2 and run from 1800–1957. From the spinup simulations, A and B were branched off in 1958 and run until the end of 2020. FESOM1.4-REcoM2 and FESOM2.1-RECOM3 reach a throughput of 6 simulated years per day (SYPD) and 16 SYPD using the same mesh configuration and the same experimental
245   setup (See Table 1) on 288 cores with time steps of 15 min and 45 min, respectively. All modelled mean fields shown in this work are averaged over the period 2012–2021 unless stated otherwise.

Table 2. List of the observational data sets used to initialize the model and assess its performance.

Data set	Variable name	Unit	Reference
Dissolved inorganic carbon	DIC	mmol m^{-3}	Global Ocean Data Analysis Project version 2 (Lauvset et al., 2016)
Total Alkalinity	Alk	mmol m^{-3}	Global Ocean Data Analysis Project version 2 (Lauvset et al., 2016)
Dissolved inorganic nitrogen	DIN	mmol m^{-3}	World Ocean Atlas (Garcia et al., 2019a)
Dissolved inorganic silicon	DSi	mmol m^{-3}	World Ocean Atlas (Garcia et al., 2019a)
Oxygen	O$_2$	mmol m^{-3}	World Ocean Atlas (Garcia et al., 2019b)
Chlorophyll a concentration	Chl	mg m^{-3}	OC-CCI (Sathyendranath et al., 2019) and
			Southern Ocean (Johnson et al., 2013)
Net primary production	NPP	mmol m^{-3}	CPBM (Westberry et al., 2008) and
			VGPM (Behrenfeld and Falkowski, 1997)

3 Results and discussion

In this section we assess the performance of FESOM2.1-REcoM3 in simulating the observed mean state of nutrients, chlorophyll a, net primary production, and export production in the near-surface ocean as well as air-sea CO_2 flux primarily under
250 elevating CO_2. Before assessing the biogeochemical variables, we analyze key features of the ocean model.

3.1 Modelled hydrography, mixed layer and Atlantic meridional overturning

An extended analysis of analogous FESOM runs is presented in Scholz et al. (2019, 2021). Here we analyze only a few relevant diagnostics to prove the validity of the presented research. We start the analysis by inspecting the spatial distribution of the model bias in surface hydrography, presented in Fig. 3 as the difference between modeled mean 2012-2021 and the PHC3
255 Climatology (Steele et al., 2001). In the northern North Atlantic the bias is expressed by the cold (~4°C colder) and fresh (~1 psu fresher) anomalies around Newfoundland which is the typical bias for standalone and climate models at coarse resolutions (see e.g., Scaife et al., 2011). Further south, the bias depicts a dipole anomaly associated with the Gulf Stream going too far north, which is a commonly addressed shortcoming for non-eddy-permitting models (see e.g., Zhang and Vallis, 2007; Storkey et al., 2018). Similar issues are found in comparable current systems, such as the Kuroshio and Malvina systems. It is, however,
260 surprising that in general FESOM is far too saline at the surface being on average 0.3 psu saltier than the climatology.

The differences in surface hydrography between runs A and B is shown in the lower panels of Fig. 3. These are on average smaller than the bias to climatology but depict large scale patterns. In most of the ocean the SST and SSS differences act in an opposite manner at buoyancy. Hence increase or decrease in SST is accompanied with an increase or decrease in SSS. The only exception is the Indian Ocean, where East and West in run A become less and more buoyant, respectively.
265 In Fig. 4, we augment the diagnostic by inspecting the Atlantic meridional overturning circulation (AMOC) which provides the most general characteristic of water mass transformation and production. The mean AMOC in both runs is expressed with the basinwide mid depth cell showing a maximum of ~ 15 Sv at ca 40°N. The bottom cell, induced by the circulation of the
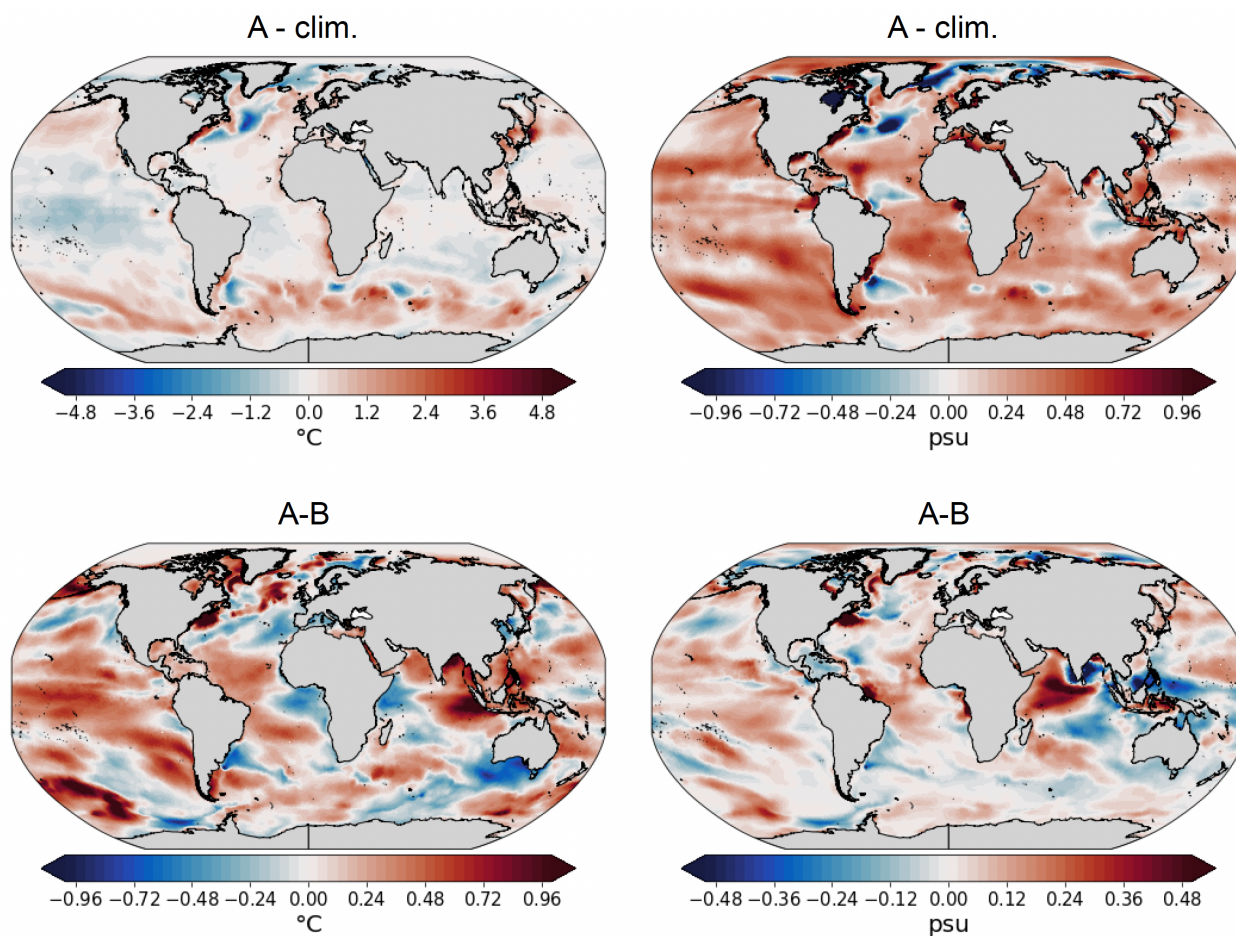
Figure 3. Maps showing differences in surface temperature [°C] (left column) and practical salinity (right column) between FESOM2.1 and the PHC climatology (top row) and between simulations A and B (bottom row) averaged over the time period 2012-2021.
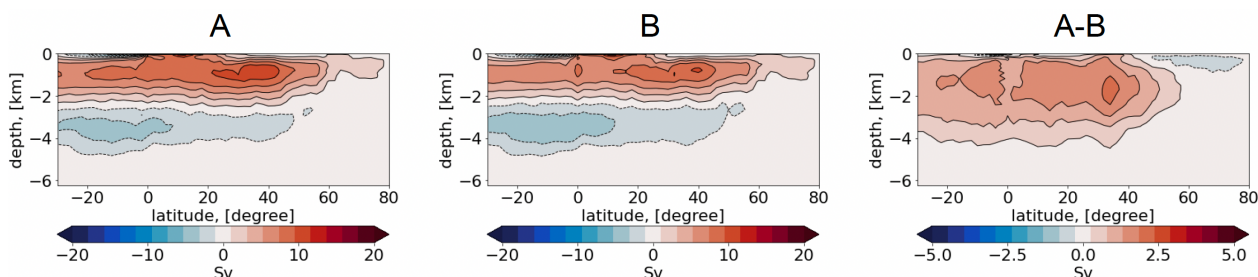
Figure 4. Vertical representation of the Atlantic Meridional Overturning Circulation (AMOC) in simulations A, B and their difference [Sv].
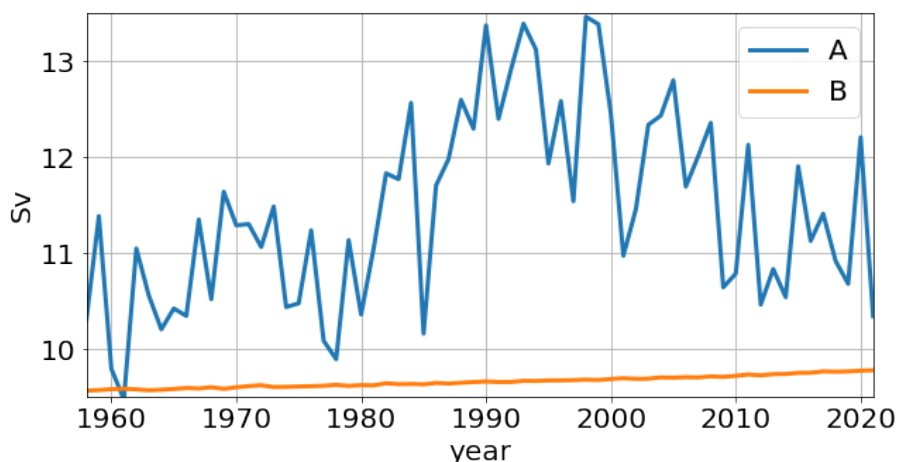
Figure 5. Time-series of annual mean Atlantic Meridional Overturning Circulation (AMOC) maxima in simulations A and B.
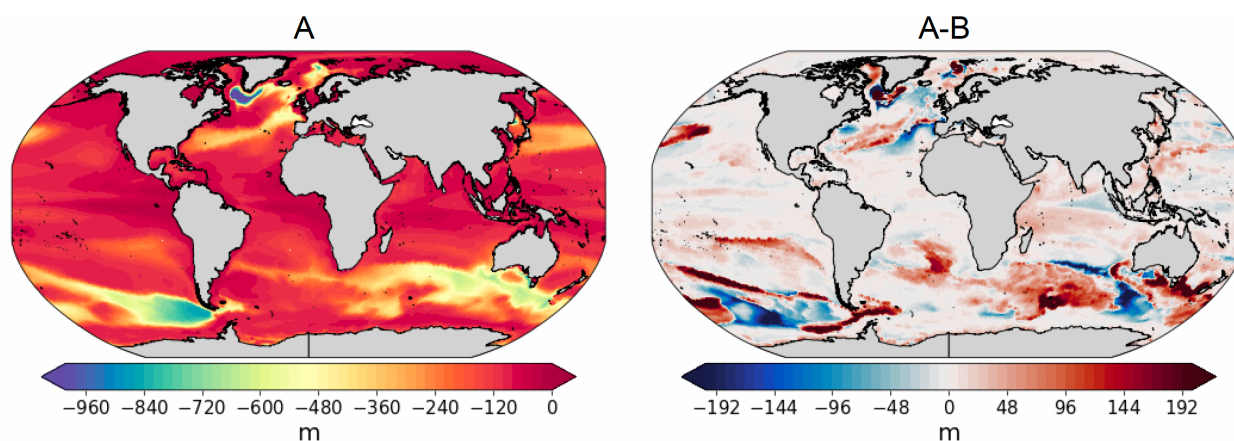
Figure 6. Mean of 2012-2021 annual maximum Mixed Layer Depth (MLD) in simulation A and difference between simulations A and B.

Antarctic Bottom water, is also well reproduced with a minimum of ~ -5 Sv. Even though the runs depict large differences in temperature and salinity from the observed climatology, the simulated AMOC shows the canonical picture as known from other works. This indicates that although biases in the representation of water mass properties and ventilation mechanisms are present, they still result in a reasonable density distribution which maintains realistic transports.

The difference between runs A and B shows that the mid depth and bottom cells are stronger in simulation B. Consequently, the difference A-B is expressed by a basinwide positive anomaly with a maximum of ~ 3 Sv. We also show the time-series of both AMOC maxima for the years 1958-2021 (Fig. 5). In run A, the time-series depicts a multidecadal variability with a minimum of ~9.5 Sv and a maximum of ~13.5 Sv. Concurrently the reference run B depicts a nearly constant value between 9.5 Sv and 10 Sv, a result of repeated year forcing.

Finally in Fig. 6 we present the annual maximum mixed layer depth (MLD) pattern. It matches those known from literature with the deepest MLD (>1000 m) found in the Labrador Sea (LS). The (annual maximum) MLD difference between the two simulations is within the depth range of ~200 m. In run B the MLD is deeper in the central LS but shallower in the surrounding

280 area of it. Interestingly, the MLD difference there pursues the differences we found for SST and SSS patterns shown in Fig.1. From inspecting the model runs and their differences we conclude that FESOM2.1 simulated a reasonable ocean state which can be used for further analysis.

3.2 Nutrients, ocean productivity and ecosystem
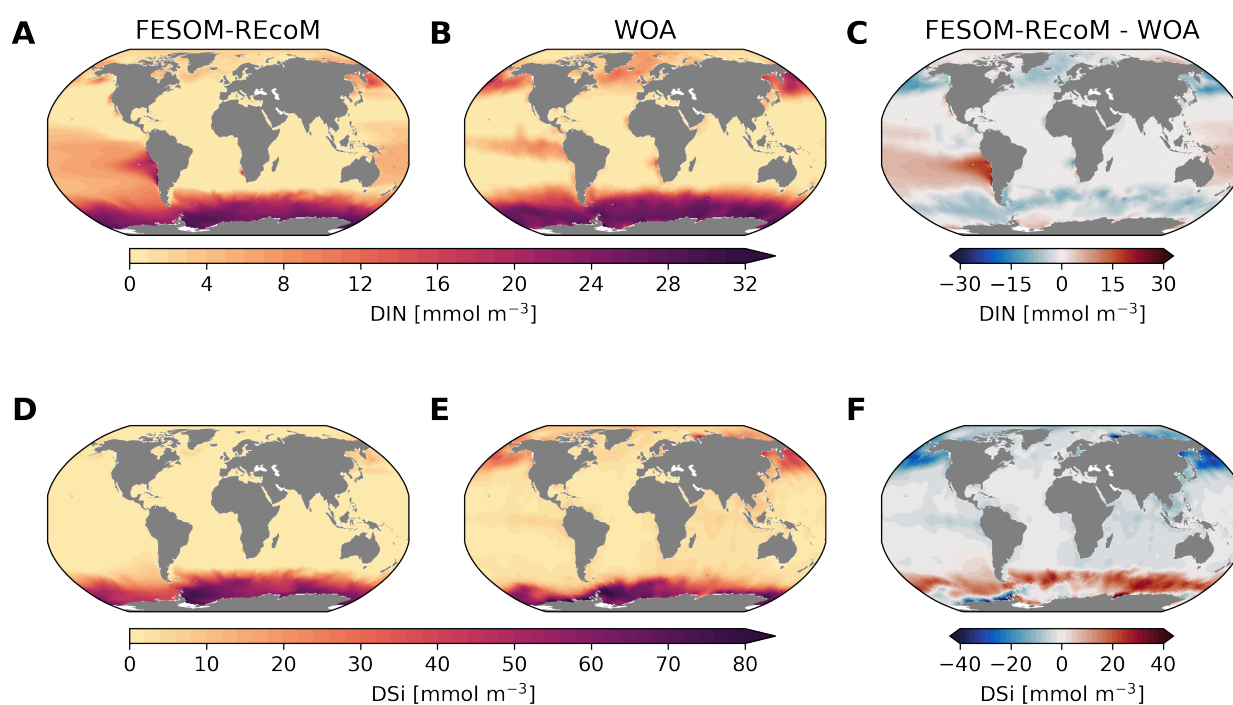
Figure 7. Maps of simulated FESOM2.1-REcoM3 surface [0-100m] concentration of dissolved inorganic nitrogen [mmol m^{-3}] (A), dissolved inorganic silicon [mmol m^{-3}] (D) with observations from the World Ocean Atlas 2018 climatology (B and E, Garcia et al., 2019b) and corresponding differences (C, F) averaged over the time period 2012-2021.

3.2.1 Modeled versus in situ nutrients

285 We first compared the spatial distribution of surface (averaged over the top 100m depth layer) ocean dissolved inorganic nitrogen (DIN) and dissolved silicate (DSi) from REcoM3 with the World Ocean Atlas 2018 (Garcia et al., 2019b) climatologies (Fig. 7). While simulated surface DIN concentrations were lower than observations in the subpolar regions, a large positive DIN bias of up to 20 mmol m^{-3} was found in the subtropical South Pacific Ocean. The simulated DSi was overestimated in

the Southern Ocean and underestimated in the northern Pacific. Exceptions are the Pacific and Atlantic sectors of the coastal

290   Southern Ocean where the modeled DSi concentrations are lower than the observations. These patterns were already present in FESOM1.4-REcoM2 (Schourup-Kristensen et al., 2014), however, two recent improvements should be noted. First, the large and positive DIN bias in the northern subtropical Pacific (Schourup-Kristensen et al., 2014) disappeared. This is caused by replacing the dust deposition input forcing field from Mahowald et al. (2003) with Albani et al. (2014), which results in more realistic (i.e., less strong) iron limitation. Second, the silicate bias in the Southern Ocean is reduced in magnitude and

295   extent compared to Schourup-Kristensen et al. (2014). This is related to tuning experiments (not shown), which resulted in a larger share of diatoms in the Southern Ocean (Figure 12) compared to Schourup-Kristensen et al. (2014), thus drawing down more silicic acid. Along with the increased share of diatoms, the Southern Ocean opal export has also increased from 74.5 Tmol Si yr^{-1} in Schourup-Kristensen et al. (2014) to 115 Tmol Si yr^{-1} in the present study and is thus more centrally positioned in the range of 69-185 Tmol Si yr^{-1} (Dunne et al., 2007) and close to the best estimate of Tréguer et al. (2021)

300   (Table 3). The silicic acid bias is rather insensitive to formulation and parameter choice of opal dissolution, but very sensitive to the share of diatoms in the Southern Ocean. The correlation coefficient and root mean squared error (RMSE) between simulated and observed annual mean DIN were 0.88 and 0.86 mmol m^{-3} respectively, and 0.47 and 0.54 mmol m^{-3} for DSi. The correlation with observed DIN is higher than in Schourup-Kristensen et al. (2014, 0.75), which we relate to the disappearance of the DIN bias in the northern subtropical Pacific. The correlation with observed DSi is lower than in FESOM-

305   1.4-REcoM2, despite the reduction in magnitude and extent in the Southern Ocean DSi bias. Moderately high silicic acid values in the northern high latitudes are not reproduced.
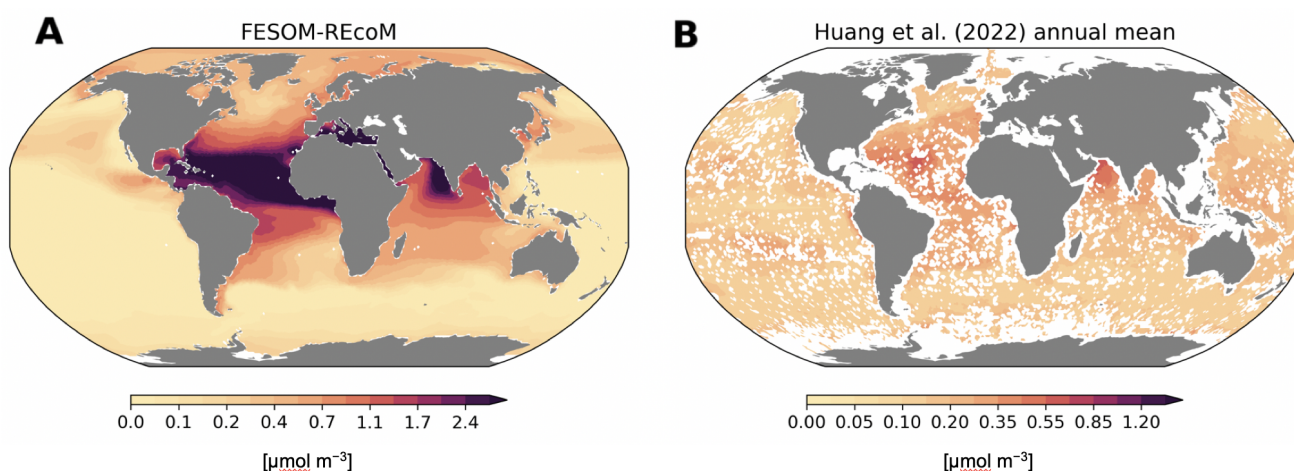
Figure 8. Maps of simulated FESOM2.1-REcoM3 surface [0-50m] concentration of dissolved iron [μmol m^{-3}] (A), and of the AI-based global reconstruction by Huang et al. (2022) (B). Note the different colorscale for the two plots.

Despite the enormous increase in the number of observations of dissolved iron with the GEOTRACES project, observations have not reached a global coverage that makes it possible to construct a global climatology. Therefore the modeled dissolved

iron is compared here to the global surface pattern of dissolved iron by Huang et al. (2022), which uses an artificial intelligence
310   method (random forest) to construct a near global iron field, based on the observations in the second intermediate GEOTRACES
data product (Schlitzer et al., 2018), plus some older in-situ iron observations compiled in Tagliabue et al. (2012), and on co-
located hydrographic observations. The pattern of modeled dissolved iron (Figure 8, averaged over the top 50 m) shows the
expected pattern of high concentrations in regions with high dust deposition, mainly in the tropical Atlantic Ocean and the
eastern part of the Arabian Sea, but also to some extent in the southern subtropical Atlantic and Indian Oceans. Concentrations
315   are extremely low in the subpolar Southern Ocean, and almost the whole Equatorial and South Pacific. Iron concentrations are
also low in the subpolar North Pacific, and — less so, but still noticeable — in the subpolar North Atlantic. Oceanic regions
adjacent to extended shelves, especially in the Arctic, show somewhat elevated iron concentrations. If we compare this to the
AI-generated global pattern of dissolved iron from Huang et al. (2022) we find qualitatively similar patters, like the elevated
iron concentration in the equatorial and subtropical Atlantic and the Arabian Sea, or the low concentrations in the subpolar
320   Southern Ocean, the equatorial Pacific, and the subpolar North Pacific, but the amplitude of the patterns is quite a bit smaller.
An important difference is that the distribution by Huang et al. (2022) shows slightly elevated iron concentrations in the center
of the subtropical South Pacific, where the model in contrast has extremely low values. This discrepancy causes a too strong
iron limitation in this region in the model, probably explaining the overly high DIN concentrations in the model South Pacific.
The too strong amplitude of the patterns in modeled dissolved iron, which is also found in other models, likely has a number of
325   causes. The most important one is probably the assumption of a constant solubility in dust-deposited iron. Dust deposition close
to the main source regions is on average coarser and has experienced less chemical processing during its transport, which both
would lead to a lower solubility, while the opposite is true for regions far from the source regions, such as in the South Pacific.
A second contribution might be the missing source from pyrogenic aerosols, which are far more soluble. Also, the effect of
dust particles as iron scavengers, which has not been included in this simulation, has been shown to reduce the overly high
330   dissolved iron concentrations often found in models under the main dust deposition regions (Ye and Völker, 2017; Pagnone
et al., 2019). Despite the overall too strong amplitude of the patterns in dissolved iron, especially in the regions of high dust
deposition, the model is able to reproduce the main regions where iron availability limits phytoplankton productivity (Moore
et al., 2013), namely the subpolar Southern Ocean, the equatorial and North Pacific, and to some extent also the seasonal iron
limitation in the subpolar North Atlantic (Nielsdóttir et al., 2009), but overestimates iron limitation in the subtropical South
335   Pacific.

3.2.2   Modeled versus satellite-based Chlorophyl a

The modeled spatial distribution of (log10 transformed) chlorophyll a concentration averaged from 2012 to 2021 was compared
with the Ocean Colour Climate Change Initiative (OC-CCI) merged data set (Sathyendranath et al., 2019). Over large parts
of the global ocean, the mean surface chlorophyll a concentrations are in agreement with observations (Fig. 9 panels C and
340   D). Yet, there are regional differences. The model underestimates chlorophyll concentration in most of the coastal regions,
such as in the coastal Arctic regions with biases reaching about 3 mg chlorophyll a m^{-3}. In temperate latitudes, the modeled
chlorophyll a concentrations are somewhat higher than observed while the subtropical gyres show concentrations slightly

lower than observations. The comparison of modeled and observational-based satellite estimates of chlorophyll a yielded a correlation of 0.66. Note, however, that remote sensing global semi-analytical algorithms, such as the one use in OC-CCI

345 (the Garver–Siegel–Maritorena model version 1; GSM01, Maritorena et al., 2002) are mostly adapted for global studies, but still require regional tuning in coastal regions, where the presence of non-biotic optically active material makes chlorophyll a retrieval challenging (Blondeau-Patissier et al., 2014).
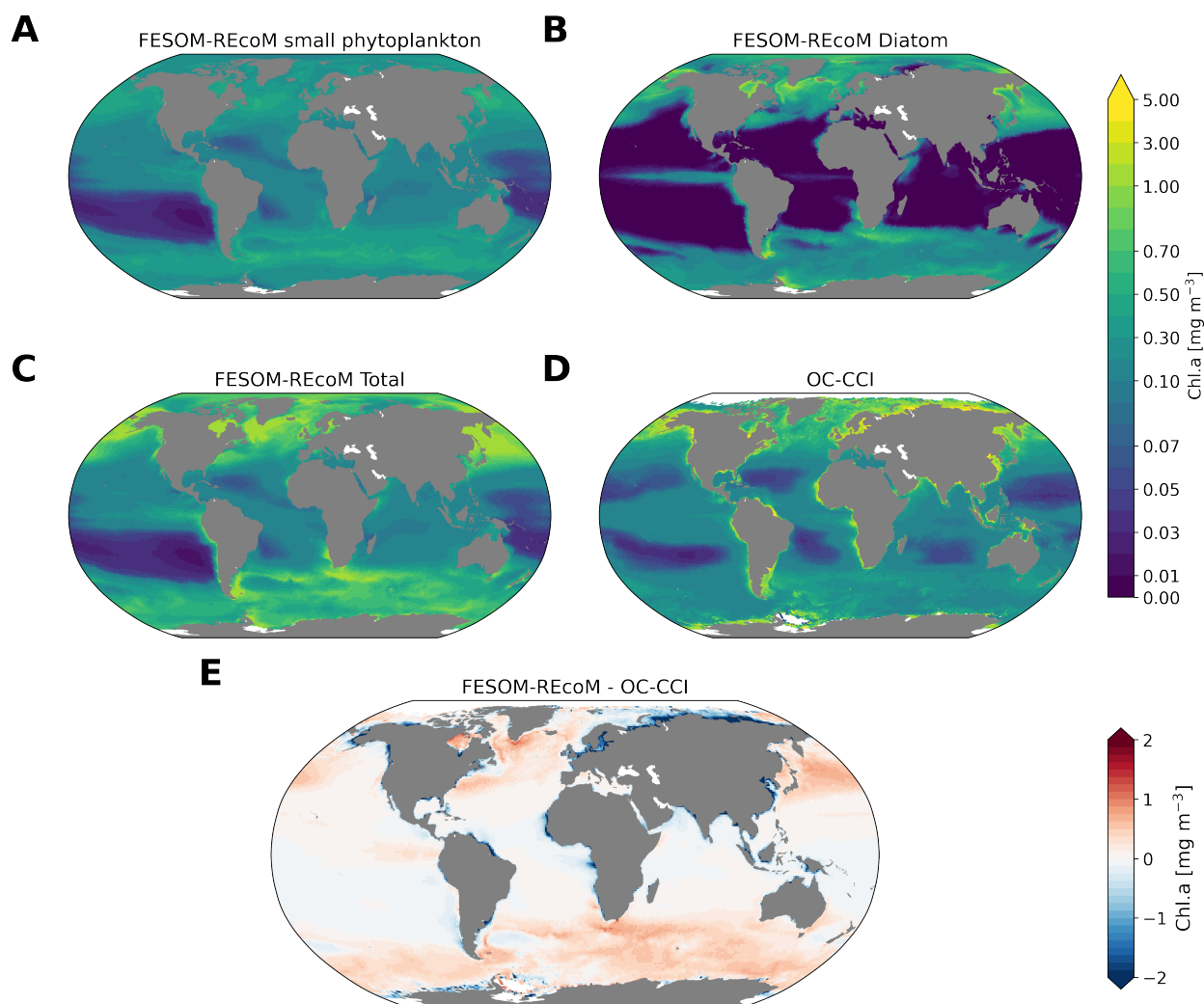
Figure 9. Maps of simulated FESOM2.1-REcoM3 (simA) surface chlorophyll a concentration [mg Chl m^{-3}] of small phytoplankton (A), diatoms (B) and the sum of both phytoplankton groups (C). The satellite-based merged dataset OC-CCI is shown in (D, Sathyendranath et al., 2019) with corresponding differences between FESOM2.1-REcoM3 and OC-CCI (E). Note the different time periods of the simulation (2012-2021) and OC-CCI (1998-2019).

3.2.3 Modeled versus satellite-based NPP
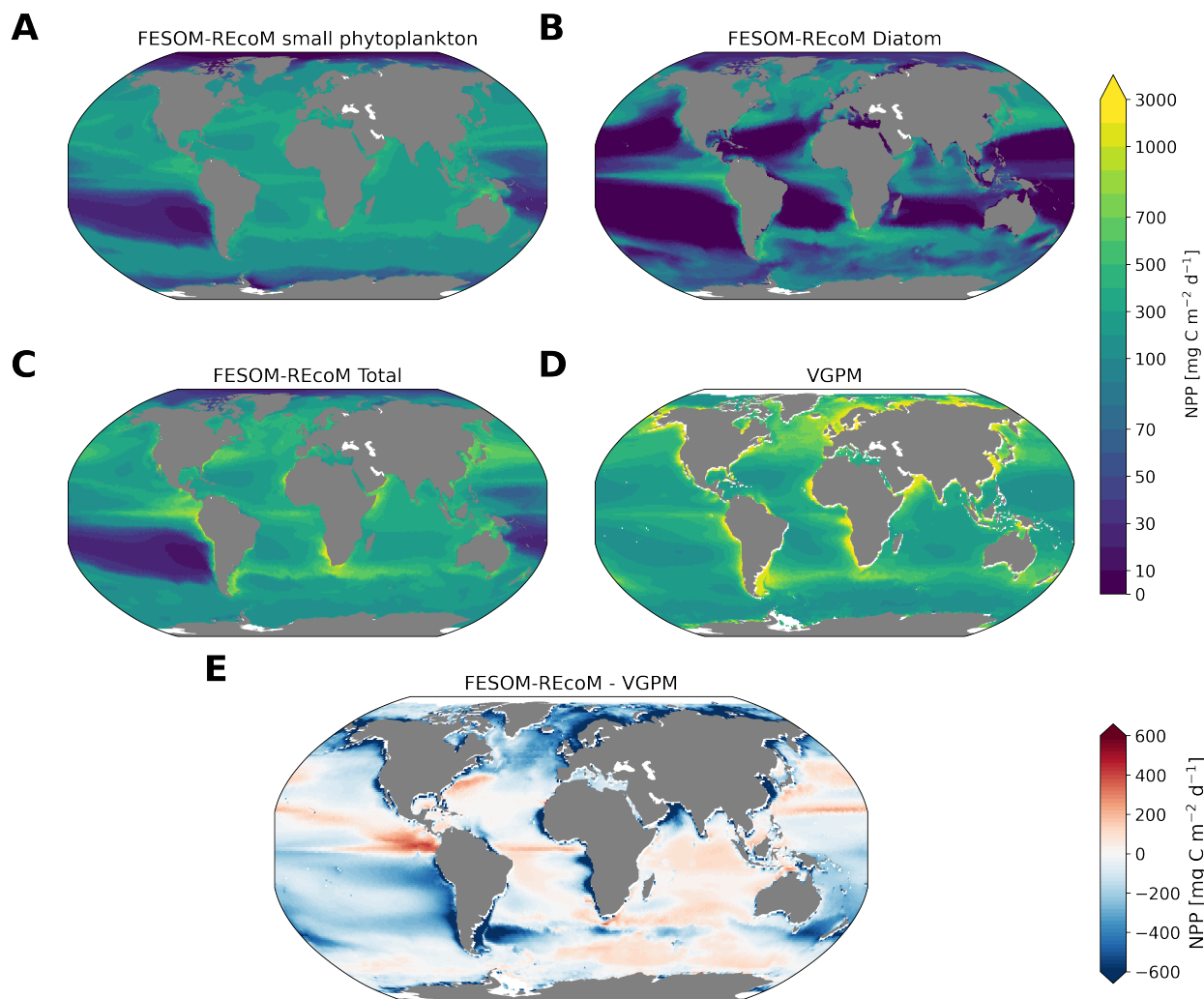
Figure 10. Maps of simulated FESOM2.1-REcoM3 (simA) vertically integrated net primary production [mgC m^{-2} d^{-1}] of small phytoplankton (A), diatoms (B), and the sum of both phytoplankton groups (C). The satellite-based Vertically Generalized Production Model (VGPM) is shown in (D; Behrenfeld and Falkowski, 1997) with corresponding differences between FESOM2.1-REcoM3 and VGPM (E). All fields are averaged over the time period 2012 to 2021.

We also compared the modeled vertically integrated Net Primary Production (NPP, Fig. 10) with the Vertically Generalized
350 Production Model (VGPM, Behrenfeld and Falkowski, 1997). VGPM is a chlorophyll-based algorithm that can be considered
as a standard NPP estimation from ocean color for the last 20 years (Lee and Marra, 2022). VGPM therefore carries uncertainties related to the global Chlorophyll algorithm (OC4) adapted to CASE-I waters (low influence of dissolved organic matter

and non-algal particles) that is not adapted to coastal regions (CASE-II waters, high influence of dissolved organic matter and non-algal particles). For example, turbid waters contaminated by yellow substances or sediments over the Arctic shelves is a

355 known issue that artificially increases both Chlorophyll a and NPP (Matsuoka et al., 2012; Mitchell, 1992; Mustapha et al., 2012). Some recent advances used local parametrizations with in situ data which resulted in much lower productivity levels in those coastal areas (Lewis et al., 2020; Lewis and Arrigo, 2020). Therefore, we additionally compared modelled NPP with the updated Carbon-based Productivity Model (CbPM, Westberry et al., 2008, see Appendix Fig. A1). CbPM uses spectrally resolved light attenuation and is based on a semi-analytical algorithm (Garver-Siegel-Maritorena, GSM, Maritorena et al.,

360 2002) which tries to distinguish optical signatures from phytoplankton, particles and dissolved organic matter. Nevertheless, both algorithms are subject to large uncertainties (Lee and Marra, 2022). When compared with VGPM, the model simulation generally underestimated the remotely sensed NPP estimations (Table 3), especially in the subtropical Pacific. Yet, with a value of 35.9 PgC yr^{-1} the modeled global total NPP is slightly above the range of earlier modeling studies (23.7 - 30.7 PgC yr^{-1}, Schneider et al., 2008), and within the range of recent Earth System Models (24.5 - 57.3 PgC yr^{-1}, Séférian et al., 2020). It is

365 lower than other satellite-based estimates of 47.3 PgC yr^{-1} (Behrenfeld and Falkowski, 1997), 52 PgC yr^{-1} (Westberry et al., 2008) and 48.7 - 52.5 PgC yr^{-1} reported by Kulk et al. (2020).

The low values of primary production could be caused by several top-down and/or bottom-up effects. The nutrient dynamics that partly control NPP, are the result of a delicate balance between physical (mixing, stratification and upwelling systems) and biogeochemical processes. To investigate bottom-up controls on regional NPP dynamics, we derived the most limiting factor

370 (either light or nutrients) of growth of diatom and small phytoplankton. This factor ranges between 0 (most limiting) and 1 (no limitation) and is based on the nutrient uptake Michaelis–Menten kinetics of REcoM. The Michaelis–Menten coefficient (MM) is computed as MM = [Nut]/([Nut] + KNut), with [Nut] being the nutrient concentration, and KNut a nutrient and phytoplankton dependent half-saturation constant. The light limitation is defined as the carbon-specific photosynthesis rate divided by the maximum photosynthetic rate. We derived maps showing the most limiting factor (factor closest to zero, either

375 nutrients DIN, DSi, or DFe, or light) in the annal mean (Fig. 11).

Spatial distribution of the dominant growth-limiting factor for diatoms and small phytoplankton over the time period 2012-2021 is shown in Fig. 11. Over large areas of the Southern Pacific and almost the entire Southern Ocean diatoms were limited by iron availability. Elsewhere, except for the Arctic Ocean where light was the most limiting factor, diatom growth was controlled by the abundance of dissolved silicic acid. Nutrient uptake of small phytoplankton was limited by iron in the South

380 Pacific, DIN within the band of 45°S-45°N in the Atlantic and Indian Oceans and insufficient light at high latitudes (south of 45°S and north of 45°N).

The large-scale patterns of limitation were in general agreement with observations (Moore et al., 2013) and other modelling studies (Long et al., 2021a), although the degree of silicic acid limitation for diatoms (outside the iron-limited Southern Ocean) varied across models (Laufkötter et al., 2015). The more severe than expected limitation in iron in most of the Pacific might

385 contribute to the lower productivity levels than observed in the same regions (Fig. 10).

In addition to bottom-up explanations, one can also raise a too high grazing pressure from zooplankton due to the choice of grazing formulations and parameter values as a reason for low primary production (Anderson et al., 2010; Prowe et al.,
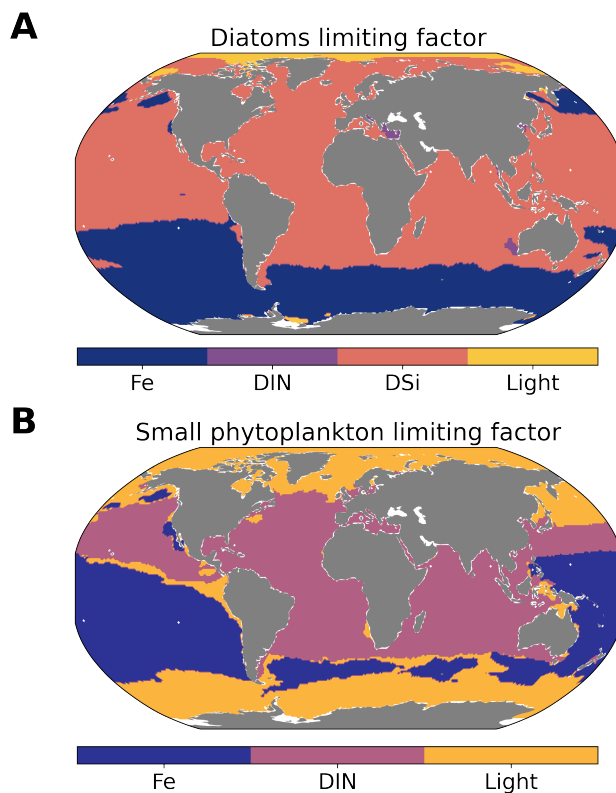
Figure 11. Maps showing the spatial distribution of the most limiting factor in the model's surface water for Diatoms (A) and small phytoplankton (B). Fe: iron, DIN: dissolved inorganic nitrogen, DSi: dissolved silicic acid.

2012; Karakuş et al., 2021). In fact, Karakuş et al. (2022) demonstrated that a separation of the small zooplankton group in REcoM into micro- and mesozooplankton leads not only to a 25% increase in NPP but also to a reduction of overly strong iron limitation in the South Pacific, due to nutrient recycling by zooplankton. Further, REcoM does not explicitly represent picophytoplankton (e.g., non N_2-fixing cyanobacteria such as Synechococcus and Prochlorococcus) and nitrogen fixers, and this might contribute to an underestimation of NPP.

Too low primary production and chlorophyll a levels were particularly evident in coastal regions, which could be linked to deficiencies in either the chlorophyll data set (see above) or in the model. For the latter, reasons could be coarse model resolution and associated weak upwelling and missing phytoplankton classes in the model, but also insufficient nutrient input from terrigenous sources. The results for net primary productivity and chlorophyll obtained here are comparable to those presented by Schourup-Kristensen et al. (2014).

The latitudinal distribution of chlorophyll a and NPP were compared with estimations from remote sensing products (Fig. 12). In low latitudes, FESOM2.1-REcoM3 shows a reasonably simulated latitudinal variation of chlorophyll a and NPP compared to VGPM. In the southern high latitudes, FESOM2.1-REcoM3 follows the Southern Ocean adjusted chlorophyll data set
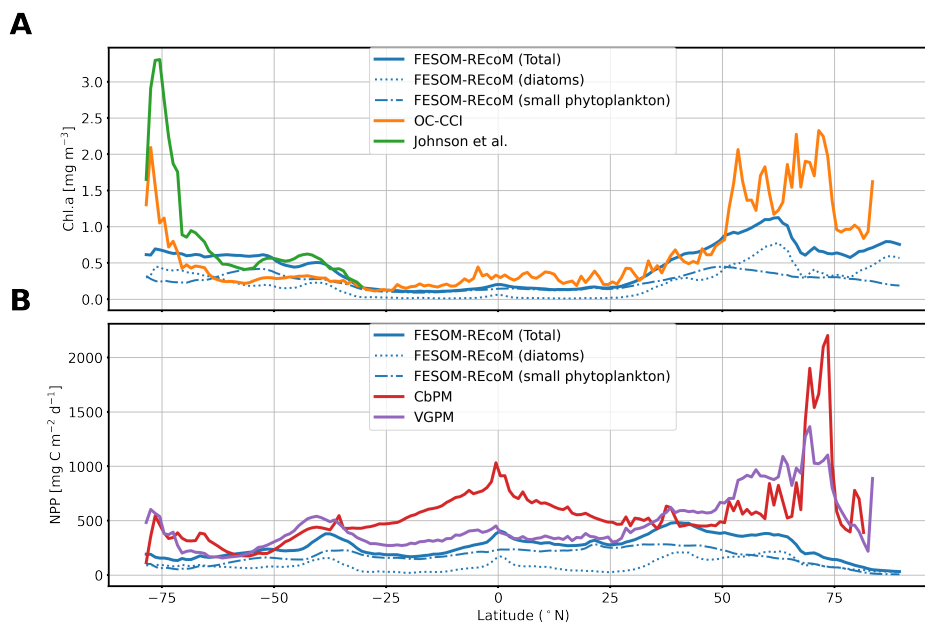
Figure 12. Latitudinal distribution of vertically integrated and zonally averaged (A) chlorophyll a [mg Chl m^{-3}] and (B) net primary production [mg C m^{-2} d^{-1}] simulated by FESOM2.1-REcoM3 (blue line). The satellite-based merged chlorophyll a datasets of OC-CCI (Sathyendranath et al., 2019, orange line) and the improved chlorophyll a algorithm of the Southern Ocean (Johnson et al., 2013, green line) are shown in (A). The satellite-based dataset of the Vertically Generalized Production Model (VGPM) (Behrenfeld and Falkowski, 1997, purple line) and the Carbon-based Productivity Model (CbPM) (Westberry et al., 2008, red line) are shown in (B).

well, except for the coastal regions close to Antarctica (approximately south of 70°S). Similarly, NPP corresponds reasonably well to the VGPM estimate in the open Southern Ocean, but may underestimate NPP in Antarctic coastal waters. In the northern high latitudes, however, the simulated chlorophyll a values are lower than the satellite estimations. Inspecting the spatial distribution (Fig. 9) reveals that this is also largely a coastal underestimation. In the open ocean in northern high-latitudes, 405 chlorophyll is reasonably well reproduced and even partly higher than the satellite-based estimate. In terms of NPP, differences between simulated and satellite estimations are larger in productive areas north of 50°N, which are strongest at the coast, but also apparent in the open ocean of the North Atlantic. For regional applications, further analysis and possibly tuning may be needed.

3.2.4 Modeled versus MAREDAT zooplankton biomass

410 In REcoM3, the small zooplankton group is widely spread in the global ocean and the highest biomass occurs in high-productivity regions (Fig. 13A). The macrozooplankton is present in the high latitudes (Fig. 13B) since it is parametrized as a polar macrozooplankton group (Karakuş et al., 2021). We compared the latitudinal distribution of integrated modeled zooplankton biomass with gridded global zooplankton biomass data from MAREDAT (Buitenhuis et al., 2010; Moriarty et al.,

2013; Moriarty and O'Brien, 2013). The simulated biomass of small and total zooplankton reproduces MAREDAT-derived

415 biomass reasonably well in low to mid latitudes, but underestimates biomass in the polar regions (Fig. 13C). The underestimation of zooplankton biomass in the northern high latitudes may be related to an underestimation of primary production in the same region. In agreement with the MAREDAT data set (Moriarty et al., 2013), macrozooplankton is not present in low latitudes.

3.2.5 Synthesis

420 The modeled biogeochemical fluxes were compared to the previous version FESOM1.4-REcoM2 and observational studies (Table 3). Modelled global NPP is higher in FESOM2.1-REcoM3 than in FESOM1.4-REcoM2, but still lower than in satellite-based estimates. The estimate is comparable to other modelling studies (Schneider et al., 2008; Séférian et al., 2020). Export production (EP) is slightly lower in FESOM2.1-REcoM3 than in the previous version, and falls within the observational range previously documented in the literature for both the global and the Southern Ocean. For the global ocean, FESOM2.1-REcoM3

425 NPP and EP estimations remained at the lower end of the range despite a slight increase in NPP. A more detailed description of zooplankton can increase NPP by 25% (Karakuş et al., 2022). In the Southern Ocean, estimations of NPP and EP remained very close to observations. Maybe the most noticeable change between the two model versions is the substantial increase in opal export which almost doubled in the Southern Ocean, passing from the lower to the middle of observational range in an earlier review (Dunne et al., 2007), and is in excellent agreement with an updated estimate (Tréguer et al., 2021). This is due

430 to an increase in diatoms relative contribution to the total NPP in high latitudes (Fig. 12).

3.3 Carbon cycle

3.3.1 Dissolved inorganic carbon and alkalinity

Insight into the carbonate system can be obtained by inspecting surface maps of modeled dissolved inorganic carbon (DIC) and alkalinity and the corresponding observational GLODAPv2 climatologies (Fig. 14). Global patterns of simulated concentrations

435 resemble the observed fields reasonably well (R = 0.81, RMSE = 59.3 mmol m^{-3}, calculated from annual means) with highest DIC values in the subtropical gyres of the Atlantic and south Pacific, as well as the subpolar North Atlantic and the Southern Ocean. Similar to GLODAP, highest alkalinity values are found in the subtropical gyres of the Atlantic and south Pacific. Yet, simulated surface DIC and alkalinity concentrations were slightly overestimated throughout the surface ocean. Two exceptions are the Arctic Ocean and the North Atlantic where the concentrations were underestimated. The departure from observations

440 differ in their patterns relative to FESOM-1.4-REcoM (too low DIC and ALK in the tropics and subtropics, too high in high latitudes, not shown), which indicates that different realisations in circulation or mixing may drive these bias patterns. This is in line with an overestimation of surface salinity in most of the global ocean with the exception of the North Atlantic and the Arctic Ocean (see Fig. 3). Also, surface alkalinity biases are generally attributed to a dominant physical (preformed) signal with a smaller contribution from the calcium carbonate cycle and a negligible contribution from organic matter remineralization

445 (Koeve et al., 2014). However, tuning the model to result in a higher CaCO$_3$ production could possibly also counteract the
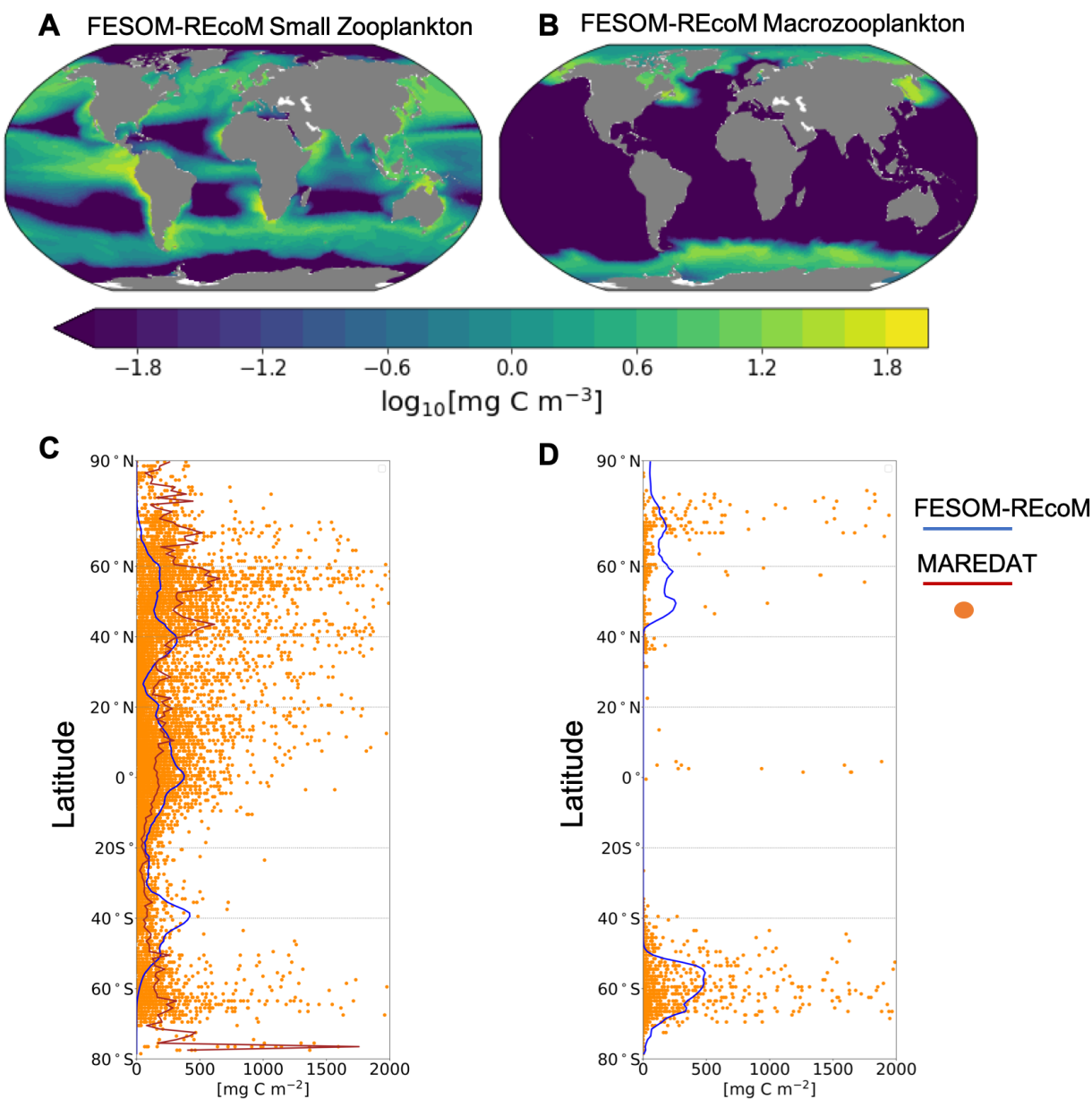
Figure 13. Maps of annual mean surface (A) small zooplankton and (A) macrozooplankton concentrations in FESOM2.1-REcoM3. Latitudinal distribution of vertically integrated [mg C m^{-2}] of (C) modeled small zooplankton (solid blue line) and sum of microzooplankton and mesozooplankton from MAREDAT (orange dots and solid brown line, Buitenhuis et al., 2010; Moriarty and O'Brien, 2013) and (D) modeled macrozooplankton (solid blue line) and macrozooplankton from MAREDAT (orange dots, Moriarty et al., 2013). Modeled zooplankton biomass is averaged over the time period 2012 to 2021.

Table 3. Global and Southern Ocean net primary production (NPP) and export production (EP) in FESOM2.1-REcoM3 and estimates from the literature. The Southern Ocean is considered as the region south of 50°S. The numbers for VGPM and CbPM are recalculated after interpolation to the model mesh over the years 2012-2019

	Unit	FESOM1.4-REcoM2 (Sim. A)	FESOM2.1-REcoM3 (Sim. A)	Range from literature
NPP global	PgC yr^{-1}	32.5	35.8	50.5 (VGPM, this study)
				68.9 (CbPM, this study)
				47.3 (Behrenfeld and Falkowski, 1997)
				52 (Westberry et al., 2008)
				23.7 – 30.7 (Schneider et al., 2008)
				48.7 - 52.5 (Kulk et al., 2020)
				24.5 - 57.3 (CMIP6) (Séférian et al., 2020)
EP global	PgC yr^{-1}	6.1	5.9	9.6 (Schlitzer, 2004)
				5.8-13 (Dunne et al., 2007)
				5 (Henson et al., 2011)
				5.9 (Siegel et al., 2014)
Opal export global	Tmol Si yr^{-1}	74.5	115	69-185 (review in Dunne et al., 2007)
				112 (Tréguer et al., 2021)
CaCO$_3$ export global	PgC yr^{-1}	1.2	0.59	0.1 - 4.7 (Seifert et al., 2022)
NPP Southern Ocean	PgC yr^{-1}	3.1	3.2	3.48 (VGPM, this study)
				3.92 (CbPM, this study)
				1.1-4.9 (Carr et al., 2006)
				5.7 (Behrenfeld and Falkowski, 1997)
EP Southern Ocean	PgC yr^{-1}	1.1	1.1	1.0 (Schlitzer, 2002; Nevison et al., 2012)
Opal export Southern Ocean	Tmol Si yr^{-1}	21.5	38	21-54 (Dunne et al., 2007)
CaCO$_3$ export Southern Ocean	PgC yr^{-1}		0.044	0.018 (Dunne et al., 2007)
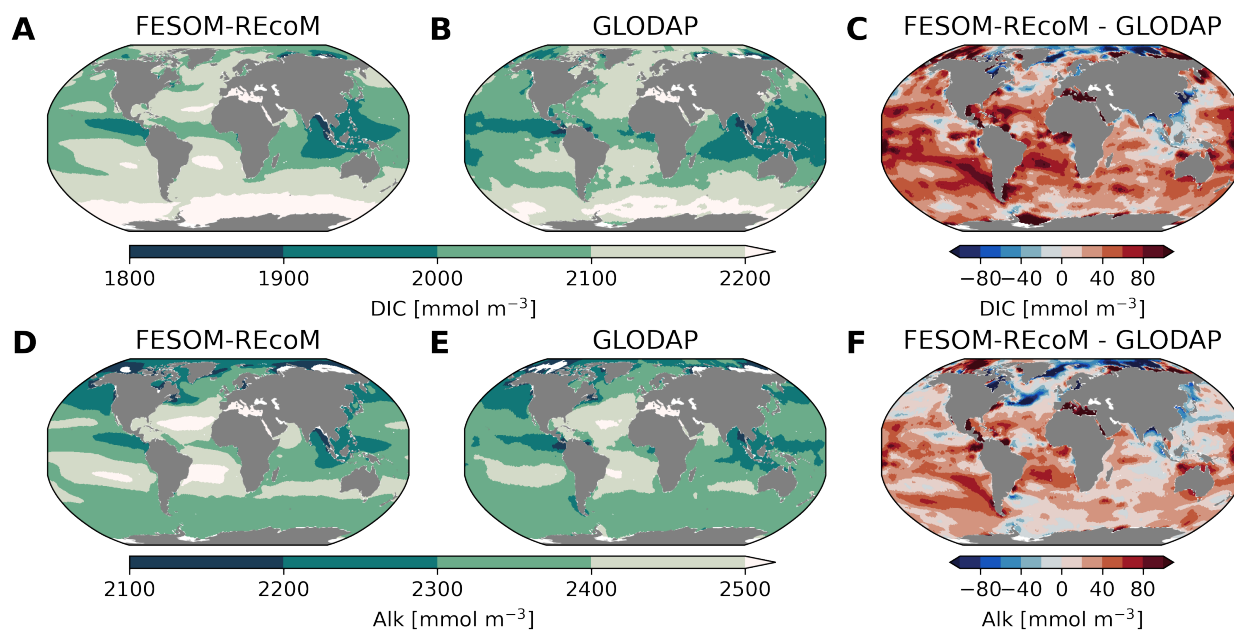
Figure 14. Maps of simulated FESOM2.1-REcoM3 surface [0-100m] concentration of dissolved inorganic carbon [mmol m^{-3}] (A) and alkalinity [mmol m^{-3}] (D); corresponding data from GLODAPv2 (B, E; Lauvset et al., 2016) and model-data differences (C, F). The comparison is for the period of 2012-2021.

positive alkalinity bias. Similarly, a higher NPP in the South Pacific could regionally ameliorate the high DIC bias. A positive bias in alkalinity at constant atmospheric CO_2 in the spin-up (not shown) and simulation A (Fig. 14) leads to a positive bias in DIC as surface water with a higher alkalinity can hold more CO_2 in equilibrium than a low-alkalinity surface ocean. The range of biases is similar as in other ocean biogeochemical models (e.g., Tjiputra et al., 2020; Long et al., 2021a).

450 ### 3.3.2 Surface ocean pCO$_2$ and air-sea CO$_2$ flux

We compare the pattern of the temporal mean (2012-2021) surface ocean partial pressure of CO_2 (pCO$_2$, Figure 15) and air-sea CO_2 flux (Figure 16) to the pCO$_2$-based data-product of Chau et al. (2022) with a seamless coverage from open ocean to the coasts (Fig. 16). The spatial patterns of pCO$_2$-products largely agree with each other although the magnitude differs (Fay et al., 2021; Fay and McKinley, 2021). Therefore we chose one of them (Chau et al., 2022) and focus on the comparison of

455 the spatial pattern with our model. We further evaluate the temporal evolution of pCO$_2$ in FESOM2.1-REcoM3 with a direct comparison to surface ocean pCO$_2$ observations from the Surface Ocean CO_2 Atlas (SOCAT, Bakker et al., 2016), where we subsampled the model output for spatio-temporal locations where observations exist, following Hauck et al. (2020) and Friedlingstein et al. (2022b) in Figure 17.

The large-scale spatial patterns of pCO$_2$ are well reproduced (Figure 15) with high values in the tropics that are typically

460 higher than atmospheric values (red colors), and lower values in the subpolar Southern and Pacific Ocean and the high-latitude
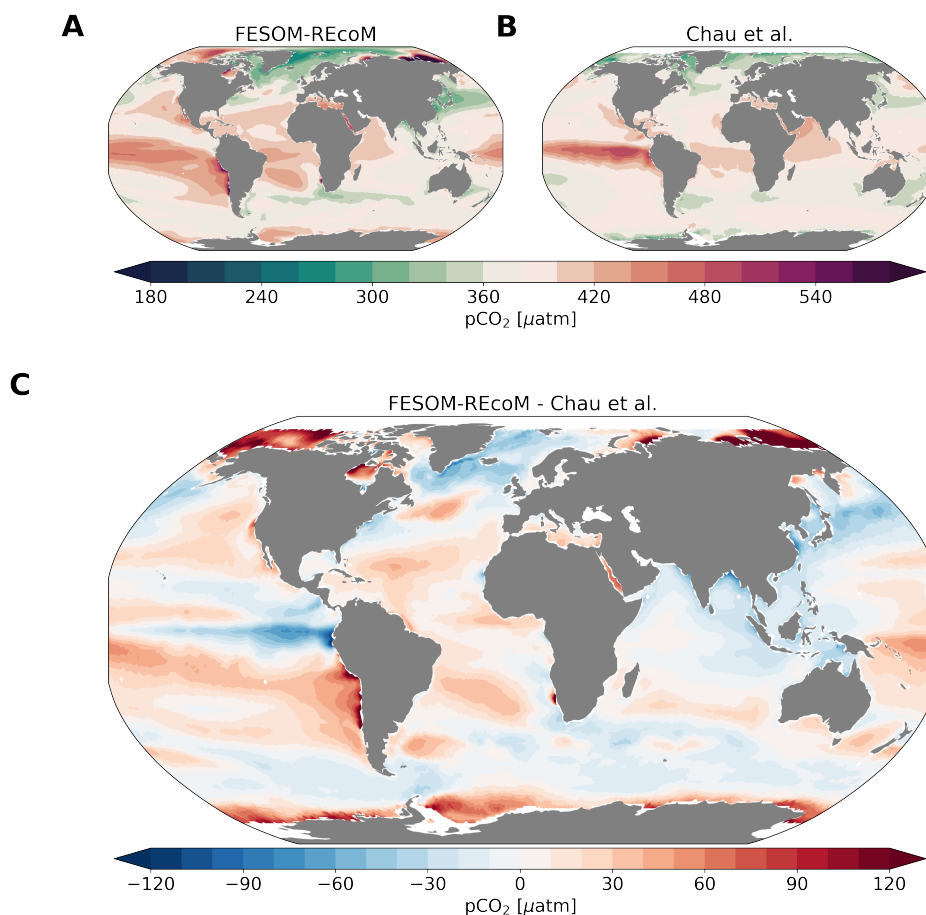
Figure 15. Maps of surface ocean pCO_2 [μatm]. The top row compares the (A) simulated FESOM2.1-REcoM3 surface partial pressure of CO_2 to the (B) pCO_2-based data-product (Chau et al., 2022), both averaged over 2012-2021. The bottom pannel (C) shows model-data differences.

North Atlantic. However, compared to the pCO_2-product of Chau et al. (2022), model pCO_2 values are overestimated in the subtropical gyres (Figure 15C). Further, the North Atlantic pCO_2 is on average lower than the pCO_2-product, and the two data sets also differ on over- versus undersaturation of pCO_2 relative to the atmosphere in the polar Southern Ocean (higher values in FESOM2.1-REcoM3). The latter may well be explained by a known summer bias in Southern Ocean pCO_2

465 observations (e.g., Metzl et al., 2006; Gregor et al., 2019). FESOM2.1-REcoM3 also simulates very high pCO_2 values on the Russian shelves in the Arctic, where hardly any observations exist. Similarly high pCO_2 values were reported for this region by Anderson et al. (2009), but missing repeat observations prevent a conclusion on whether this is a robust signal and what its extent in time and space is.

FESOM-2.1-REcoM3 reproduced the temporal evolution of surface ocean pCO_2 reasonably well compared to SOCAT

470 when accounting for where and when pCO_2 sampling took place (Figure 17). The annual correlation coefficient and root
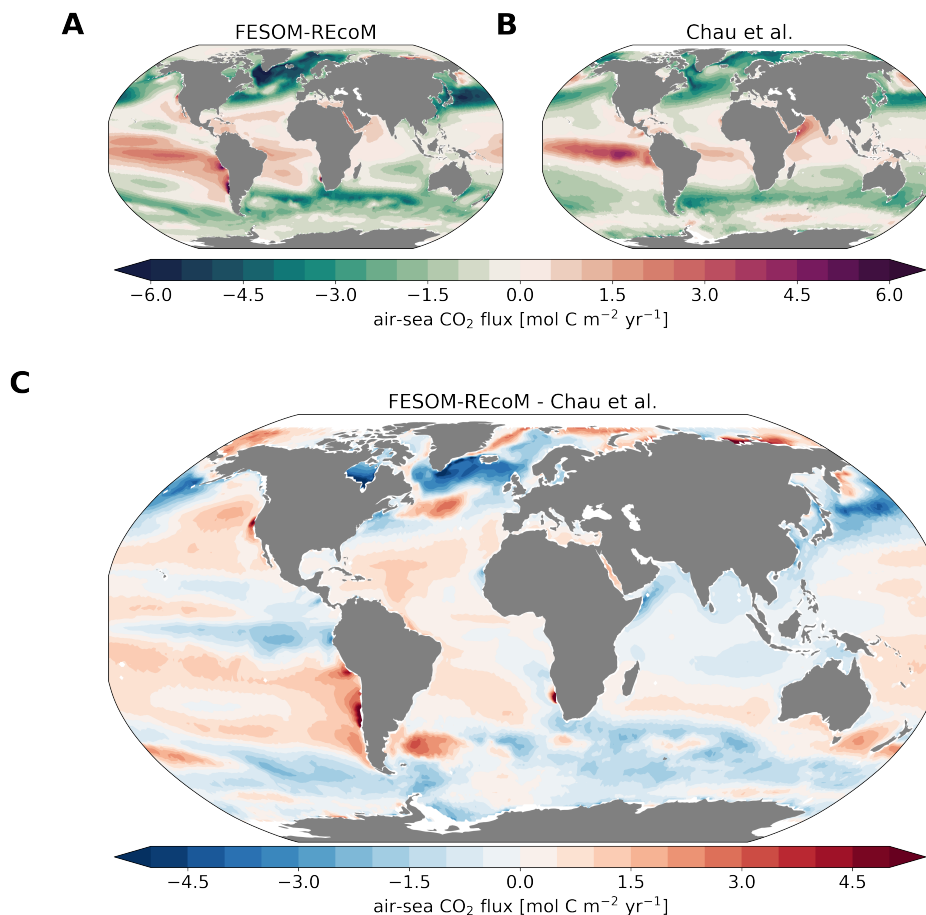
Figure 16. Maps of air-sea CO_2 fluxes. The top row compares the (A) simulated FESOM2.1-REcoM3 CO_2 flux to the (B) pCO_2-based data-product (Chau et al., 2022), both averaged over 2012-2021. The bottom pannel (C) shows model-data differences.

mean squared error (RMSE) between simulated and observed global mean pCO_2 are 0.93 and 4.6 μatm, respectively. The subsampled model follows the SOCAT time-series closely, including its variability, which may to some extent be caused by sampling distribution. The global mismatch with SOCAT pCO_2 as measured by the RMSE is comparable or slightly below the value for FESOM-1.4-REcoM2 (see supplementary Figure S9, 1985-2018, in Hauck et al., 2020) and comparable, but at the

475   high end of the range of other models in GCB2022 (1990-2021, Friedlingstein et al., 2022b). On a monthly scale, the RMSE is higher (38 μatm), as the models capture the large-scale patterns better than smaller-scale variability according to a previous assessment (Hauck et al., 2020). An analysis of large-scale regional patterns (North, Tropics, South, Figure 17) reveals that the model overestimates pCO_2 in the tropics and underestimates pCO_2 in the northern extra-tropics and to a lesser extent in the southern extra-tropics in recent decades, as also indicated in the maps (Figure 15).
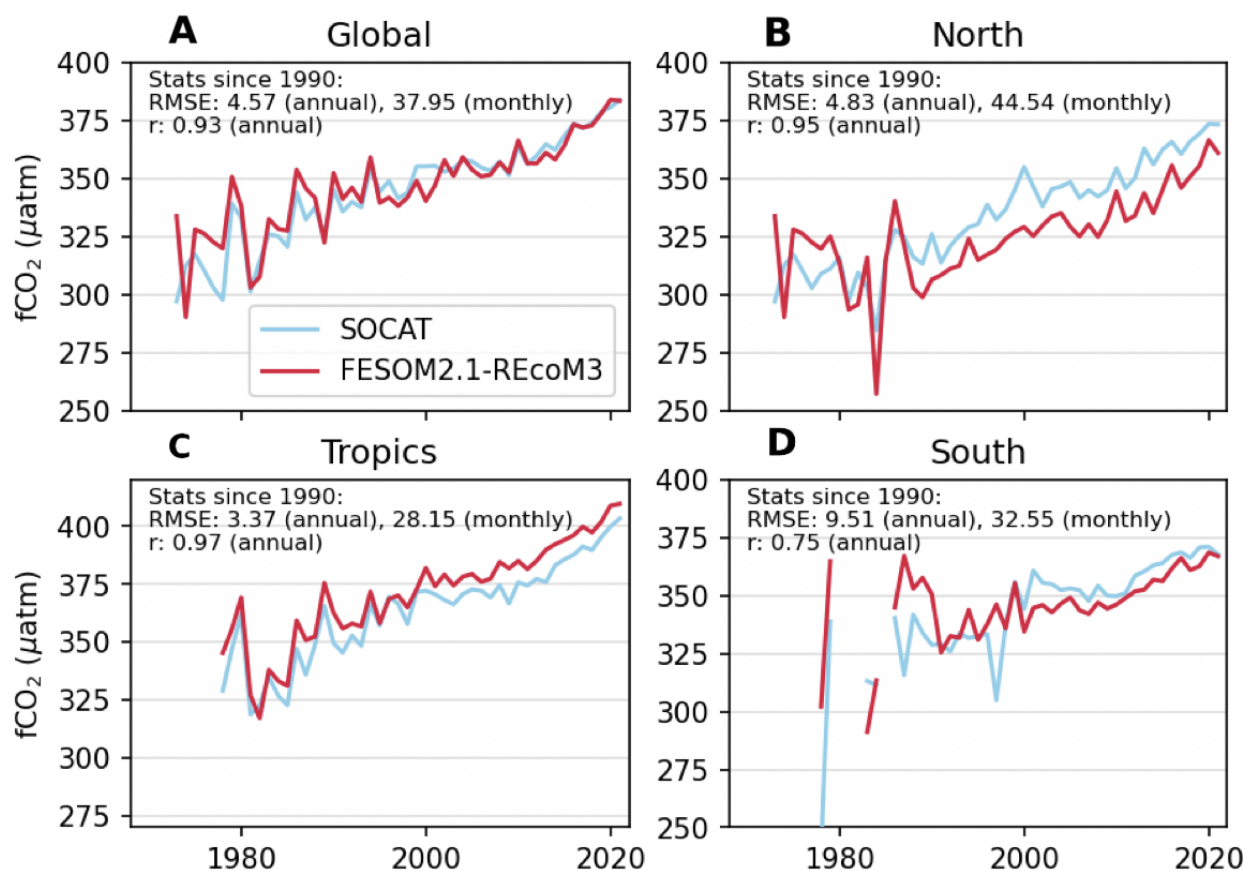
Figure 17. Comparing annual mean pCO_2 [μatm] from FESOM2.1-REcoM (subsampled for spatiotemporal locations of observations in SOCAT, red) with observations from SOCATv2022 (light blue, updated from Bakker et al., 2016). Results are shown spatially averaged for (A) the global ocean, (B) the northern hemisphere ($>30°$N), (C) the Tropics ($30°$S-$30°$N), and (D) the southern hemisphere ($<30°$S). The time-series are shown for all observations in SOCAT (since 1970), but correlation coefficient r (unitless) and Root Mean Squared Error RMSE (μatm) are indicated in the panels for the time period 1990–2021.

480   The air-sea CO_2 flux spatial pattern was reasonably reproduced by FESOM2.1-REcoM3 with CO_2 uptake in the subpolar regions of both hemispheres, and outgassing in the tropics and north Pacific (Figure 16). Generally, the CO_2 flux patterns mirror the pCO_2 patterns (Figure 15), but with the additional imprint of spatial variability of wind speed. Hence, the CO_2 uptake in the subpolar Southern Ocean may appear large compared to pCO_2, which is not as strongly undersaturated in the South as in the North Atlantic. Regions of mean outgassing in the Southern Ocean are of smaller extent in the model than in the

485   pCO_2-product. While it is well established that outgassing of CO_2 in the polar Southern Ocean occurs in winter (e.g., Bakker et al., 1997), its magnitude and timing varies between estimates and is under debate (Gruber et al., 2009; Lenton et al., 2013; Gray et al., 2018; Bushinsky et al., 2019; Sutton et al., 2021; Long et al., 2021b). The misfit between the annual mean modelled CO_2 flux and the pCO_2-based data-product generally mimic pCO_2 misfits and thus shows small positive misfits (less uptake or more outgassing) in the subtropical gyres and small negative biases (stronger uptake or less outgassing) in the equatorial

490   Pacific, and the Southern Ocean (Fig. 16, bottom panel). The strongest misfits were found in the northern high latitudes and the upwelling zone of the eastern tropical Pacific. The large mismatch in pCO_2 on the Siberian shelves does not show up in CO_2 flux as sea ice prevents CO_2 outgassing throughout most of the year.
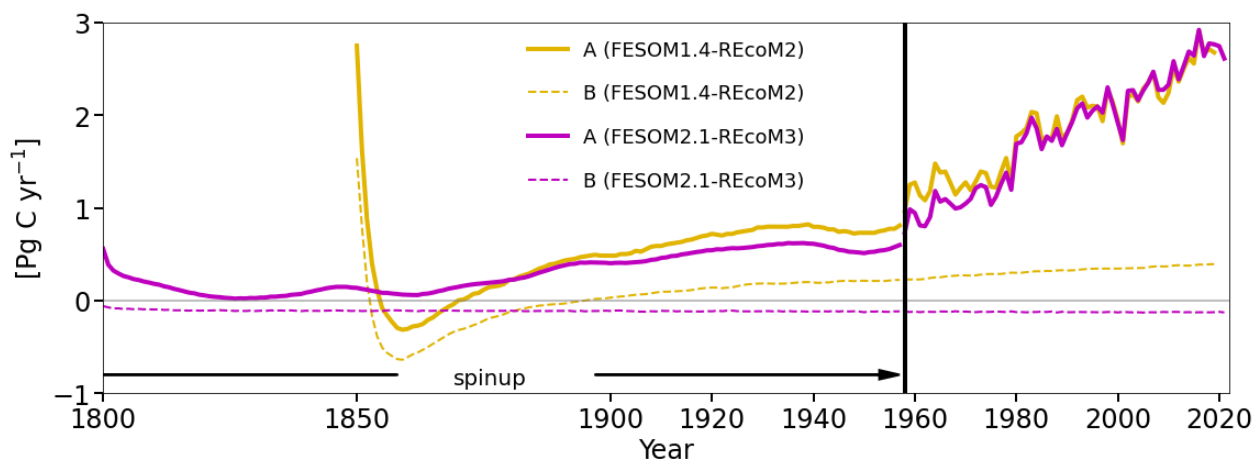
Figure 18. Time-series of simulated annual mean global ocean-atmosphere CO_2 flux in PgC yr^{-1} in the experiments conducted in this study. FESOM-2.1-REcoM3 spinup was conducted for 347 years (including 189 years of pre-spinup, not shown in the plot) under repeat year forcing taken from the year 1961 (RYF61). Here we show the spin-up since 1800 that is continued as the control simulation B after 1958 for FESOM-1.4-REcoM2 (yellow) and FESOM-2.1-REcoM3 (magenta) with a constant CO_2 concentration of 278 ppm (dashed lines) and the spin-up under increasing CO_2 that is continued as simulation A after 1958 (solid lines). The control simulation B started in the year 1958 and was conducted for 64 years with RYF61 (dashed lines). Simulation A also started in 1958 and was forced with inter-annual varying forcing JRA55-do-1.4.0 (solid lines). Please note that spinup period for FESOM1.4-REcoM2 and FESOM2.1-REcoM3 differ from each other, the latter being longer than the former.

We continue our investigation with the analysis of the global ocean-atmosphere CO_2 flux time-series (Fig. 18). In 1800, the first year of spinup after the first 189 years of pre-spinup of simulation B (not shown), the global ocean-atmosphere CO_2 flux

495 was already in a stable state and converged towards a value close to zero. Under the assumption that the ocean and atmosphere were in equilibrium at constant preindustrial CO_2 and without riverine carbon transported into the ocean (Aumont et al., 2001; Resplandy et al., 2018; Regnier et al., 2022), an equilibrium flux of zero is expected for simulation B. Any deviation from this can be considered a bias (Hauck et al., 2020). The global bias of the annual air-sea CO_2 flux in the FESOM-2.1-REcoM3 control simulation amounts to -0.12 PgC yr^{-1}, and could be further reduced towards zero with a longer spin-up. The control

500 simulation conducted with the older model version FESOM1.4 had a larger bias with a positive flux of around 0.4 PgC yr^{-1} at the end of the simulation. In addition to the bias, the drift is reduced from 0.00264 PgC yr^{-2} in FESOM1.4-REcoM2 to -0.00011 PgC yr^{-2} in FESOM2.1-REcoM3 with longer spin-up. Despite different spinup procedures (FESOM1.4 has a shorter spin-up period), simulation A with both FESOM2.1 and FESOM1.4 reveals similar CO_2 fluxes under interannually varying forcing after 1980, which indicates a dominance of the forcing over the initial conditions. This also questions the common

505 assumption that the same bias occurs in the control and historical simulations.
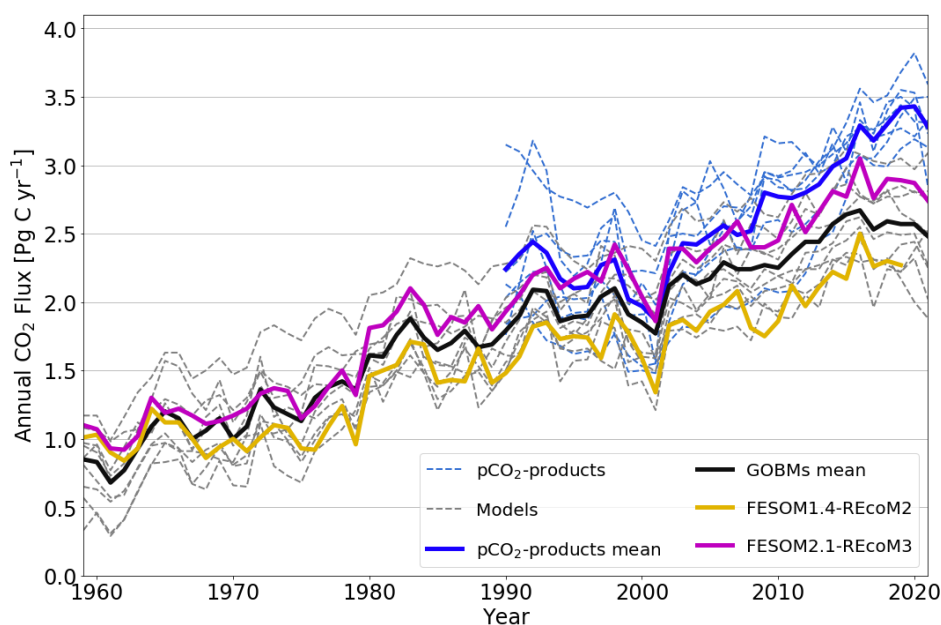
Figure 19. Globally integrated annual air-sea CO_2 flux from Global Ocean Biogeochemistry Models (GOBMs) and pCO_2-based data-products used in the Global Carbon Budget 2022, after applying bias correction to the models and river flux adjustment of 0.65 PgC yr^{-1} (Regnier et al., 2022) to the pCO_2-products. The thick black line indicates the model ensemble mean and the thick blue line shows the mean of the pCO_2-product ensemble. Thin dashed lines are from individual models and pCO_2-products. FESOM2.1-REcoM3 (magenta) shows the ocean carbon flux for the period of 1959-2021 whereas FESOM1.4-REcoM2 (yellow) covers the period of 1959-2019. Positive numbers indicate a flux into the ocean.

We next assess the model performance of the interannually varying simulation (A) by comparison with the Global Carbon Budget's ensemble of pCO_2-based data-products and other ocean biogeochemistry models (Fig. 19). Note that all model time

series shown in Fig. 19 are referenced relative to their control simulations. Although being consistent with the interannual variability, air-sea CO_2 fluxes of FESOM1.4 are at the lower end of the range compared to other Global Ocean Biogeochemistry

510 Models and pCO_2-based estimates. In contrast, starting from the mid-1960s, FESOM2.1 shows a higher CO_2 flux in comparison to FESOM1.4. Considering the fact that both model versions do not depart much from each other in simulation A, the increase in net CO_2 flux is mostly attributed to the level of CO_2 fluxes in their control simulations with a constant atmospheric CO_2 concentration and without climate-change forcing (simulation B; Fig. 18).

After accounting for the bias in simulation B, the simulated ocean carbon sink is 1.74 ± 0.11 PgC yr^{-1} and 2.17 ± 0.13 PgC yr^{-1}

515 for FESOM1.4-REcoM2 and FESOM2.1-REcoM3 versions between 1990 and 1999, respectively. Hence, FESOM2.1-REcoM3 is closer to the best estimate for the 1990s (2.2 ± 0.4 PgC yr^{-1}, IPCC, Denman et al., 2007; Ciais et al., 2014) than FESOM1.4-REcoM2. The cumulative uptake over the period of 1959-2019 amounts to 93.4 PgC (FESOM1.4-REcoM2) and 116.6 PgC (FESOM2.1-REcoM3) which is a 25% increase in CO_2 flux. Yet, the FESOM2.1-REcoM3 CO_2 fluxes are lower than the mean of the pCO_2-based data-products since about 2008 and thus affirm the growing discrepancy between global ocean bio-

520 geochemistry models and pCO_2-products (Friedlingstein et al., 2022a).

3.3.3 DIC Inventory Changes

Table 4. FESOM2.1-REcoM3 DIC inventory for simulation A (PgC) in 1994, and change in DIC inventory between 1800-1994 and 1994-2007. The FESOM-2.1-REcoM3 numbers are from simulation A and hence encompass anthropogenic and natural carbon cycle processes. Gruber et al. (2019) estimate the anthropogenic carbon inventory change. We have given the Gruber et al. (2019) anthropogenic plus back-of-the-envelope natural carbon inventory changes in parenthesis (only available for global).

	Year	Global	North	Tropics	South
FESOM-2.1-REcoM3	1994	38167.4	5259.8	21108.1	11799.5
FESOM-2.1-REcoM3	1800 to 1994	91.6	14.5	35.5	41.6
FESOM-2.1-REcoM3	1994 to 2007	27.7	5.2	11.6	11.0
Sabine et al. (2004), (Gruber et al., 2019)	1800 to 1994	118±19 (111±21)	25.1	46.6	48.0
Gruber et al. (2019)	1994 to 2007	34±4 (29±5)	5.9	17.5	10.4

The interior ocean DIC inventory in FESOM-2.1 amounts to about 38,200 PgC, which is in the reported range of 37,200 to 39,000 PgC (Sundquist, 1985; Keppler et al., 2020). The DIC inventory grew over time in accordance with observation-based estimates (Table 4, Sabine et al., 2004; Gruber et al., 2019). The increase from 1994-2007 is with 27.7 PgC slightly lower than

525 the best estimate by Gruber et al. (2019), which, however, only quantifies the anthropogenic CO_2 increase (34±4 PgC). The model estimate falls within the uncertainty range of Gruber et al. (2019) when considering in addition the poorly constrained response of the natural carbon inventory to climate change (29±5 PgC). Similarly, the simulated DIC inventory change 1800-1994 (91.6 PgC) is at the lower end but within the reported uncertainty of the observation-based total DIC inventory change (111±21 PgC). FESOM-2.1-REcoM3 is thus one of the few ocean biogeochemistry models that falls within the range of

530 interior ocean anthropogenic carbon accumulation that is also supported by O_2/N_2 ratios (Tohjima et al., 2019) and atmospheric inversions (see also discussion in Friedlingstein et al., 2022b). Notably, FESOM2.1-REcoM3 can reproduce the latitudinal distribution of anthropogenic carbon accumulation 1994-2007 with the maximum in the tropics (30°S-30°N), followed by the Southern Ocean south of 30°S, and the North (north of 30°N), although it also also underestimates the accumulation in the tropics, as most other models do (Friedlingstein et al., 2022a). If the observation-based separation into North, Tropics and
535 South is correct, this may indicate a too weak transport of anthropogenic carbon from the Southern Ocean into the tropics, or a generally too weak CO_2 uptake in the tropics.

3.4 Oxygen
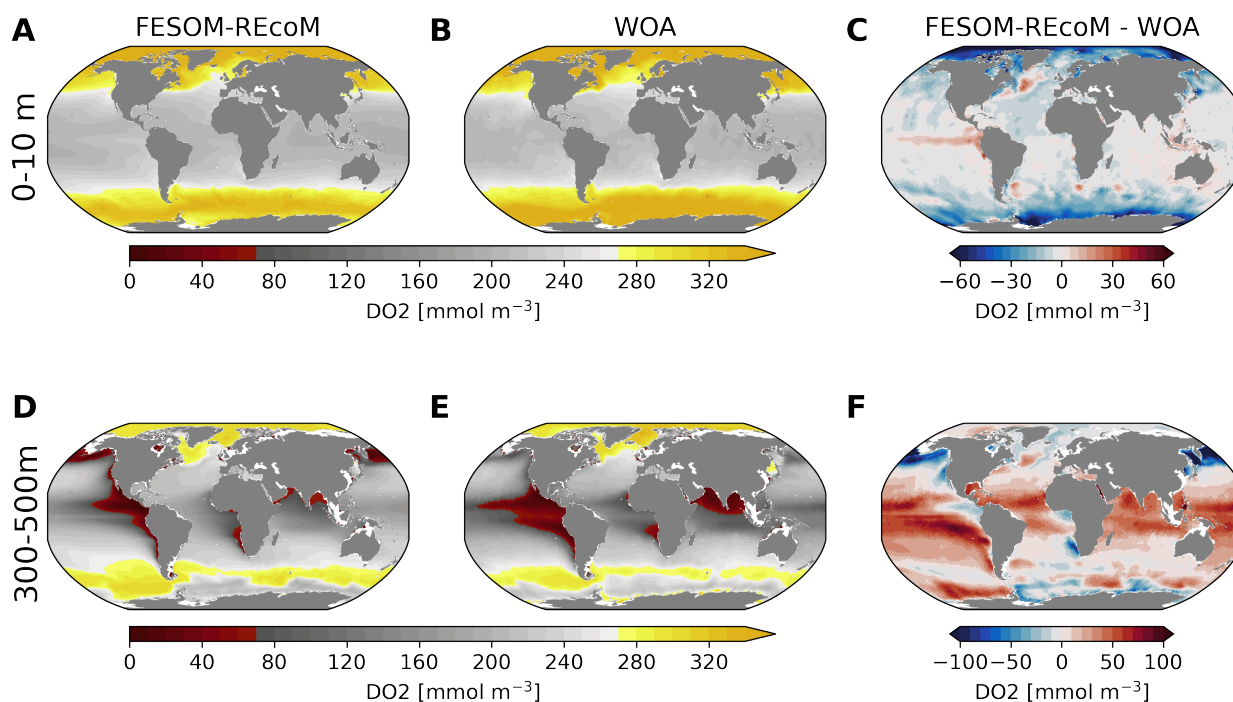
Figure 20. Maps of surface (0-10m, top row) and intermediate (300-500m, bottom row) concentration of simulated FESOM2.1-REcoM3 dissolved O_2 [mmol m^{-3}] (A, D), World Ocean Atlas 2018 climatology of dissolved O_2 (B, E; (Garcia et al., 2019b)) and corresponding differences (C, F) over the time period 2012-2021.

The simulated global O_2 concentration distribution at the surface ocean and intermediate depths was consistent with observed patterns in WOA2018 (Fig. 20). The model successfully reproduced the typical spatial patterns (Schmidtko et al.,
540 2017): (1) Oxygen Minimum Zones in the western boundary upwelling systems where old deoxygenated waters are brought to the surface, (2) high concentrations in the high latitude regions where cold temperature increases oxygen solubility (Arctic and Southern Oceans), and (3) moderate oxygen concentrations in the more stratified tropical gyres. Nevertheless, there

were regional discrepancies. At the surface, the model slightly underestimated O_2 concentrations in the high latitude surface ocean. At intermediate depth, the model generally overestimated oxygen levels, especially in the Pacific Ocean and the

545   sub-polar Southern Ocean with biases exceeding 100 mmol m^{-3}. Compared to other models which compared oxygen concentrations within the 100-600 m layer (Cocco et al., 2013), REcoM3 performed remarkably well with simulated values of about 160±105 mmol m^{-3}, which is very close to the observations from the WOA (158±103 mmol m^3).

4   Conclusions and Outlook

We have presented a new coupled ocean biogeochemistry model FESOM2.1-REcoM3. Building upon finite volumes for the

550   ocean component improves the numerical efficiency and leads to higher numerical throughput of the coupled model (Danilov et al., 2017). Furthermore, the biogeochemistry component was extended to incorporate state of the art carbonate chemistry routines, a second zooplankton and detritus group and simulates the cycling of oxygen in the ocean. In its present configuration, the overall realism of FESOM2.1-REcoM3 in simulating the observed mean biogeochemical state is comparable to that of most GOBMs, while being among the more realistic models for estimating global ocean anthropogenic carbon uptake. There are

555   still a number of model shortcomings, such as a lower simulated NPP and regional misfit between the annual mean CO_2 flux of the model simulation and the pCO_2-based data-product that will be addressed in the future.

This model set-up provides the basis for further model development, e.g., the inclusion of coccolithophores as an additional phytoplankton functional type and CO_2 sensitivities of phytoplankton growth (Seifert et al., 2022), as well as the separation of the generic small zooplankton group into micro- and mesozooplankton that reduces model biases in nutrient fields, increases

560   net primary production and better captures the top-down control on phytoplankton bloom phenology (Karakuş et al., 2022). We further plan to incorporate more detailed iron biogeochemistry as developed in REcoM coupled to MITgcm (e.g., Ye et al., 2020), and the explicit representation of the effects of viscosity and ballasting on particle sinking speed, as well as oxygen-dependent remineralization, following Cram et al. (2018) to address knowledge gaps in carbon export and transfer to depth (Henson et al., 2022). Other on-going work addresses the role of rivers for carbon and nutrient transport into the ocean and

565   the remineralization time-scale of this river-derived organic material (Aumont et al., 2001; Lacroix et al., 2020; Regnier et al., 2022), and thus tackles a major uncertainty in the ocean carbon cycle and comparison of ocean carbon sink estimates based on pCO_2-products and ocean biogeochemistry models (e.g., Hauck et al., 2020).

Code availability. The FESOM2.1-REcoM3 source code is available at https://github.com/FESOM/fesom2/tree/fesom2.1_recom (last access: 31 December 2022); the version of FESOM2.1-REcoM3 used for this paper can be found at https://doi.org/10.5281/zenodo.7502419.

570   A manual is available at: https://recom.readthedocs.io/en/latest/.

Author contributions. Conceptualization was done by OG, LO, CV and JH. Data were prepared by OG, JH, and OK. Analysis of simulations and visualization was done by all authors. All authors contributed to writing of the paper.

Competing interests. The authors declare no competing interests.

Acknowledgements. This research was supported under the Initiative and Networking Fund of the Helmholtz Association (Helmholtz Young
575 Investigator Group Marine Carbon and Ecosystem Feedbacks in the Earth System [MarESys], grant number VH-NG-1301). LO has received
funding from the European Union's Horizon 2020 research and innovation program under grant agreement number 820989 (project COM-
FORT) and from the Germany Ministry for Education and Research (BMBF) project nuArctic (grant no. 03F0918A). MZ is funded by the
Deutsche Forschungsgemeinschaft (DFG, German Research Foundation) – Projektnummer 268020496 – TRR 172, within the Transregional
Collaborative Research Center "ArctiC Amplification: Climate Relevant Atmospheric and SurfaCe Processes, and Feedback Mechanisms
580 (AC)[3]. We thank Dr. Sergey Danilov from AWI Bremerhaven, Germany, and Dr. Martin Butzin from MARUM, Bremen for helpful support.
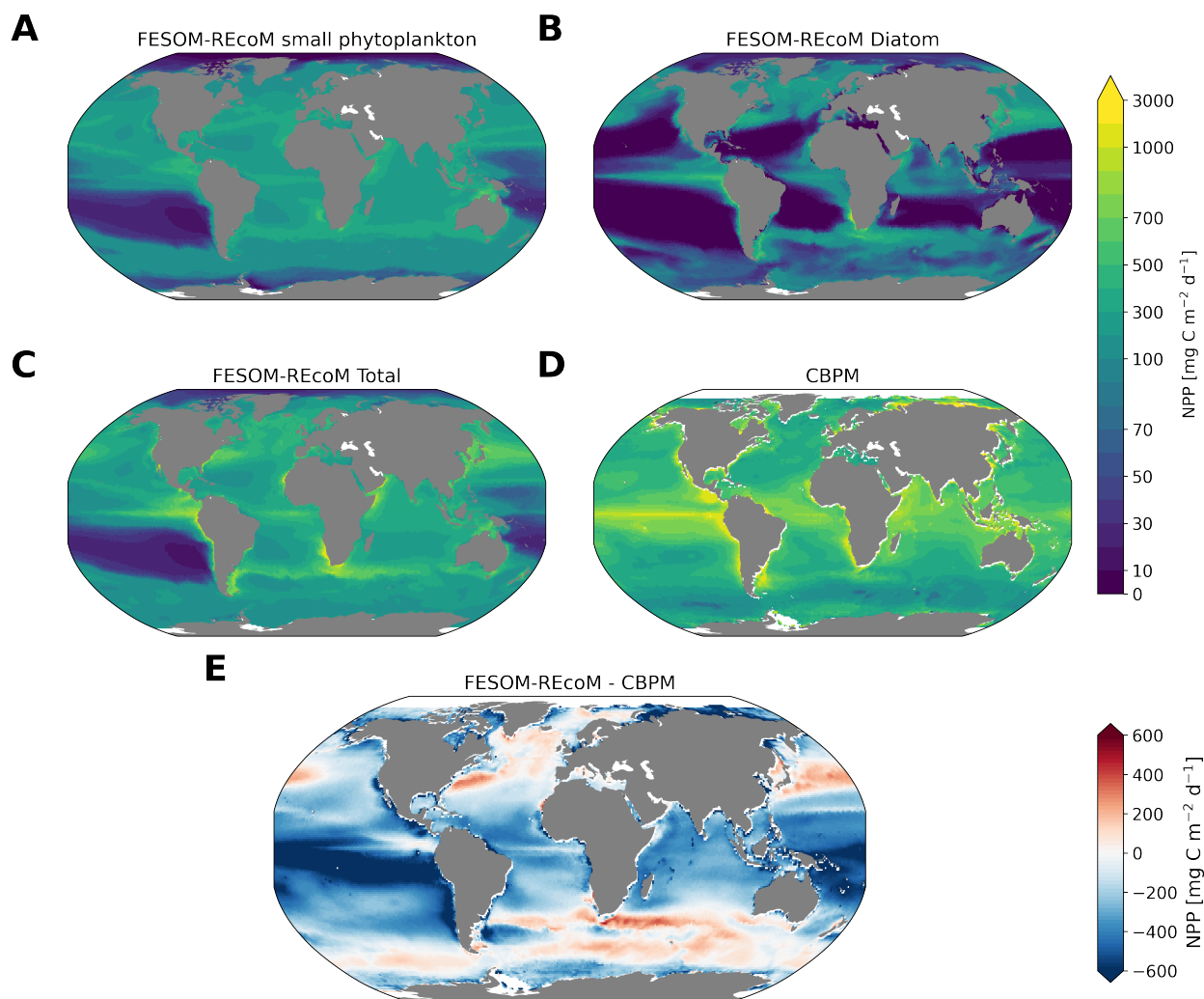
Figure A1. Maps of simulated FESOM2.1-REcoM3 (simA) vertically integrated net primary production [mgC m^{-2} d^{-1}] of small phytoplankton (A), diatoms (B), and the sum of both phytoplankton groups (C). The satellite-based Carbon-based Productivity Model (CbPM) is shown in (D; Westberry et al., 2008) with corresponding differences between FESOM2.1-REcoM3 and VGPM (E). All fields are averaged over the time period 2012 to 2021.
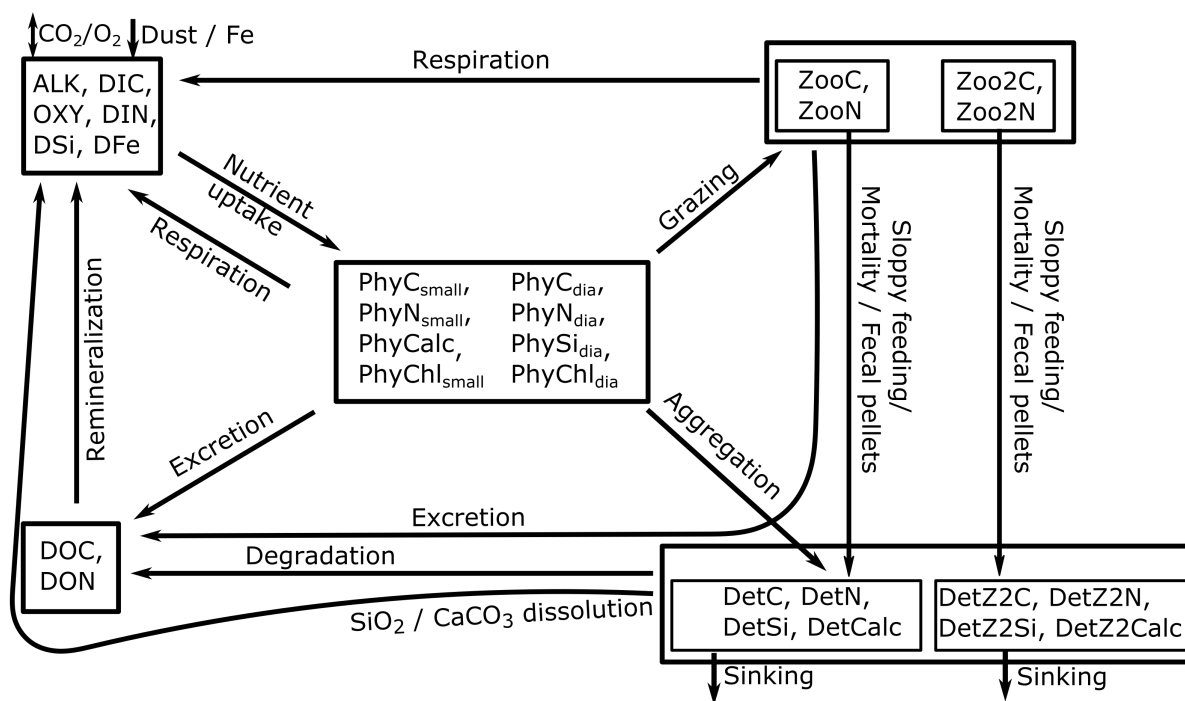
Figure A2. Conceptual diagram of the ocean biogeochemical model REcoM3. The 28 tracers can be grouped (indicated by boxes) into dissolved nutrients, carbonate system parameters and oxygen (upper left), phytoplankton functional types (center), zooplankton functional types (upper right), two detritus classes (lower right), and dissolved organic material (lower left). Source and sink terms are depicted by arrows. For reasons of diagrammatic clarity, connections of dissolved oxygen (Oxy) to other state variables are omitted here. Similarly, the release of alkalinity, dissolved inorganic nutrients and organic matter from the sediment are not shown.

Appendix A: Equations

This appendix provides an overview of the underlying model equations and lists all biogeochemical variables of FESOM2.1-REcoM3. Changes in state variables in REcoM3 are controlled by biological and chemical processes, in addition to the changes induced by ocean circulation, mixing, diffusion and advection computed by FESOM2.1. While some variables exchange across
585 the ocean surface and/or the sea floor, others, like dead organic matter (detritus) sink through the water column. The concentration change for a state variable S is formulated as follows:

$$\frac{\partial S}{\partial t} \;=\; -\mathbf{U} \cdot \nabla S + \nabla \cdot (\kappa \cdot \nabla S) + SMS(S), \tag{A1}$$

where S is the volumetric concentration of a state variable, $\mathbf{U}$ is the three-dimensional advection velocity and κ is the diffusivity. The term $SMS(S)$ represents the biogeochemical sources minus sinks. The slow-sinking detritus class is assumed to sink
590 with a velocity, which increases linearly with depth as a first-order description of the shift to larger and faster-sinking particles with increasing depth (Kriest and Oschlies, 2008). A constant sinking rate is applied to the fast-sinking detritus class. REcoM3 has 28 oceanic and four explicit benthic state variables (Tables A1 and A2).

A1 Sources minus sinks

A1.1 Nutrients

595 A1.1.1 Dissolved inorganic nitrate (DIN)

The simulated DIN conceptually represents the concentrations of nitrate, nitrite and ammonia, while in practice only nitrate is considered. The concentration of DIN in the water column rises when DON is remineralized and diminishes as a consequence of assimilation by small phytoplankton and diatoms:

$$\text{SMS(DIN)} = \underbrace{\rho_{\text{DON}} \cdot f_T \cdot \text{DON}}_{\text{DON remineralization}} - \underbrace{\text{V}^{\text{N}}_{\text{small}} \cdot \text{PhyC}_{\text{small}}}_{\text{N-assimilation, small phytoplankton}} - \underbrace{\text{V}^{\text{N}}_{\text{dia}} \cdot \text{PhyC}_{\text{dia}}}_{\text{N-assimilation, diatoms}} . \tag{A2}$$

600 The state variables DON, $\text{PhyC}_{\text{small}}$ and PhyC_{dia} are listed in Table A1. The value of the remineralization rate constant (ρ_{DON}) is given in Table A8. The temperature dependency of remineralization (f_T) is calculated in Eq. A43. See Section A3.4 for details on the carbon-specific nitrogen-assimilation rates $\text{V}^{\text{N}}_{\text{small}}$ and $\text{V}^{\text{N}}_{\text{dia}}$ (Table A5).

A1.1.2 Dissolved silicic acid (DSi)

silicon assimilation (Si-assimilation) and increases when biogenic silica from one of the two detritus classes dissolves.

$$605 \quad \text{SMS(DSi)} = \underbrace{\rho^T_{\text{Si}} \cdot \text{DetSi}}_{\text{Remineralization, slow-sinking detritus}} + \underbrace{\rho^T_{\text{Si}} \cdot \text{DetZ2Si}}_{\text{Remineralization, fast-sinking detritus}} - \underbrace{\text{V}^{\text{Si}} \cdot \text{PhyC}_{\text{dia}}}_{\text{Si-assimilation, diatoms}} \tag{A3}$$

The state variables PhyC_{dia}, DetSi and DetZ2Si are listed in Table A1. The temperature dependent remineralization rate of silicon (ρ^T_{Si}) and the carbon-specific Si-assimilation rate (V^{Si}) are calculated in Eqs. A45 and A51, respectively (Table A5).

A1.1.3 Dissolved iron (DFe)

Excretion of phyto- and zooplankton and remineralization of detritus release iron with a fixed iron:nitrate ratio ($q^{\mathrm{Fe:N}}$). Unlike
610 for nitrogen, which is released as dissolved organic nitrogen and needs to be remineralized further to become available as nu-
trient again, the released iron is directly put into the dissolved pool iron, basically assuming that all dissolved iron is ultimately
bio-available. Iron assimilation (again assumed to be proportional to nitrogen assimilation, from now on N-assimilation) by
both phytoplankton classes lower the level of dissolved iron. In addition, free inorganic iron Fe' is scavenged onto sinking
particles, with a rate that is proportional to particle concentration. We take detrital carbon as a proxy for the mass of sinking
615 particles.

$$
\begin{aligned}
\mathrm{SMS}(\mathrm{DFe}) = q^{\mathrm{Fe:N}} \cdot (\,&\underbrace{\epsilon^{\mathrm{N}}_{\mathrm{phy}} \cdot f^{\mathrm{N:Cmax}}_{\mathrm{lim,\,small}} \cdot \mathrm{PhyN_{small}}}_{\text{Excretion, small phytoplankton}} + \underbrace{\epsilon^{\mathrm{N}}_{\mathrm{phy}} \cdot f^{\mathrm{N:Cmax}}_{\mathrm{lim,\,dia}} \cdot \mathrm{PhyN_{dia}}}_{\text{Excretion, diatoms}} \\
+ \; &\underbrace{\rho_{\mathrm{DetN}} \cdot f_T \cdot \mathrm{DetN}}_{\text{Remineralization, slow-sinking detritus}} + \underbrace{\rho_{\mathrm{DetN}} \cdot f_T \cdot \mathrm{DetZ2N}}_{\text{Remineralization, fast-sinking detritus}} \\
+ \; &\underbrace{\epsilon^{\mathrm{N}}_{\mathrm{zoo}} \cdot \mathrm{ZooN}}_{\text{Excretion, small zooplankton}} + \underbrace{\epsilon^{\mathrm{N}}_{\mathrm{zoo2}} \cdot \mathrm{Zoo2N}}_{\text{Excretion, macrozooplankton}} \\
- \; &\underbrace{\mathrm{V}^{\mathrm{N}}_{\mathrm{small}} \cdot \mathrm{PhyC_{small}}}_{\text{N-assimilation, small phytoplankton}} - \underbrace{\mathrm{V}^{\mathrm{N}}_{\mathrm{dia}} \cdot \mathrm{PhyC_{dia}}}_{\text{N-assimilation, diatom}}) \\
- \; &\underbrace{\kappa_{\mathrm{Fe}} \cdot \mathrm{DetC} \cdot \mathrm{Fe'}}_{\text{Scavenging, slow-sinking detritus}} - \underbrace{\kappa_{\mathrm{Fe}} \cdot \mathrm{DetZ2C} \cdot \mathrm{Fe'}}_{\text{Scavenging, fast-sinking detritus}}
\end{aligned}
\tag{A4}
$$

The state variables $\mathrm{PhyC_{small}}$, $\mathrm{PhyC_{dia}}$, $\mathrm{PhyN_{small}}$, $\mathrm{PhyN_{dia}}$, DetC, DetN, $\mathrm{DetZ2C}$, $\mathrm{DetZ2N}$, ZooN, $\mathrm{Zoo2N}$ are listed in
Table A1. Intracellular Fe : N ratio ($q^{\mathrm{Fe:N}}$) and scavenging rate of iron (κ_{Fe}) are given in Table A4. Excretion rates ($\epsilon^{\mathrm{N}}_{\mathrm{phy}}$,
$\epsilon^{\mathrm{N}}_{\mathrm{zoo}}$ and $\epsilon^{\mathrm{N}}_{\mathrm{zoo2}}$) and the degradation rate for detritus N (ρ_{DetN}) are listed in Table A8. The temperature dependency (f_T) is
620 calculated in Eq. A43. The limitation by intracellular nitrogen ($f^{\mathrm{N:Cmax}}_{\mathrm{lim\,small}}$, $f^{\mathrm{N:Cmax}}_{\mathrm{lim\,dia}}$) is described in Eq. A55. Scavenging is
calculated following Parekh et al. (2004). The total concentration of dissolved iron ($\mathrm{Fe_T}$) is separated into free iron ($\mathrm{Fe'}$) and
iron complexed with organic ligands ($\mathrm{Fe_L}$), which is not scavenged. Complexation reactions are fast (Tagliabue and Völker,
2011), so we assume instantaneous equilibrium between free iron and free ligand ($\mathrm{L'}$) which is computed using a constant
$K_{\mathrm{Fe_L}} = \frac{[\mathrm{Fe'}] \cdot [\mathrm{L'}]}{[\mathrm{Fe_L}]}$, by solving

625 $$\mathrm{Fe_T} = \mathrm{Fe'} + \mathrm{Fe_L} \qquad \mathrm{L_T} = \mathrm{Fe_L} + \mathrm{L'} \tag{A5}$$

For simplicity we assume here a constant total ligand concentration $\mathrm{L_T}$, unlike in Völker and Tagliabue (2015). Variable ligand
concentration, like in Misumi et al. (2011) or Völker and Tagliabue (2015), or variable ligand binding strength, like in Ye et al.
(2020) will be explored in the future. The values for $K_{\mathrm{Fe_L}}$ and $\mathrm{L_T}$ are listed in Table A4.

A1.2 Carbon cycle

A1.2.1 Dissolved inorganic carbon (DIC)

DIC concentration increases with respiration of phyto- and zooplankton, remineralization of semi-labile dissolved organic carbon, dissolution of calcitic detritus and dissolution of $CaCO_3$ in zooplankton guts. Loss terms are carbon fixation by primary producers and the formation of calcium carbonate. In addition, sea–air flux of CO_2 leads to an exchange of carbon with the atmosphere, depending on the partial pressure difference of CO_2 between ocean and atmosphere. This exchange is treated separately as a boundary condition. The partial pressure of surface ocean CO_2 is computed using the mocsy-2.0 routines (Orr and Epitalon, 2015).

$$
\begin{aligned}
\mathrm{SMS(DIC)} = & \underbrace{(r_{\mathrm{small}} - P_{\mathrm{small}}) \cdot \mathrm{PhyC}_{\mathrm{small}}}_{\text{Net respiration, small phytoplankton}} + \underbrace{(r_{\mathrm{dia}} - P_{\mathrm{dia}}) \cdot \mathrm{PhyC}_{\mathrm{dia}}}_{\text{Net respiration, diatom}} + \underbrace{\rho_{\mathrm{DOC}} \cdot f_T \cdot \mathrm{DOC}}_{\text{Remineralization of DOC}} \\
& + \underbrace{r_{\mathrm{zoo}} \cdot \mathrm{ZooC}}_{\text{Respiration, small zoo}} + \underbrace{r_{\mathrm{zoo2}} \cdot \mathrm{Zoo2C}}_{\text{Respiration, macrozoo}} + \underbrace{\mathrm{Diss}_{\mathrm{calc}} \cdot \mathrm{DetCalc}}_{\text{Calcite dissolution, slow-sinking detritus}} + \underbrace{G^{\mathrm{zoo}}_{\mathrm{small}} \cdot q^{\mathrm{CaCO_3:N}}_{\mathrm{small}} \cdot \mathrm{Diss}_{\mathrm{calc\_guts}}}_{CaCO_3 \text{ dissolution in guts, small zoo}} \\
& - \underbrace{\psi \cdot P_{\mathrm{small}} \cdot \mathrm{PhyC}_{\mathrm{small}}}_{\text{Calcification}} + \underbrace{\mathrm{Diss}_{\mathrm{calc2}} \cdot \mathrm{DetZ2Calc}}_{\text{Calcite dissolution, fast-sinking detritus}} + \underbrace{G^{\mathrm{zoo2}}_{\mathrm{small}} \cdot q^{\mathrm{CaCO_3:N}}_{\mathrm{small}} \cdot \mathrm{Diss}_{\mathrm{calc\_guts}}}_{CaCO_3 \text{ dissolution in guts, macrozoo}}
\end{aligned} \tag{A6}
$$

The state variables $\mathrm{PhyC}_{\mathrm{small}}$, $\mathrm{PhyC}_{\mathrm{dia}}$, DOC, ZooC, $\mathrm{Zoo2C}$, $\mathrm{DetCalc}$, $\mathrm{DetZ2Calc}$ are listed in Table A1. Respiration rate constants of small phytoplankton (r_{small}), diatoms (r_{dia}) and zooplankton groups (r_{zoo} and r_{zoo2}) are computed in Sections A3.2 and A4.1, respectively. Photosynthesis terms (P_{small} and P_{dia}) are calculated in Eq. A46. The remineralization rate constant (ρ_{DOC}) is listed in Table A8 and the temperature dependency (f_T) is given in Eq. A43. Calcite dissolution by detritus ($\mathrm{Diss}_{\mathrm{calc}}$, $\mathrm{Diss}_{\mathrm{calc2}}$) is calculated in Eq. A38. The constant for dissolution of calcium carbonate in zooplankton guts ($\mathrm{Diss}_{\mathrm{calc\_guts}}$) is listed in Table A5. $G^{\mathrm{zoo}}_{\mathrm{small}}$ and $G^{\mathrm{zoo2}}_{\mathrm{small}}$ are grazing terms and explained in Section A4.2. The value of the calcite production ratio (ψ) is given in Table A3.

A1.2.2 Total alkalinity (Alk)

The balance of alkalinity is affected by primary production, remineralization of dissolved organic matter, dissolution of calcitic detritus and dissolution of $CaCO_3$ in zooplankton guts. Alkalinity increases when nitrogen is assimilated and when $CaCO_3$ is dissolved (Wolf-Gladrow et al., 2007). Simultaneously, it is reduced by calcification as well as remineralization of dissolved organic nitrogen. The effect of phosphate assimilation and remineralization onto alkalinity is taken into account assuming a constant N:P Redfield ratio (16:1).

$$\mathrm{SMS(Alk)} = (1+1/16)\cdot \underbrace{\mathrm{V^N_{small}}\cdot \mathrm{PhyC_{small}}}_{\text{N-assimilation, small phytoplankton}} + (1+1/16)\cdot \underbrace{\mathrm{V^N_{dia}}\cdot \mathrm{PhyC_{dia}}}_{\text{N-assimilation, diatom}} \tag{A7}$$

$$- (1+1/16)\cdot \underbrace{\rho_{\mathrm{DON}}\cdot f_T \cdot \mathrm{DON}}_{\text{Remineralization of DON}} - 2\cdot \underbrace{\psi \cdot P_{\mathrm{small}}\cdot \mathrm{PhyC_{small}}}_{\text{Calcification}}$$

$$+ 2\cdot \underbrace{\mathrm{Diss_{calc}}\cdot \mathrm{DetCalc}}_{\text{Calcite dissolution, slow-sinking detritus}} + 2\cdot \underbrace{G^{\mathrm{zoo}}_{\mathrm{small}}\cdot q^{\mathrm{CaCO_3:N}}_{\mathrm{small}}\cdot \mathrm{Diss_{calc\_guts}}}_{CaCO_3\ \text{dissolution in guts, small zoo}} \tag{A8}$$

$$+ 2\cdot \underbrace{\mathrm{Diss_{calc2}}\cdot \mathrm{DetZ2Calc}}_{\text{Calcite dissolution, fast-sinking detritus}} + 2\cdot \underbrace{G^{\mathrm{zoo2}}_{\mathrm{small}}\cdot q^{\mathrm{CaCO_3:N}}_{\mathrm{small}}\cdot \mathrm{Diss_{calc\_guts}}}_{CaCO_3\ \text{dissolution in guts, macrozoo}}$$

655 The state variables $\mathrm{PhyC_{small}}$, $\mathrm{PhyC_{dia}}$, DON, $\mathrm{DetCalc}$, $\mathrm{DetZ2Calc}$ are listed in Table A1. The N-assimilation ($\mathrm{V^N_{small}}$ and $\mathrm{V^N_{dia}}$) is calculated in Section A3.4. The remineralization rate constant (ρ_{DON}) is given in Table A8. The temperature dependency (f_T) is calculated in Eq. A43. The value of the calcite production ratio (ψ) is given in Table A3. The photosynthesis term (P_{small}) is calculated in Eq. A46. The calcite dissolution by detritus ($\mathrm{Diss_{calc}}$, $\mathrm{Diss_{calc2}}$) is calculated in Eq. A38. Dissolution of calcium carbonate in guts ($\mathrm{Diss_{calc\_guts}}$) is listed in Table A5. $G^{\mathrm{zoo}}_{\mathrm{small}}$ and $G^{\mathrm{zoo2}}_{\mathrm{small}}$ are grazing terms and explained in Section A4.2.

A1.3 Phytoplankton

A1.3.1 Nitrogen

The phytoplankton nitrogen pools increase through N-assimilation. The assimilation process is assumed to be proportional to carbon biomass, with a carbon-specific uptake rate that depends on the C:N ratio of phytoplankton and the external DIN concentration (Geider et al., 1998). Excretion of biogenic nitrogen to semi-labile DON drains the pool. At high intracellular $\mathrm{C:N}$

665 ratio, excretion is downregulated. Aggregation and grazing by the two zooplankton groups transfer nitrogen to the zooplankton and detritus pools.

$$\mathrm{SMS(PhyN_{small})} = \underbrace{\mathrm{V^N_{small}}\cdot \mathrm{PhyC_{small}}}_{\text{N-assimilation}} \tag{A9}$$

$$- \underbrace{\epsilon^{\mathrm{N}}_{\mathrm{phy}}\cdot f^{\mathrm{N:Cmax}}_{\mathrm{lim,small}}\cdot \mathrm{PhyN_{small}}}_{\text{DON excretion}} - \underbrace{\mathrm{Agg}\cdot \mathrm{PhyN_{small}}}_{\text{Aggregation loss}} - \underbrace{G^{\mathrm{zoo}}_{\mathrm{small}}}_{\text{Grazing loss by small zoo}} - \underbrace{G^{\mathrm{zoo2}}_{\mathrm{small}}}_{\text{Grazing loss by macrozoo}} \tag{A10}$$

$$\mathrm{SMS(PhyN_{dia})} = \underbrace{\mathrm{V^N_{dia}}\cdot \mathrm{PhyC_{dia}}}_{\text{N-assimilation}} \tag{A11}$$

670
$$- \underbrace{\epsilon^{\mathrm{N}}_{\mathrm{phy}}\cdot f^{\mathrm{N:Cmax}}_{\mathrm{lim,dia}}\cdot \mathrm{PhyN_{dia}}}_{\text{DON excretion}} - \underbrace{\mathrm{Agg}\cdot \mathrm{PhyN_{dia}}}_{\text{Aggregation loss}} - \underbrace{G^{\mathrm{zoo}}_{\mathrm{dia}}}_{\text{Grazing loss by small zoo}} - \underbrace{G^{\mathrm{zoo2}}_{\mathrm{dia}}}_{\text{Grazing loss by macrozoo}} \tag{A12}$$

The state variables $\mathrm{PhyC_{small}}$, $\mathrm{PhyN_{small}}$, $\mathrm{PhyC_{dia}}$, and $\mathrm{PhyN_{dia}}$ are listed in Table A1. The N-assimilation ($\mathrm{V^N_{small}}$ and $\mathrm{V^N_{dia}}$) is explained in Section A3.4. The constant excretion rate constant ($\epsilon^{\mathrm{N}}_{\mathrm{phy}}$) is given in Table A8. When the C:N ratio of the cells becomes too high, excretion of DON is downregulated by the limiter function ($f^{\mathrm{N:Cmax}}_{\mathrm{lim,small}}$, $f^{\mathrm{N:Cmax}}_{\mathrm{lim,dia}}$) that is described in Eq. A55.

Phytoplankton aggregation (Agg) defines the transfer of nitrogen into the detritus pools which depends quadratically on detris

675 and phytoplankton concentrations (Eq. A52). Grazing loss terms ($G_{\text{small}}^{\text{zoo}}$, $G_{\text{small}}^{\text{zoo2}}$, $G_{\text{dia}}^{\text{zoo}}$ and $G_{\text{dia}}^{\text{zoo2}}$) are explained in Section A4.2.

A1.3.2 Carbon

The carbon biomass of small phytoplankton and diatoms increases as a result of carbon assimilation during photosynthesis. Loss terms include excretion of DOC, which is limited by the availability of proteins as in the nitrogen pool, respiration, aggregation, and grazing.

680
$$\text{SMS}(\text{PhyC}_{\text{small}}) = \underbrace{(P_{\text{small}} - r_{\text{small}}) \cdot \text{PhyC}_{\text{small}}}_{\text{Net photosynthesis}} \tag{A13}$$

$$- \underbrace{\text{Agg} \cdot \text{PhyC}_{\text{small}}}_{\text{Aggregation loss}} - \underbrace{\epsilon_{\text{phy}}^{\text{C}} \cdot f_{\text{lim, small}}^{\text{N:Cmax}} \cdot \text{PhyC}_{\text{small}}}_{\text{Excretion of DOC}} - \underbrace{q_{\text{small}}^{\text{C:N}} \cdot G_{\text{small}}^{\text{zoo}}}_{\text{Grazing loss by small zoo}} - \underbrace{q_{\text{small}}^{\text{C:N}} \cdot G_{\text{small}}^{\text{zoo2}}}_{\text{Grazing loss by macrozoo}}$$

$$\text{SMS}(\text{PhyC}_{\text{dia}}) = \underbrace{(P_{\text{dia}} - r_{\text{dia}}) \cdot \text{PhyC}_{\text{dia}}}_{\text{Net photosynthesis}} \tag{A14}$$

$$- \underbrace{\text{Agg} \cdot \text{PhyC}_{\text{dia}}}_{\text{Aggregation loss}} - \underbrace{\epsilon_{\text{phy}}^{\text{C}} \cdot f_{\text{lim, dia}}^{\text{N:Cmax}} \cdot \text{PhyC}_{\text{dia}}}_{\text{Excretion of DOC}} - \underbrace{q_{\text{dia}}^{\text{C:N}} \cdot G_{\text{dia}}^{\text{zoo}}}_{\text{Grazing loss by small zoo}} - \underbrace{q_{\text{dia}}^{\text{C:N}} \cdot G_{\text{dia}}^{\text{zoo2}}}_{\text{Grazing loss by macrozoo}}$$

The state variables $\text{PhyC}_{\text{small}}$ and PhyC_{dia} are listed in Table A1. The photosynthesis terms (P_{small} and P_{dia}) are calculated

685 in Eq. A46. Rates of respiration by small phytoplankton (r_{small}), diatoms (r_{dia}) are explained in Section A3.2. The constant for DOC excretion rate of phytoplankton ($\epsilon_{\text{phy}}^{\text{C}}$, Table A8) is downregulated by the limiter factor ($f_{\text{lim,small}}^{\text{N:Cmax}}$, $f_{\text{lim,dia}}^{\text{N:Cmax}}$) when the N : C ratio becomes too high (Eq. A55). Phytoplankton aggregation (Agg) is calculated in Eq. A52. Grazing terms ($G_{\text{small}}^{\text{zoo}}$, $G_{\text{small}}^{\text{zoo2}}$, $G_{\text{dia}}^{\text{zoo}}$ and $G_{\text{dia}}^{\text{zoo2}}$) are explained in Section A4.2. $q^{\text{C:N}} = \text{PhyC}/\text{PhyN}$, is used to convert the grazing units from mmol N to mmol C.

690 ### A1.3.3 CaCO_3

The formation of biogenic calcium carbonate in our model is limited to coccolithophores only, which are assumed to form a constant fraction of the non-diatom phytoplankton. Formation of CaCO_3 by heterotrophs, such as foraminifera or pteropods is neglected. Biogenic CaCO_3 produced by coccolithophores is transformed into detritus CaCO_3 with all forms of organic carbon loss, i.e. organic matter excretion, respiration, aggregation and grazing. Calcifiers are assumed to comprise a certain

695 fraction of the total small phytoplankton concentration, specified by the parameter ψ (Table A3), tying the calcite production of calcifiers to the growth of small phytoplankton.

$$\text{SMS}(\text{PhyCalc}) = \underbrace{\psi \cdot P_{\text{small}} \cdot \text{PhyC}_{\text{small}}}_{\text{Calcification}} - \underbrace{r_{\text{small}} \cdot \text{PhyCalc}}_{\text{Respiration}} - \underbrace{G_{\text{small}}^{\text{zoo}} \cdot q_{\text{small}}^{\text{CaCO}_3:\text{N}}}_{\text{Grazing loss, small zoo}} - \underbrace{G_{\text{small}}^{\text{zoo2}} \cdot q_{\text{small}}^{\text{CaCO}_3:\text{N}}}_{\text{Grazing loss, macrozoo}}$$

$$- \underbrace{\epsilon_{\text{phy}}^{\text{C}} \cdot f_{\text{lim, small}}^{\text{N:Cmax}} \cdot \text{PhyCalc}}_{\text{Excretion loss}} - \underbrace{\text{Agg} \cdot \text{PhyCalc}}_{\text{Aggregation loss}} \tag{A15}$$

The state variables $\text{PhyC}_{\text{small}}$ and PhyCalc are listed in Table A1. The value of the calcite production ratio (ψ) is given in Table A3. The constant excretion rate ($\epsilon^{\text{C}}_{\text{phy}}$, Table A8) is downregulated by the limiter factor $f^{\text{N:Cmax}}_{\text{lim,small}}$ (Eq. A55) when the
700 N:C ratio becomes too high. Photosynthesis (P_{small}), respiration (r_{small}) and the aggregation of phytoplankton (Agg) rates are calculated in Eqs. A46, A48 and A52, respectively. Grazing terms ($G^{\text{zoo}}_{\text{small}}$ and $G^{\text{zoo2}}_{\text{small}}$) are explained in Section A4.2. $q^{\text{CaCO}_3:\text{N}}_{\text{small}} = \text{PhyCalc}/\text{PhyN}_{\text{small}}$ is used to convert the grazing units from mmol N to mmol CaCO_3.

A1.3.4 Diatom silicon

The silica frustule of diatoms is built through Si-assimilation, which we assume to be carbon-specific, and regulated by cellular
705 quotas (see below). Any decrease in N-biomass through excretion, grazing or aggregation leads to a corresponding transfer of silica to the detritus silica pool.

$$
\begin{aligned}
\text{SMS(PhySi)} = &\ \underbrace{\text{V}^{\text{Si}} \cdot \text{PhyC}_{\text{dia}}}_{\text{Diatom Si-assimilation}} \\
&- \underbrace{\epsilon^{\text{N}}_{\text{phy}} \cdot f^{\text{N:Cmax}}_{\text{lim,dia}} \cdot \text{PhySi}_{\text{dia}}}_{\text{Excretion to detritus}} - \underbrace{\text{Agg} \cdot \text{PhySi}_{\text{dia}}}_{\text{Aggregation loss}} - \underbrace{G^{\text{zoo}}_{\text{dia}} \cdot q^{\text{Si:N}}}_{\text{Grazing loss, small zoo}} - \underbrace{G^{\text{zoo2}}_{\text{dia}} \cdot q^{\text{Si:N}}}_{\text{Grazing loss, macrozoo}}
\end{aligned}
\tag{A16}
$$

The state variables PhyC_{dia} and $\text{PhySi}_{\text{dia}}$ are described in Table A1. Si-assimilation (V^{Si}) and aggregation rates (Agg) are
710 calculated in Eqs. A51 and A52, respectively. The constant excretion rate ($\epsilon^{\text{N}}_{\text{phy}}$, Table A8) is downregulated by the limiter factor $f^{\text{N:Cmax}}_{\text{lim,dia}}$ (Eq. A55) when the N:C ratio becomes too high. Grazing terms ($G^{\text{zoo}}_{\text{dia}}$ and $G^{\text{zoo2}}_{\text{dia}}$) are explained in Section A4.2. The intracellular ratio between diatom silicon and nitrate is defined as $q^{\text{Si:N}} = \text{PhySi}_{\text{dia}}/\text{PhyN}_{\text{dia}}$.

A1.3.5 Chlorophyll a

Chlorophyll a synthesis is structured as a function of irradiance and of N-assimilation, following Geider et al. (1998). Chloro-
715 phyll a is degraded at a light-dependent rate (See Álvarez et al. (2018)), and lost via aggregation and grazing. The grazing losses in terms of nitrogen biomass are converted to chlorophyll loss using the intracellular Chl:N ratio.

$$
\text{SMS(PhyChl}_{\text{small}}) = \underbrace{\text{S}^{\text{chl}}_{\text{small}} \cdot \text{PhyC}_{\text{small}}}_{\text{Chlorophyll } a \text{ synthesis}}
\tag{A17}
$$

$$
- \underbrace{G^{\text{zoo}}_{\text{small}} \cdot q^{\text{Chl:N}}_{\text{small}}}_{\text{Grazing loss, small zoo}} - \underbrace{G^{\text{zoo2}}_{\text{small}} \cdot q^{\text{Chl:N}}_{\text{small}}}_{\text{Grazing loss, macrozoo}} - \underbrace{\text{deg}^{\text{chl}}_{\text{small}} \cdot \text{PhyChl}_{\text{small}}}_{\text{Degradation loss}} - \underbrace{\text{Agg} \cdot \text{PhyChl}_{\text{small}}}_{\text{Aggregation loss}}
\tag{A18}
$$

$$
\text{SMS(PhyChl}_{\text{dia}}) = \underbrace{\text{S}^{\text{chl}}_{\text{dia}} \cdot \text{PhyC}_{\text{dia}}}_{\text{Chlorophyll } a \text{ synthesis}}
\tag{A19}
$$

720
$$
- \underbrace{G^{\text{zoo}}_{\text{dia}} \cdot q^{\text{Chl:N}}_{\text{dia}}}_{\text{Grazing loss, small zoo}} - \underbrace{G^{\text{zoo2}}_{\text{dia}} \cdot q^{\text{Chl:N}}_{\text{dia}}}_{\text{Grazing loss, macrozoo}} - \underbrace{\text{deg}^{\text{chl}}_{\text{dia}} \cdot \text{PhyChl}_{\text{dia}}}_{\text{Degradation loss}} - \underbrace{\text{Agg} \cdot \text{PhyChl}_{\text{dia}}}_{\text{Aggregation loss}}
\tag{A20}
$$

The state variables $\text{PhyC}_{\text{small}}$, PhyC_{dia}, $\text{PhyChl}_{\text{small}}$ and $\text{PhyChl}_{\text{dia}}$ are listed in Table A1. The chlorophyll a synthesis ($\text{S}^{\text{chl}}_{\text{small}}$, $\text{S}^{\text{chl}}_{\text{dia}}$) and the aggregation (Agg) terms are calculated in Eqs. A49 and A52, respectively. The degradation parameters ($\text{deg}^{\text{chl}}_{\text{small}}$,

$\deg_{\text{dia}}^{\text{chl}}$) are given in Table A8. Grazing terms (G_{small}^{zoo}, G_{small}^{zoo2}, G_{dia}^{zoo}, and G_{dia}^{zoo2}) are explained in Section A4.2. The conversion factor from mmol N to mg Chl a is defined as $q^{\text{Chl}\,:\,\text{N}} = \text{PhyChl/PhyN}$.

A1.4 Zooplankton

A1.4.1 Nitrogen

Both zooplankton classes increase their nitrogen biomass via grazing on phytoplankton and detritus while mortality and excretion of DON reduce it. Macrozooplankton further feeds on small zooplankton and releases nitrogen via fecal pellet production.

$$\text{SMS}(\text{ZooN}) = \underbrace{\gamma_{zoo} \cdot G_{\text{tot}}^{zoo}}_{\text{Grazing}} - \underbrace{G_{\text{zoo}}}_{\text{Grazing loss, macrozoo}} - \underbrace{m_{\text{zoo}} \cdot \text{ZooN}^2}_{\text{Mortality}} - \underbrace{\epsilon_{\text{zoo}}^{\text{N}} \cdot \text{ZooN}}_{\text{Excretion of DON}} \tag{A21}$$

$$\text{SMS}(\text{Zoo2N}) = \underbrace{\gamma_{zoo2} \cdot G_{\text{tot}}^{zoo2}}_{\text{Grazing}} - \underbrace{m_{\text{zoo2}} \cdot \text{Zoo2N}^2}_{\text{Mortality}} - \underbrace{\epsilon_{\text{zoo2}}^{\text{N}} \cdot \text{Zoo2N}}_{\text{Excretion of DON}} - \underbrace{f_{\text{n}} \cdot G_{\text{tot}}^{zoo2}}_{\text{Fecal pellet}} \tag{A22}$$

The state variables ZooN and Zoo2N are listed in Table A1. Only a fraction of the grazed phytoplankton (γ_{zoo}, γ_{zoo2}, Table A3) enters the zooplankton biomass. The rest is transferred to detritus due to sloppy feeding. The grazing terms (G_{tot}^{zoo}, G_{tot}^{zoo2}) are calculated in Section A4.2. The mortality parameter (m_{zoo}, m_{zoo2}) and fecal pellet production rate constant (f_{n}) are listed in Table A3. The DON excretion terms ($\epsilon_{\text{zoo}}^{\text{N}}$, $\epsilon_{\text{zoo2}}^{\text{N}}$) are given in Table A8.

A1.4.2 Carbon

The zooplankton carbon biomass increases with carbon uptake via grazing and decreases through carbon losses through mortality, respiration and carbon excretion to the semi-labile DOC pool. Macrozooplankton further gains carbon by grazing on small zooplankton and loses it via fecal pellet production.

$$\text{SMS}(\text{ZooC}) = \underbrace{\gamma_{\text{zoo}} \cdot (G_{\text{small}}^{zoo} \cdot q_{\text{small}}^{\text{C}\,:\,\text{N}} + G_{\text{dia}}^{zoo} \cdot q_{\text{dia}}^{\text{C}\,:\,\text{N}})}_{\text{Grazing on phytoplankton}} + \underbrace{\gamma_{\text{zoo}} \cdot (G_{\text{det}}^{zoo} \cdot q_{\text{det}}^{\text{C}\,:\,\text{N}} + G_{\text{detZ2}}^{zoo} \cdot q_{\text{detZ2}}^{\text{C}\,:\,\text{N}})}_{\text{Grazing on detritus}} - \underbrace{G_{\text{zoo}} \cdot q_{\text{zoo}}^{\text{C}\,:\,\text{N}}}_{\text{Grazing loss by macrozoo}} \tag{A23}$$

$$- \underbrace{m_{\text{zoo}} \cdot \text{ZooN}^2 \cdot q_{\text{zoo}}^{\text{C}\,:\,\text{N}}}_{\text{Zooplankton mortality}} - \underbrace{r_{\text{zoo}} \cdot \text{ZooC}}_{\text{Respiration loss}} - \underbrace{\epsilon_{\text{zoo}}^{\text{C}} \cdot \text{ZooC}}_{\text{Excretion of DOC}} \tag{A24}$$

$$\text{SMS}(\text{Zoo2C}) = \underbrace{\gamma_{zoo2} \cdot (G_{\text{small}}^{zoo2} \cdot q_{\text{small}}^{\text{C}\,:\,\text{N}} + G_{\text{dia}}^{zoo2} \cdot q_{\text{dia}}^{\text{C}\,:\,\text{N}})}_{\text{Grazing on phytoplankton}} + \underbrace{\gamma_{zoo2} \cdot (G_{\text{det}}^{zoo2} \cdot q_{\text{det}}^{\text{C}\,:\,\text{N}} + G_{\text{detZ2}}^{zoo2} \cdot q_{\text{detZ2}}^{\text{C}\,:\,\text{N}})}_{\text{Grazing on detritus}} + \underbrace{\gamma_{zoo2} \cdot (G_{\text{zoo}} \cdot q_{\text{zoo}}^{\text{C}\,:\,\text{N}})}_{\text{Grazing on small zoo}} \tag{A25}$$

$$- \underbrace{m_{\text{zoo2}} \cdot \text{Zoo2N}^2 \cdot q_{\text{zoo2}}^{\text{C}\,:\,\text{N}}}_{\text{Zooplankton mortality}} - \underbrace{r_{\text{zoo2}} \cdot \text{Zoo2C}}_{\text{Respiration loss}} - \underbrace{\epsilon_{\text{zoo2}}^{\text{C}} \cdot \text{Zoo2C}}_{\text{Excretion of DOC}} - \underbrace{f_{\text{c}} \cdot G_{\text{cflux}}}_{\text{Fecal pellet}} \tag{A26}$$

The state variables ZooN, ZooC, Zoo2N and Zoo2C are listed in Table A1. A fraction of the grazed phytoplankton (γ_{zoo} and γ_{zoo2}, Table A3) is kept in the zooplankton biomass while the remainder is returned back to detritus pool as a consequence of sloppy feeding. Grazing terms (G_{small}^{zoo}, G_{dia}^{zoo}, G_{det}^{zoo}, G_{detZ2}^{zoo}, G_{small}^{zoo2}, G_{dia}^{zoo2}, G_{det}^{zoo2}, G_{detZ2}^{zoo2} and G_{zoo}) are calculated in Section A4.2. The respiration terms of zooplankton (r_{zoo} and r_{zoo2}) are calculated in Eqs. A60 and A61. Mortality parameters (m_{zoo}, m_{zoo2}) are listed in Table A3. The DOC excretion terms ($\epsilon_{\text{zoo}}^{\text{C}}$, $\epsilon_{\text{zoo2}}^{\text{C}}$) are in Table A8. The grazing flux in terms of

nitrogen biomass is converted to carbon biomass using the respective intracellular C:N ratios ($q_{\text{small}}^{\text{C:N}}$, $q_{\text{dia}}^{\text{C:N}}$, $q_{\text{det}}^{\text{C:N}}$, $q_{\text{detZ2}}^{\text{C:N}}$, $q_{\text{zoo}}^{\text{C:N}}$ and $q_{\text{zoo2}}^{\text{C:N}}$) where, $q_{\text{small}}^{\text{C:N}} = \text{PhyC}_{\text{small}}/\text{PhyN}_{\text{small}}$, $q_{\text{dia}}^{\text{C:N}} = \text{PhyC}_{\text{dia}}/\text{PhyN}_{\text{dia}}$, $q_{\text{det}}^{\text{C:N}} = \text{DetC}/\text{DetN}$, $q_{\text{detZ2}}^{\text{C:N}} = \text{DetZ2C}/\text{DetZ2N}$,

750   $q_{\text{zoo}}^{\text{C:N}} = \text{ZooC}/\text{ZooN}$ and $q_{\text{zoo2}}^{\text{C:N}} = \text{Zoo2C}/\text{Zoo2N}$. Total grazed carbon biomass (G_{cflux}) and the fecal pellet production rate constant (f_c, Table A3) together determine the fraction of carbon being lost to the large detritus carbon pool via fecal pellets.

A1.5   Detritus

A1.5.1   Nitrogen

Detrital nitrogen pool increases as a result of sloppy feeding and mortality. Sloppy feeding is outlined as a function of grazing

755   fluxes and grazing efficiency of macrozooplankton. In other words, the grazed phytoplankton partly goes to the macrozooplankton biomass depending on the grazing efficiency. The phytoplankton aggregation contributes only to slow-sinking detritus. Fecal pellet production is defined only for macrozooplankton group. Detritus is degraded to DON based on temperature and a remineralisation rate.

$$\text{SMS}(\text{DetN}) = \underbrace{(G_{\text{small}}^{\text{zoo}} + G_{\text{dia}}^{\text{zoo}}) \cdot (1 - \gamma_{\text{zoo}})}_{\text{Sloppy feeding}} + \underbrace{m_{\text{zoo}} \cdot \text{ZooN}^2}_{\text{Zooplankton mortality}} - \underbrace{\gamma_{\text{zoo}} \cdot (G_{\text{det}}^{\text{zoo}} + G_{\text{detZ2}}^{\text{zoo}})}_{\text{Grazing loss, small zoo}}$$

760
$$+ \underbrace{\text{Agg} \cdot (\text{PhyN}_{\text{small}} + \text{PhyN}_{\text{dia}})}_{\text{Phytoplankton aggregation}} - \underbrace{\rho_{\text{DetN}} \cdot f_T \cdot \text{DetN}}_{\text{Degradation to DON}} \tag{A27}$$

$$\text{SMS}(\text{DetZ2N}) = \underbrace{(G_{\text{small}}^{\text{zoo2}} + G_{\text{dia}}^{\text{zoo2}} + G_{\text{zoo}}) \cdot (1 - \gamma_{\text{zoo2}})}_{\text{Sloppy feeding}} - \underbrace{\gamma_{\text{zoo2}} \cdot (G_{\text{det}}^{\text{zoo2}} + G_{\text{detZ2}}^{\text{zoo2}} \cdot)}_{\text{Grazing loss, macrozoo}} \tag{A28}$$

$$+ \underbrace{m_{\text{zoo2}} \cdot \text{Zoo2N}^2}_{\text{Mortality}} + \underbrace{f_n \cdot G_{\text{tot}}}_{\text{Fecal pellet}} - \underbrace{\rho_{\text{DetN}} \cdot f_T \cdot \text{DetZ2N}}_{\text{Degradation to DON}} \tag{A29}$$

The state variables $\text{PhyN}_{\text{small}}$, PhyN_{dia}, ZooN, DetN, Zoo2N and DetZ2N are listed in Table A1. The grazing efficiency (γ_{zoo} and γ_{zoo2}), mortality (m_{zoo}, m_{zoo2}) and fecal pellet production rate constant (f_n) are listed in Table A3. Grazing terms ($G_{\text{small}}^{\text{zoo}}$,

765   $G_{\text{dia}}^{\text{zoo}}$, $G_{\text{det}}^{\text{zoo}}$, $G_{\text{detZ2}}^{\text{zoo}}$, $G_{\text{small}}^{\text{zoo2}}$, $G_{\text{dia}}^{\text{zoo2}}$, $G_{\text{det}}^{\text{zoo2}}$, $G_{\text{detZ2}}^{\text{zoo2}}$ and G_{zoo}) are calculated in Section A4.2. The remineralisation rate constant of DON (ρ_{DetN}) is listed in Table A8. The temperature dependency f_T is calculated in Eq. A43. The aggregation (Agg) term is calculated in Eq. A52.

A1.5.2   Carbon

Detrital carbon sources are associated with sloppy feeding, aggregation of phytoplankton, mortality of small zooplankton and

770   fecal pellet production by macrozooplankton. Degradation of DetC and DetZ2C to DOC is the only loss term.

$$\mathrm{SMS(DetC)} = \underbrace{(G_{\mathrm{small}}^{\mathrm{zoo}} \cdot q_{\mathrm{small}}^{\mathrm{C:N}} + G_{\mathrm{dia}}^{\mathrm{zoo}} \cdot q_{\mathrm{dia}}^{\mathrm{C:N}}) \cdot (1 - \gamma_{\mathrm{zoo}})}_{\text{Sloppy feeding}} + \underbrace{m_{\mathrm{zoo}} \cdot \mathrm{ZooN}^2 \cdot q_{\mathrm{zoo}}^{\mathrm{C:N}}}_{\text{small zoo mortality}} - \underbrace{\gamma_{zoo} \cdot (G_{\mathrm{det}}^{\mathrm{zoo}} \cdot q_{\mathrm{det}}^{\mathrm{C:N}} + G_{\mathrm{detZ2}}^{\mathrm{zoo}} \cdot q_{\mathrm{detZ2}}^{\mathrm{C:N}})}_{\text{Grazing loss by macro zoo}}$$
(A30)

$$+ \underbrace{\mathrm{Agg} \cdot (\mathrm{PhyC_{small}} + \mathrm{PhyC_{dia}})}_{\text{Phytoplankton aggregation}} - \underbrace{\rho_{\mathrm{DetC}} \cdot f_T \cdot \mathrm{DetC}}_{\text{Degradation to DOC}}$$

$$\mathrm{SMS(DetZ2C)} = \underbrace{(G_{\mathrm{small}}^{\mathrm{zoo2}} \cdot q_{\mathrm{small}}^{\mathrm{C:N}} + G_{\mathrm{dia}}^{\mathrm{zoo2}} \cdot q_{\mathrm{dia}}^{\mathrm{C:N}} + G_{\mathrm{zoo}} \cdot q_{\mathrm{zoo}}^{\mathrm{C:N}}) \cdot (1 - \gamma_{zoo2})}_{\text{Sloppy feeding}} - \underbrace{\gamma_{zoo2} \cdot (G_{\mathrm{det}}^{\mathrm{zoo2}} \cdot q_{\mathrm{det}}^{\mathrm{C:N}} + G_{\mathrm{detZ2}}^{\mathrm{zoo2}} \cdot q_{\mathrm{detZ2}}^{\mathrm{C:N}})}_{\text{Grazing loss by macro zoo}}$$
(A31)

$$+ \underbrace{m_{\mathrm{zoo2}} \cdot \mathrm{Zoo2N}^2 \cdot q_{\mathrm{zoo2}}^{\mathrm{C:N}}}_{\text{Mortality}} + \underbrace{f_{\mathrm{c}} \cdot G_{\mathrm{cflux}}}_{\text{Fecal pellet}} - \underbrace{\rho_{\mathrm{DetC}} \cdot f_T \cdot \mathrm{DetZ2C}}_{\text{Degradation to DOC}}$$
(A32)

775 The state variables $\mathrm{PhyC_{small}}$, $\mathrm{PhyC_{dia}}$, ZooN, DetC, Zoo2N and DetZ2C are listed in Table A1. The grazing efficiency (γ_{zoo} and γ_{zoo2}) and mortality (m_{zoo} m_{zoo2}) parameters are listed in Table A3. Grazing terms ($G_{\mathrm{small}}^{\mathrm{zoo}}$, $G_{\mathrm{dia}}^{\mathrm{zoo}}$, $G_{\mathrm{det}}^{\mathrm{zoo}}$, $G_{\mathrm{detZ2}}^{\mathrm{zoo}}$, $G_{\mathrm{small}}^{\mathrm{zoo2}}$, $G_{\mathrm{dia}}^{\mathrm{zoo2}}$, $G_{\mathrm{det}}^{\mathrm{zoo2}}$, $G_{\mathrm{detZ2}}^{\mathrm{zoo2}}$ and G_{zoo}) are calculated in Section A4.2. The remineralisation rate of DOC (ρ_{DetC}) is listed in Table A8. Temperature dependency f_T is calculated in Eq. A43. The aggregation (Agg) term is calculated in Eq. A52. Total grazed carbon biomass (G_{cflux}) and the fecal pellet production rate constant (f_{c}, Table A3) together determine the fraction of carbon

780 being lost to the large detritus carbon pool via fecal pellets. The quotas $q_{\mathrm{small}}^{\mathrm{C:N}} = \mathrm{PhyC_{small}}/\mathrm{PhyN_{small}}$, $q_{\mathrm{dia}}^{\mathrm{C:N}} = \mathrm{PhyC_{dia}}/\mathrm{PhyN_{dia}}$, $q_{\mathrm{zoo}}^{\mathrm{C:N}} = \mathrm{ZooC}/\mathrm{ZooN}$, $q_{\mathrm{zoo2}}^{\mathrm{C:N}} = \mathrm{Zoo2C}/\mathrm{Zoo2N}$, $q_{\mathrm{det}}^{\mathrm{C:N}} = \mathrm{DetC}/\mathrm{DetN}$ and $q_{\mathrm{detZ2}}^{\mathrm{C:N}} = \mathrm{DetZ2C}/\mathrm{DetZ2N}$ are used to convert the units from mmol N to mmol C.

A1.5.3 Silica

Biogenic detrital silica increases with excretion fluxes from diatoms to detritus, aggregation and grazing and decreases with
785 silica dissolution from DetSi and DetZ2Si.

$$\mathrm{SMS(DetSi)} = (\underbrace{\epsilon_{\mathrm{phy}}^{\mathrm{N}} \cdot f_{\mathrm{lim,dia}}^{\mathrm{N:Cmax}}}_{\text{Diatom excretion}} + \underbrace{\mathrm{Agg}}_{\text{Aggregation}}) \cdot \mathrm{DiaSi} + \underbrace{G_{\mathrm{dia}}^{\mathrm{zoo}} \cdot q^{\mathrm{Si:N}}}_{\text{Sloppy feeding}} - \underbrace{\rho_{\mathrm{Si}}^{T} \cdot \mathrm{DetSi}}_{\text{Remineralization to DSi}}$$
(A33)

$$\mathrm{SMS(DetZ2Si)} = \underbrace{G_{\mathrm{dia}}^{\mathrm{zoo2}} \cdot q^{\mathrm{Si:N}}}_{\text{Sloppy feeding}} - \underbrace{\rho_{\mathrm{Si}}^{T} \cdot \mathrm{DetZ2Si}}_{\text{Remineralization to DSi}}$$
(A34)

The state variables DiaSi, DetSi and DetZ2Si are listed in Table A1. The constant excretion rate ($\epsilon_{\mathrm{phy}}^{\mathrm{N}}$, Table A8) is down-regulated by the limiter factor $f_{\mathrm{lim,dia}}^{\mathrm{N:Cmax}}$ (Eq. A55) when the N:C ratio becomes too high. The remineralization rates (ρ_{Si}^{T}),
790 the aggregation (Agg) and the grazing on diatoms ($G_{\mathrm{dia}}^{\mathrm{zoo}}$, $G_{\mathrm{dia}}^{\mathrm{zoo2}}$) are calculated in Eqs. A45, A52 and A65, respectively. The intracellular ratio between diatom silicon and carbon is defined as $q^{\mathrm{Si:N}} = \mathrm{PhySi_{dia}}/\mathrm{PhyN_{dia}}$.

A1.5.4 $\mathrm{CaCO_3}$

The coccolithophore fraction of small phytoplankton loses biogenic $\mathrm{CaCO_3}$ to the detrital $\mathrm{CaCO_3}$ pool along with excretion, aggregation, respiration and grazing. Dissolution of $\mathrm{CaCO_3}$ leads to an increase in DIC and alkalinity.

$$
\text{SMS(DetCalc)} = \underbrace{\epsilon_{\text{C}}^{\text{phy}} \cdot f_{\text{lim, small}}^{\text{N:Cmax}} \cdot \text{PhyCalc}}_{\text{Small phytoplankton, excretion}} + (\underbrace{\text{Agg}}_{\text{Aggregation}} + \underbrace{r_{\text{small}}}_{\text{Respiration}}) \cdot \text{PhyCalc} + \underbrace{G_{\text{small}}^{\text{zoo}} \cdot q_{\text{small}}^{\text{CaCO}_3:\text{N}}}_{\text{Grazing loss}} \tag{A35}
$$

$$
- \underbrace{G_{\text{small}}^{\text{zoo}} \cdot q_{\text{small}}^{\text{CaCO}_3:\text{N}} \cdot \text{Diss}_{\text{calc-guts}}}_{CaCO_3 \text{ dissolution in guts}} - \underbrace{\text{Diss}_{\text{calc}} \cdot \text{DetCalc}}_{CaCO_3 \text{ dissolution, slow-sinking detritus}}
$$

$$
\text{SMS(DetZ2Calc)} = \underbrace{G_{\text{small}}^{\text{zoo2}} \cdot q_{\text{small}}^{\text{CaCO}_3:\text{N}}}_{\text{Grazing loss}} \tag{A36}
$$

$$
- \underbrace{G_{\text{small}}^{\text{zoo2}} \cdot q_{\text{small}}^{\text{CaCO}_3:\text{N}} \cdot \text{Diss}_{\text{calc-guts}}}_{CaCO_3 \text{ dissolution in guts}} - \underbrace{\text{Diss}_{\text{calc2}} \cdot \text{DetZ2Calc}}_{CaCO_3 \text{ dissolution, fast-sinking detritus}} \tag{A37}
$$

The state variables PhyCalc, DetCalc and DetZ2Calc are listed in Table A1. The constant excretion rate ($\epsilon_{\text{phy}}^{\text{C}}$, Table A8) is downregulated by the limiter factor $f_{\text{lim, small}}^{\text{N:Cmax}}$ (Eq. A55) when the N:C ratio becomes too high. The respiration (r_{small}), the aggregation (Agg) and the grazing on small pyhtoplankton ($G_{\text{small}}^{\text{zoo}}$ and $G_{\text{small}}^{\text{zoo2}}$) are calculated in Eqs. A48, A52 and A64, respectively. The ratio $q_{\text{small}}^{\text{CaCO}_3:\text{N}} = \text{PhyCalc}/\text{PhyN}_{\text{small}}$.

Calcite dissolution: As the detritus calcite sinks through the water column it is subject to dissolution. We follow Yamanaka and Tajika (1996) assuming an exponential decrease of the CaCO_3 flux with depth. As we also assume an increasing sinking speed of small detritus with depth, following Kriest and Oschlies (2008), the dissolution rate is scaled with the sinking velocity.

$$
\text{Diss}_{\text{calc}} = \text{Diss}_{\text{calc\_rate}} \cdot w_{\text{det}} \qquad \text{Diss}_{\text{calc2}} = \text{Diss}_{\text{calc\_rate}} \tag{A38}
$$

$\text{Diss}_{\text{calc}}$ and $\text{Diss}_{\text{calc2}}$ are the dissolution rate constants for slow- and fast-sinking detritus classes (Table A5). The reference dissolution rate ($\text{Diss}_{\text{calc\_rate}}$, Table A8) is based on a length scale of $3500\,\text{m}$ and velocity of $20\,\text{m}\,\text{d}^{-1}$. The sinking speed at depth z (w_{det}, Table A5) is calculated as follows:

$$
w_{\text{det}} = 0.0288 \cdot z + w_0 \tag{A39}
$$

Here, z denotes the depth and w_0 is the sinking speed at the ocean surface (Table A3). The dissolution rate for fast-sinking detritus class ($\text{Diss}_{\text{calc2}}$) is assumed to be constant throughout the water column and is set to the value of $\text{Diss}_{\text{calc\_rate}}$ (Table A8).

A1.6 Dissolved oxygen (Oxy)

Oxy concentration increases with carbon fixation by primary producers. It decreases with respiration of phyto- and zooplanktons, remineralization of dissolved organic carbon. In addition, sea–air flux of O_2 leads to an exchange of oxygen with the atmosphere, depending on the partial pressure difference of O_2 between ocean and atmosphere. This exchange is treated separately as a boundary condition. The partial pressure of surface ocean O_2 is computed using the mocsy-2.0 routines (Orr and

Epitalon, 2015).

$$
\begin{aligned}
\mathrm{SMS(Oxy)} = &\underbrace{(P_\mathrm{small} - r_\mathrm{small}) \cdot \mathrm{PhyC_{small}}}_{\text{Net production, small phytoplankton}} + \underbrace{(P_\mathrm{dia} - r_\mathrm{dia}) \cdot \mathrm{PhyC_{dia}}}_{\text{Net production, diatom}} \\
&- \underbrace{\rho_\mathrm{DOC} \cdot f_T \cdot \mathrm{DOC}}_{\text{Remineralization of DOC}} - \underbrace{r_\mathrm{zoo} \cdot \mathrm{ZooC}}_{\text{Respiration, small zoo}} - \underbrace{r_\mathrm{zoo2} \cdot \mathrm{Zoo2C}}_{\text{Respiration, macrozoo}}
\end{aligned}
\tag{A40}
$$

820 The state variables $\mathrm{PhyC_{small}}$, $\mathrm{PhyC_{dia}}$, DOC, ZooC and Zoo2C are listed in Table A1. Respiration rate constants of small phytoplankton (r_small), diatoms (r_dia) and zooplankton groups (r_zoo and r_zoo2) are computed in Sections A3.2 and A4.1, respectively. Photosynthesis terms (P_small and P_dia) are calculated in Eq. A46. The remineralization rate constant ρ_DOC is listed in Table A8 and the temperature dependency (f_T) is given in Eq. A43.

A1.7 Dissolved organic material

825 Dissolved organic matter in our model is a representation of the semi-labile fraction only, the refractory and labile fractions are not included.

A1.7.1 Dissolved organic nitrogen (DON)

DON is produced via nitrogen excretion by phytoplankton, zooplankton and by degradation of detrital nitrogen. DON is turned into DIN by remineralization which is the only sink term.

$$
\begin{aligned}
830 \quad \mathrm{SMS(DON)} = &\underbrace{\epsilon^\mathrm{N}_\mathrm{phy} \cdot f^\mathrm{N:Cmax}_\mathrm{lim,small} \cdot \mathrm{PhyN_{small}}}_{\text{Excretion, small phytoplankton}} + \underbrace{\epsilon^\mathrm{N}_\mathrm{dia} \cdot f^\mathrm{N:Cmax}_\mathrm{lim,dia} \cdot \mathrm{PhyN_{dia}}}_{\text{Excretion, diatom}} \\
&+ \underbrace{\epsilon^\mathrm{N}_\mathrm{zoo} \cdot \mathrm{ZooN}}_{\text{Excretion, small zoo}} + \underbrace{\epsilon^\mathrm{N}_\mathrm{zoo2} \cdot \mathrm{Zoo2N}}_{\text{Excretion, macrozoo}} + \underbrace{\rho_\mathrm{DetN} \cdot f_T \cdot \mathrm{DetN}}_{\text{Detritus degradation, slow-sinking}} + \underbrace{\rho_\mathrm{Det2ZN} \cdot f_T \cdot \mathrm{DetZ2N}}_{\text{Detritus degradation, fast sinking}} - \underbrace{\rho_\mathrm{DON} \cdot f_T \cdot \mathrm{DON}}_{\text{Remineralization}}
\end{aligned}
\tag{A41}
$$

The state variables $\mathrm{PhyN_{small}}$, $\mathrm{PhyN_{dia}}$, ZooN, DetN, Zoo2N, DetZ2N and DON are listed in Table A1. The constant excretion rate of nitrogen from phytoplankton and zooplankton classes ($\epsilon^\mathrm{N}_\mathrm{phy}$, $\epsilon^\mathrm{N}_\mathrm{dia}$, $\epsilon^\mathrm{N}_\mathrm{zoo}$ and $\epsilon^\mathrm{N}_\mathrm{zoo2}$), the degradation rate of detritus (ρ_DetN, ρ_DetZ2N) and the remineralization rate of DON (ρ_DON) are listed in Table A8. The constant excretion rate of phytoplankton

835 is downregulated by the limiter function ($f^\mathrm{N:Cmax}_\mathrm{lim,small}$, $f^\mathrm{N:Cmax}_\mathrm{lim,dia}$, Eq. A55) when the N : C ratio becomes too high. The temperature dependency f_T is calculated in Eq. A43.

A1.7.2 Dissolved organic carbon (DOC)

DOC is produced via carbon excretion by phytoplankton and zooplankton and by degradation of detrital carbon. DOC is turned into DIC by remineralization which is the only sink term.

$$
\begin{aligned}
840 \quad \mathrm{SMS(DOC)} = &\underbrace{\epsilon^\mathrm{C}_\mathrm{phy} \cdot f^\mathrm{N:Cmax}_\mathrm{lim,small} \cdot \mathrm{PhyC_{small}}}_{\text{Excretion, small phytoplankton}} + \underbrace{\epsilon^\mathrm{C}_\mathrm{dia} \cdot f^\mathrm{N:Cmax}_\mathrm{lim,dia} \cdot \mathrm{PhyC_{dia}}}_{\text{Excretion, diatom}} \\
&+ \underbrace{\epsilon^\mathrm{C}_\mathrm{zoo} \cdot \mathrm{ZooC}}_{\text{Excretion, small zoo}} + \underbrace{\epsilon^\mathrm{C}_\mathrm{zoo2} \cdot \mathrm{Zoo2C}}_{\text{Excretion, macrozoo}} + \underbrace{\rho_\mathrm{DetC} \cdot f_T \cdot \mathrm{DetC}}_{\text{Detritus degradation, slow sinking}} + \underbrace{\rho_\mathrm{Det2C} \cdot f_T \cdot \mathrm{Det2C}}_{\text{Detritus degradation, fast sinking}} - \underbrace{\rho_\mathrm{DOC} \cdot f_T \cdot \mathrm{DOC}}_{\text{Remineralization}}
\end{aligned}
\tag{A42}
$$

The state variables $\mathrm{PhyC_{small}}$, $\mathrm{PhyC_{dia}}$, ZooC, DetC, Zoo2C, Det2C and DOC are listed in Table A1. The constant excretion rate of nitrogen from phytoplankton and zooplankton classes ($\epsilon^\mathrm{C}_\mathrm{phy}$, $\epsilon^\mathrm{C}_\mathrm{dia}$, $\epsilon^\mathrm{C}_\mathrm{zoo}$ and $\epsilon^\mathrm{C}_\mathrm{zoo2}$), the degradation rate of detritus (ρ_DetC, ρ_Det2C) and the remineralization rate of DOC (ρ_DOC) are listed in Table A8. The constant excretion rate of phytoplankton
845   is downregulated by the limiter factor ($f^\mathrm{N\,:\,Cmax}_\mathrm{lim,small}$, $f^\mathrm{N\,:\,Cmax}_\mathrm{lim,dia}$, Eq. A55) when the N : C ratio becomes too high. Temperature dependency f_T is calculated in Eq. A43.

A2   Temperature dependence of rates

Arrhenius function: Most metabolic processes are faster at higher temperatures. This temperature dependence is defined relative to a reference temperature.

850   $$f_T = \exp\left(-4500 \cdot \left(\frac{1}{T} - \frac{1}{T_{ref}}\right)\right) \tag{A43}$$

T and T_ref are the local and reference temperature in K, respectively (Table A6).

Macrozooplankton grazing: Macrozooplankton grazing is temperature dependent. A dimensionless exponential temperature function (Butzin and Pörtner, 2016) is used for the parameterization of the temperature dependency (f_{Tzoo2}, Table A5). Specifically, the following parameterization provides an optimum curve with a maximum at 0.5°C as described in Karakuş
855   et al. (2021).

$$f_{Tzoo2} = \frac{\exp\left(\frac{Q_a}{T_r} - \frac{Q_a}{T}\right)}{1 + \exp\left(\frac{Q_h}{T_h} - \frac{Q_h}{T}\right)} \tag{A44}$$

T_r is the intrinsic optimum temperature for development and T_h is the temperature above which inhibitive processes dominate. Q_a and Q_h are the temperatures for the uninhibited and inhibited reaction kinetics, respectively (Table A9). T is the local temperature in K.

860   **Silicon dissolution:** The temperature dependent dissolution rate of silicon (ρ^T_Si, Table A5) is calculated following Maerz et al. (2020), but with a minimum dissolution rate.

$$\rho^T_\mathrm{Si} = \max\left(0.023 \cdot 2.6^{\frac{T-10}{10}}, \rho_\mathrm{Si}\right) \tag{A45}$$

T is the local temperature in °C. The minimum dissolution rate (ρ_Si) is listed in Table A8.

A3   Phytoplankton processes

865   Phytoplankton growth equations are based on Geider et al. (1998) with small modifications for diatom silicon uptake, following Hohn (2009).

A3.1 Photosynthesis

The rate of the carbon specific (C-specific from now on) photosynthesis for phytoplankton (P_{small}, P_{dia}) is parameterized as follows:

$$P_{\text{small}} = P_{\text{max}}^{\text{small}} \cdot \left(1.0 - \exp \left(\frac{-\alpha_{\text{small}} \cdot q^{\text{Chl:C}} \cdot \text{PAR}}{P_{\text{max}}^{\text{small}}} \right) \right), \qquad P_{\text{dia}} = P_{\text{max}}^{\text{dia}} \cdot \left(1.0 - \exp \left(\frac{-\alpha_{\text{dia}} \cdot q^{\text{Chl:C}} \cdot \text{PAR}}{P_{\text{max}}^{\text{dia}}} \right) \right) \qquad \text{(A46)}$$

The light harvesting efficiency (α_{small}, α_{dia}) per chlorophyll is listed in Table A7. PAR is the photosynthetically available radiation (Table A5). The intracellular Chl to C ratio ($q^{\text{Chl:C}}$) is defined as PhyChl/PhyC and varies as a result of photoacclimation. The apparent maximum photosynthetic rate ($P_{\text{max}}^{\text{small}}$, $P_{\text{max}}^{\text{dia}}$) is defined below.

$$P_{\text{max}}^{\text{small}} = \mu_{\text{C small}}^{\text{max}} \cdot \min \left(f_{\text{lim, small}}^{\text{Fe}}, f_{\text{lim, small}}^{\text{N:Cmin}} \right) \cdot f_T , \qquad P_{\text{max}}^{\text{dia}} = \mu_{\text{C, dia}}^{\text{max}} \cdot \min \left(f_{\text{lim, dia}}^{\text{Fe}}, f_{\text{lim, dia}}^{\text{N:Cmin}}, f_{\text{lim, dia}}^{\text{Si:Cmin}} \right) \cdot f_T \qquad \text{(A47)}$$

The value of $\mu_{\text{C small}}^{\text{max}}, \mu_{\text{C, dia}}^{\text{max}}$ is listed in Table A7. The limitation terms ($f_{\text{lim,small}}^{\text{N:Cmin}}$, $f_{\text{lim,dia}}^{\text{N:Cmin}}$, $f_{\text{lim,dia}}^{\text{Si:Cmin}}$, $f_{\text{lim,small}}^{\text{Fe}}$ and $f_{\text{lim,dia}}^{\text{Fe}}$) are presented in Section A3.6 and the temperature dependency (f_T) is calculated in Eq. A43.

A3.2 Respiration

The phytoplankton respiration rate (r_{small} and r_{dia}, Table A5) is calculated as a base respiration plus a second term proportional to N-assimilation, as a measure of biosynthesis:

$$r_{\text{small}} = \underbrace{\text{res}_{\text{small}} \cdot f_{\text{lim,small}}^{\text{N:Cmax}}}_{\text{Maintenance}} + \underbrace{\zeta \cdot \text{V}_{\text{small}}^{\text{N}}}_{\text{N-assim}}, \qquad r_{\text{dia}} = \underbrace{\text{res}_{\text{dia}} \cdot f_{\text{lim,dia}}^{\text{N:Cmax}}}_{\text{Maintenance}} + \underbrace{\zeta \cdot \text{V}_{\text{dia}}^{\text{N}}}_{\text{N-assim}} \qquad \text{(A48)}$$

The values for the maintenance respiration rate ($\text{res}_{\text{small}}$, res_{dia}) and the cost of biosynthesis (ζ) are listed in Table A7. Si-assimilation is assumed to be inexpensive, so it is not included as additional cost in the respiration (Hohn, 2009). The limiter function ($f_{\text{lim,small}}^{\text{N:Cmax}}$ and $f_{\text{lim,dia}}^{\text{N:Cmax}}$) is described in Eq. A55 and the N-assimilation rate ($\text{V}_{\text{small}}^{\text{N}}$, $\text{V}_{\text{dia}}^{\text{N}}$) is calculated in Eq. A50.

A3.3 Chlorophyll a synthesis

The chlorophyll synthesis rate ($\text{S}_{\text{small}}^{\text{chl}}$, $\text{S}_{\text{dia}}^{\text{chl}}$, Table A5) is proportional to N-assimilation, with the proportionality factor varying as a function of the C-specific photosynthesis rate, relative to the maximum possible photosynthetic rate at the current Chl:C ratio of the cell, which depends on photosynthetically available radiation and light harvesting efficiency.

$$\text{S}_{\text{small}}^{\text{chl}} = \text{V}_{\text{small}}^{\text{N}} \cdot q_{\text{max,small}}^{\text{Chl:N}} \cdot \min \left(1, \frac{P_{\text{small}}}{\alpha_{\text{small}} \cdot q^{\text{Chl:C}} \cdot \text{PAR}} \right), \qquad \text{S}_{\text{dia}}^{\text{chl}} = \text{V}_{\text{dia}}^{\text{N}} \cdot q_{\text{max,dia}}^{\text{Chl:N}} \cdot \min \left(1, \frac{P_{\text{dia}}}{\alpha_{\text{dia}} \cdot q^{\text{Chl:C}} \cdot \text{PAR}} \right) \qquad \text{(A49)}$$

The N-assimilation ($\text{V}_{\text{small}}^{\text{N}}$, $\text{V}_{\text{dia}}^{\text{N}}$) is computed in Eq. A50. The conversion factor of the maximum Chl : N ratio ($q_{\text{max,small}}^{\text{Chl:N}}, q_{\text{max,dia}}^{\text{Chl:N}}$) and the light harvesting efficiency (α_{small}, α_{dia}) are listed in Table A7. The C-specific photosynthesis (P_{small}, P_{dia}) is given in Eq. A46. PAR is the photosynthetically available radiation (Table A5) and the intracellular Chl to C ratio ($q^{\text{Chl:C}}$) is defined as PhyChl/PhyC.

A3.4 N- and Si-assimilation

Nitrogen: The C-specific N-assimilation rate is a function of the maximum rate of C-specific photosynthesis and DIN concen-
895 tration. N-assimilation depends on the DIN concentration in seawater via Michaelis–Menten kinetics. The $N:C$ uptake ratio
and a function of the intracellular quota between N and C further, which downregulates uptake under high N:C ratio further
modify the N-assimilation.

$$V_{small}^{N} = V_{cm}^{small} \cdot P_{max}^{small} \cdot \sigma_{N:C}^{small} \cdot f_{lim,small}^{N:Cmax} \cdot \frac{DIN}{K_{small}^{N} + DIN}, \qquad V_{dia}^{N} = V_{cm}^{dia} \cdot P_{max}^{dia} \cdot \sigma_{N:C}^{dia} \cdot f_{lim,dia}^{N:Cmax} \cdot \frac{DIN}{K_{dia}^{N} + DIN} \qquad (A50)$$

$V_{cm}^{small}, V_{cm}^{dia}, \sigma_{N:C}^{small}, \sigma_{N:C}^{dia}, K_{small}^{N}$ and K_{dia}^{N} are listed in Table A7. The maximum rate of photosynthesis (P_{max}^{small} and P_{max}^{dia}) is given
900 in Eqs. A47. $f_{lim,small}^{N:Cmax}$ and $f_{lim,dia}^{N:Cmax}$ are described in Eq. A55. DIN corresponds to insitu concentration.

Silicon: The building of a silica frustule of diatoms requires silicate uptake. The C-specific Si-assimilation rate is a function
of a factor for C-specific N-uptake, a rate constant of C-specific photosynthesis, maximum uptake ratio $N:C$ for small phy-
toplankton and DSi concentration. The maximum $Si:C$ ratio, temperature, and the scaling factor for the maximum nitrogen
uptake further regulate the N-assimilation.

905
$$V^{Si} = V_{cm}^{dia} \cdot \mu_{C,dia}^{max} \cdot f_T \cdot \sigma_{Si:C} \cdot f_{lim}^{Si:Cmax} \cdot f_{lim,dia}^{N:Cmax} \cdot \frac{DSi}{K_{Si} + DSi} \qquad (A51)$$

The scaling factor for the N-uptake (V_{cm}^{dia}), the maximum Rate constant of C-specific photosynthesis ($\mu_{C,dia}^{max}$), the uptake ratio
of the maximum $Si:C$ ($\sigma_{Si:C}$) and half-saturation constant for silicate uptake (K_{Si}) are listed in Table A7. The temperature
dependency (f_T) is computed in Eq. A43. The limitation by the intracellular ratios $N:C$ and $Si:C$ ($f_{lim,dia}^{N:Cmax}, f_{lim}^{Si:Cmax}$) are
described in Eqs. A55 and A56, respectively. DSi corresponds to in situ concentration.

910 A3.5 Aggregation loss

The aggregation rate (Agg, Table A5) is proportional to the concentration of small phytoplankton, diatoms and detritus. The
effect of increased stickiness of diatoms under nutrient limitation (Waite et al., 1992; Aumont et al., 2015) is taken into account
by multiplying the diatom biomass with (1-q_{lim}^{dia}). When the nutrient limitation is high (i.e, low q_{lim}^{dia}), the aggregation rate
increases in the model.

915
$$Agg = \phi_{phy} \cdot \left(PhyN_{small} + (1 - q_{lim}^{dia}) \cdot PhyN_{dia} \right) + \phi_{det} \cdot (DetN + DetZ2N) \qquad (A52)$$

$$q_{lim}^{dia} = \min \left(f_{lim,dia}^{Fe}, f_{lim,dia}^{N:Cmin}, f_{lim,dia}^{Si:Cmin} \right) \qquad (A53)$$

The state variables $PhyN_{small}$, $PhyN_{dia}$, $DetN$ and $DetZ2N$ are described in Table A1. The values of the maximum aggregation
loss parameters (ϕ_{phy} and ϕ_{det}) are listed in Table A3. The limitation terms ($f_{lim,dia}^{N:Cmin}$, $f_{lim,dia}^{Si:Cmin}$ and $f_{lim,dia}^{Fe}$) are presented below
920 (Section A3.6).

A3.6 Nutrient limitation

The metabolic processes such as C-specific photosynthesis, respiration rate and excretion losses are treated as functions of the intracellular nitrogen status (i.e., N : C ratios q) following Geider et al. (1998). Intracellular ratios between nutrients and carbon limit uptake of nitrogen and silicon which is modeled via a non-linear function as in Schourup-Kristensen et al. (2014).

925
$$f_{\text{lim}}(\theta, q_1, q_2) = 1 - \exp(-\theta(|\Delta q| - \Delta q)^2) \tag{A54}$$

Here, $\Delta q = q_1 - q_2$ is the difference between the current intracellular nutrient:C quota and a prescribed maximum or minimum quota. The dimensionless constant θ controls the limitation.

A3.6.1 $f_{\text{lim}}^{\text{N : Cmax}}$

The limiter $f_{\text{lim}}^{\text{N : Cmax}}$ downregulates the metabolic processes such as nitrogen and Si-assimilation, excretion and maintenance
930 respiration of phytoplankton when the intracellular nitrogen quota ($q^{\text{N : C}}$) becomes too high. $f_{\text{lim}}^{\text{N : Cmax}}$ is one when the current $q^{\text{N : C}} < 0.151$ (i.e., Redfield ratio, 16N:106C) and zero for $q^{\text{N : C}} > 0.2$ (i.e., 21.2N:106C). It determines the end of the uptake of nitrogen and silicon in assimilation processes as well as the cease of carbon and nitrogen release during the respiration and excretion of DON/DOC and CaCO_3 processes of phytoplankton (See Section A1.5.4).

$$f_{\text{lim,small}}^{\text{N : Cmax}} = f_{\text{lim}}(\theta_{\max}^{\text{N}}, q_{\text{small}}^{\text{N : C}}, q_{\text{small}}^{\text{N : Cmax}}), \qquad f_{\text{lim,dia}}^{\text{N : Cmax}} = f_{\text{lim}}(\theta_{\max}^{\text{N}}, q_{\text{dia}}^{\text{N : C}}, q_{\text{dia}}^{\text{N : Cmax}}) \tag{A55}$$

935 The limitation function for quota regulation is calculated with Eq. A54. $q_{\text{small}}^{\text{N : C}}$ and $q_{\text{dia}}^{\text{N : C}}$ are the current intracellular nitrogen quota for small phytoplankton and diatoms, respectively. Dimensionless constants $\theta_{\max}^{\text{N}}$, $q_{\text{small}}^{\text{N : Cmax}}$ and $q_{\text{dia}}^{\text{N : Cmax}}$ are listed in Table A6.

A3.6.2 $f_{\text{lim}}^{\text{Si : Cmax}}$

The limiter $f_{\text{lim}}^{\text{Si : Cmax}}$ downregulates the Si-assimilation of diatoms when the intracellular silicon quota (Si : C) becomes too
940 high. $f_{\text{lim}}^{\text{Si : Cmax}}$ is one when the current $q^{\text{N : C}} < 0.76$ and zero for $q^{\text{N : C}} > 0.8$. It determines the end of the uptake of silicon in assimilation processes. The limiter function is described in Eq. A54 and is calculated as follows:

$$f_{\text{lim}}^{\text{Si : Cmax}} = f_{\text{lim}}(\theta_{\max}^{\text{Si}}, q^{\text{Si : C}}, q^{\text{Si : Cmax}}) \tag{A56}$$

Dimensionless constants $\theta_{\max}^{\text{Si}}$ and $q^{\text{Si : Cmax}}$ are listed in Table A6.

A3.6.3 $f_{\text{lim}}^{\text{Si : Cmin}}$

945 Carbon fixation and aggregation loss in diatoms are further downregulated by a factor ($f_{\text{lim,dia}}^{\text{Si : Cmin}}$, see Eq. A54) when the intracellular silicon quota ($q^{\text{Si : C}}$) approaches a minimum value ($q^{\text{Si : Cmin}}$), mimicking the arrest of cellular division at low cellular Si (Claquin et al., 2002). $f_{\text{lim,dia}}^{\text{Si : Cmin}}$ is zero when the current $q^{\text{Si : C}} < 0.04$ and one for $q^{\text{Si : C}} > 0.08$.

$$f_{\text{lim,dia}}^{\text{Si : Cmin}} = f_{\text{lim}}(\theta_{\min}^{\text{Si}}, q^{\text{Si : Cmin}}, q^{\text{Si : C}}) \tag{A57}$$

Dimensionless constants $\theta_{\min}^{\text{Si}}$ and $q^{\text{Si : Cmin}}$ are listed in Table A6.

A3.6.4 $f_{\text{lim}}^{\text{Fe}}$

Growth-limitation by iron is modeled with Michaelis–Menten kinetics, implicitly assuming that all dissolved iron is ultimately bioavailable.

$$f_{\text{lim,small}}^{\text{Fe}} = \frac{\text{DFe}}{K_{\text{small}}^{\text{Fe}} + \text{DFe}}, \ , \qquad f_{\text{lim,dia}}^{\text{Fe}} = \frac{\text{DFe}}{K_{\text{dia}}^{\text{Fe}} + \text{DFe}} \tag{A58}$$

Stat variable DFe is listed in Table A1. The half saturation constants ($K_{\text{small}}^{\text{Fe}}$ and $K_{\text{dia}}^{\text{Fe}}$) are given in Table A6.

A3.6.5 $f_{\text{lim}}^{\text{N:Cmin}}$

In addition to iron limitation, photosynthesis is limited by nitrogen in small phytoplankton and diatoms using the Eq. A54. Nitrogen limitation ($f_{\text{lim,small}}^{\text{N:Cmin}}$, $f_{\text{lim,dia}}^{\text{N:Cmin}}$) is described as a function of the intracellular nitrogen quota ($q_{\text{small}}^{\text{N:C}}$, $q_{\text{dia}}^{\text{N:C}}$) with growth ending at a minimum quota ($q_{\text{small}}^{\text{N:Cmin}}$, $q_{\text{dia}}^{\text{N:Cmin}}$).

$$f_{\text{lim,small}}^{\text{N:Cmin}} = f_{\text{lim}}(\theta_{\text{min}}^{\text{N}}, q_{\text{small}}^{\text{N:Cmin}}, q_{\text{small}}^{\text{N:C}}), \qquad f_{\text{lim,dia}}^{\text{N:Cmin}} = f_{\text{lim}}(\theta_{\text{min}}^{\text{N}}, q_{\text{dia}}^{\text{N:Cmin}}, q_{\text{dia}}^{\text{N:C}}) \tag{A59}$$

Dimensionless constants $\theta_{\text{min}}^{\text{N}}$, $q_{\text{small}}^{\text{N:Cmin}}$ and $q_{\text{dia}}^{\text{N:Cmin}}$ are listed in Table A6.

A4 Zooplankton processes

A4.1 Zooplankton respiration

Small zooplankton: When the intracellular C:N ratio in zooplankton exceeds the Redfield ratio, a temperature dependent respiration (r_{zoo}, Table A5) is assumed to drive it back with a time scale τ.

$$r_{\text{zoo}} = \frac{q_{\text{zoo}}^{\text{C:N}} - q_{\text{standard}}^{\text{C:N}}}{\tau} \cdot f_T \tag{A60}$$

The time scale for respiration (τ) is listed in Table A7. The temperature dependence (f_T) is calculated in Eq. (A43). The ratios are defined as $q_{\text{zoo}}^{\text{C:N}} = \text{ZooC}/\text{ZooN}$ and $q_{\text{Standard}}^{\text{C:N}} = 106\text{C}/16\text{N}$.

Macrozooplankton: The daily respiration rate constant of macrozooplankton (r_{zoo2}, Table A5) is modeled following Karakuş et al. (2021).

$$r_{\text{zoo2}} = R_{\text{s}} \cdot (1 + R_f + R_a) \tag{A61}$$

The standard respiration rate (R_{s}) is listed in Table A3. The feeding activity factor (R_f, Table A5) is defined as the ratio of grazing flux to carbon biomass of macrozooplankton which increases linearly from 0 to 1 for ratio between 0% and 10% and is 1 otherwise. The respiration activity factor (R_a, Table A5) defines reduced macrozooplankton respiration rate in austral/boreal winter with the value of -0.5.

A4.2 Grazing

In REcoM3, there are two zooplankton classes, small zooplankton (< 2cm) and macrozooplankton (2-20 cm). The small zooplankton group grazes on small phytoplankton and diatoms as well as on fast- and slow-sinking detrital particles. While macrozooplankton grazes on similarly both phytoplankton classes and detritus groups, it further grazes on small zooplankton. Total grazing of both zooplankton groups is based on the Holling type III ingestion function as follows:

$$G_{\text{tot}}^{\text{zoo}} = \xi_{zoo} \cdot \frac{\left(\sum_i p_i \cdot N_i\right)^2}{\sigma_{zoo} + \left(\sum_i p_i \cdot N_i\right)^2} \cdot f_T \cdot \text{ZooN} \tag{A62}$$

$G_{\text{tot}}^{\text{zoo}}$ ($G_{\text{tot}}^{\text{zoo2}}$) is the total grazing flux which is calculated for small (macro) zooplankton. ZooN (Zoo2N) is listed in Table A1. The maximum grazing rate (ξ_{zoo}, ξ_{zoo2}) and the half saturation constants ($\sigma_{zoo}, \sigma_{zoo2}$) are listed in Table A10. The temperature dependency terms (f_T, f_{Tzoo2}) are given in Eqs. A43 and A44. In the model, relative grazing preferences are implemented following Fasham et al. (1990). Variable relative grazing preferences (p_i) are calculated using the nominal preferences for small phytoplankton, diatoms, slow-/fast-sinking detritus and small zooplankton (Table A10) as follows:

$$p_i = \frac{p'_i \cdot N_i}{\sum_i p'_i \cdot N_i} \tag{A63}$$

. Here, summation i is done over each food source to calculate the relative proportion of the food. Total grazing is used to calculate the grazing of zooplankton groups on individual food source, i.e., small phytoplankton (i=1, PhyN$_{\text{small}}$), diatoms (i=2, PhyN$_{\text{dia}}$), both detritus classes (i=3, DetN and i=4, DetZ2N) and (i=5, ZooN) in the case of macrozooplankton as the ratio of each food source to total food source (G$_{\text{small}}$, G$_{\text{dia}}$, G$_{\text{det}}$, G$_{\text{detZ2}}$ and G$_{\text{zoo}}$).

$$G_{\text{small}}^{\text{zoo}} = G_{\text{tot}}^{\text{zoo}} \cdot \frac{p_{\text{small}} \cdot \text{PhyN}_{\text{small}}}{\sum_i p_i \cdot N_i}, \qquad G_{\text{small}}^{\text{zoo2}} = G_{\text{tot}}^{\text{zoo2}} \cdot \frac{p_{\text{small}} \cdot \text{PhyN}_{\text{small}}}{\sum_i p_i \cdot N_i} \tag{A64}$$

$$G_{\text{dia}}^{\text{zoo}} = G_{\text{tot}}^{\text{zoo}} \cdot \frac{p_{\text{dia}} \cdot \text{PhyN}_{\text{dia}}}{\sum_i p_i \cdot N_i}, \qquad G_{\text{dia}}^{\text{zoo2}} = G_{\text{tot}}^{\text{zoo2}} \cdot \frac{p_{\text{dia}} \cdot \text{PhyN}_{\text{dia}}}{\sum_i p_i \cdot N_i} \tag{A65}$$

$$G_{\text{det}}^{\text{zoo}} = G_{\text{tot}}^{\text{zoo}} \cdot \frac{p_{\text{det}} \cdot \text{DetN}}{\sum_i p_i \cdot N_i}, \qquad G_{\text{det}}^{\text{zoo2}} = G_{\text{tot}}^{\text{zoo2}} \cdot \frac{p_{\text{det}} \cdot \text{DetN}}{\sum_i p_i \cdot N_i} \tag{A66}$$

$$G_{\text{detZ2}}^{\text{zoo}} = G_{\text{tot}}^{\text{zoo}} \cdot \frac{p_{\text{detZ2}} \cdot \text{DetZ2N}}{\sum_i p_i \cdot N_i}, \qquad G_{\text{detZ2}}^{\text{zoo2}} = G_{\text{tot}}^{\text{zoo2}} \cdot \frac{p_{\text{detZ2}} \cdot \text{DetZ2N}}{\sum_i p_i \cdot N_i} \tag{A67}$$

$$G_{\text{zoo}} = G_{\text{tot}}^{\text{zoo2}} \cdot \frac{p_{\text{ZooN}} \cdot \text{ZooN}}{\sum_i p_i \cdot N_i} \tag{A68}$$

where G_{zoo} is associated with macrozooplankton grazing on small zooplankton. PhyN$_{\text{small}}$, PhyN$_{\text{dia}}$, ZooN, DetN and DetZ2N are listed in Table A1.

A5 Bottom boundary fluxes

The model contains a benthic layer at the sea floor. Within this benthic layer, the total amounts of organic carbon, organic nitrogen, biogenic silica and CaCO3 are modeled.

Loss to benthos: When the slow- and fast-sinking detritus reach the ocean bottom, they continue to sink into the benthic layer with the speed w_{det} (Eq. A39) and $w_{\mathrm{detZ2}} = 200$ m d^{-1}, respectively. This results in a detrital flux ($\mathrm{BenF_{DetN}}$, $\mathrm{BenF_{DetZ2N}}$, $\mathrm{BenF_{DetC}}$, $\mathrm{BenF_{DetZ2C}}$, $\mathrm{BenF_{DetSi}}$, $\mathrm{BenF_{DetZ2Si}}$, $\mathrm{BenF_{DetCalc}}$ and $\mathrm{BenF_{DetZ2Calc}}$, Table A11) from the water column to the benthos.

$$\mathrm{BenF_{DetN}} = -w_{\mathrm{det}} \cdot \mathrm{DetN} \tag{A69}$$

$$\mathrm{BenF_{DetC}} = -w_{\mathrm{det}} \cdot \mathrm{DetC} \tag{A70}$$

$$\mathrm{BenF_{DetSi}} = -w_{\mathrm{det}} \cdot \mathrm{DetSi} \tag{A71}$$

$$\mathrm{BenF_{DetCalc}} = -w_{\mathrm{det}} \cdot \mathrm{DetCalc} \tag{A72}$$

$$\mathrm{BenF_{DetZ2N}} = -w_{\mathrm{detZ2}} \cdot \mathrm{DetZ2N} \tag{A73}$$

$$\mathrm{BenF_{DetZ2C}} = -w_{\mathrm{detZ2}} \cdot \mathrm{DetZ2C} \tag{A74}$$

$$\mathrm{BenF_{DetZ2Si}} = -w_{\mathrm{detZ2}} \cdot \mathrm{DetZ2Si} \tag{A75}$$

$$\mathrm{BenF_{DetZ2Calc}} = -w_{\mathrm{detZ2}} \cdot \mathrm{DetZ2Calc} \tag{A76}$$

These fluxes increase the total amount of the different benthic state variables. The state variables DetN, DetC, DetSi, $\mathrm{DetCalc}$, $\mathrm{DetZ2N}$, $\mathrm{DetZ2C}$, $\mathrm{DetZ2Si}$ and $\mathrm{DetZ2Calc}$ are described in Table A1.

Input from benthos: The lowermost ocean layer located next to the benthic layer receives remineralized inorganic matter back from the benthos. These fluxes, at the same time reduce the amount of the benthic variables. In addition, a sediment flux of Fe from the sediment is calculated from the nitrogen flux, but assuming a Fe:N ratio that is higher than in biomass. This parameterization models that the release of iron from the sediment is driven by redox processes, which are ultimately tied to their remineralization of organic matter.

$$\mathrm{BenF_{DIN}} = \rho_{\mathrm{ben}}^{\mathrm{N}} \cdot \mathrm{BenthosN} \tag{A77}$$

$$\mathrm{BenF_{DSi}} = \rho_{\mathrm{ben}}^{\mathrm{Si}} \cdot \mathrm{BenthosSi} \tag{A78}$$

$$\mathrm{BenF_{DIC}} = \rho_{\mathrm{ben}}^{\mathrm{C}} \cdot \mathrm{BenthosC} + \mathrm{Diss_{calc}} \cdot \mathrm{BenthosCalc} + \mathrm{Diss_{calc2}} \cdot \mathrm{BenthosCalc2} \tag{A79}$$

$$\mathrm{BenF_{Alk}} = (1 + 1/16) \cdot \rho_{\mathrm{ben}}^{\mathrm{N}} \cdot \mathrm{BenthosN} + 2 \cdot \mathrm{Diss_{calc}} \cdot \mathrm{BenthosCalc} \tag{A80}$$

$\mathrm{BenF_{DIN}}$, $\mathrm{BenF_{DSi}}$, $\mathrm{BenF_{DIC}}$ and $\mathrm{BenF_{Alk}}$ (Table A11) denote the fluxes of DIN, DSi, DIC and Alk returned into the bottom layer of the ocean. Constant remineralization rates ($\rho_{\mathrm{ben}}^{\mathrm{N}}$, $\rho_{\mathrm{ben}}^{\mathrm{Si}}$ and $\rho_{\mathrm{ben}}^{\mathrm{C}}$) are listed in Table A8. The calcite dissolution rates $\mathrm{Diss_{calc}}$ and $\mathrm{Diss_{calc2}}$ are calculated in Eq. (A38). BenthosN, BenthosSi, BenthosC and BenthosCalc denote the vertically integrated benthos concentration of dissolved nitrogen, silicate, carbon and calcium carbonate, respectively (Table A2). The

alkalinity of the lowermost ocean layer located next to the benthic layer is changed by the remineralization of DIN, dissoved inorganic phosphate converted from DIN with Redfield ratio) and dissolution of calcite from the benthos.

Table A1. List of oceanic state variables in REcoM3.

Variable	Description	Unit
DIN	Dissolved Inorganic Nitrogen	$[\mathrm{mmol\,N\,m^{-3}}]$
DSi	Dissolved Inorganic Silicon	$[\mathrm{mmol\,N\,m^{-3}}]$
DFe	Dissolved Inorganic Iron	$[\mathrm{\mu mol\,Fe\,m^{-3}}]$
DIC	Dissolved Inorganic Carbon	$[\mathrm{mmol\,C\,m^{-3}}]$
Alk	Alkalinity	$[\mathrm{mmol\,C\,m^{-3}}]$
$\mathrm{PhyN_{small}}$	Intracellular nitrogen concentration in small phytoplankton	$[\mathrm{mmol\,N\,m^{-3}}]$
$\mathrm{PhyC_{small}}$	Intracellular carbon concentration in small phytoplankton	$[\mathrm{mmol\,C\,m^{-3}}]$
PhyCalc	Intracellular calcite concentration in small phytoplankton	$[\mathrm{mmol\,CaCO_3\,m^{-3}}]$
$\mathrm{PhyChl_{small}}$	Intracellular chl a concentration in small phytoplankton	$[\mathrm{mg\,Chl\,m^{-3}}]$
$\mathrm{PhyN_{dia}}$	Intracellular nitrogen concentration in diatoms	$[\mathrm{mmol\,N\,m^{-3}}]$
$\mathrm{PhyC_{dia}}$	Intracellular carbon concentration in diatoms	$[\mathrm{mmol\,C\,m^{-3}}]$
$\mathrm{PhySi_{dia}}$	Intracellular silicon concentration in diatoms	$[\mathrm{mmol\,Si\,m^{-3}}]$
$\mathrm{PhyChl_{dia}}$	Intracellular chl a concentration in diatoms	$[\mathrm{mg\,Chl\,m^{-3}}]$
ZooN	small zooplankton nitrogen concentration	$[\mathrm{mmol\,N\,m^{-3}}]$
Zoo2N	Macrozooplankton nitrogen concentration	$[\mathrm{mmol\,N\,m^{-3}}]$
ZooC	small zooplankton carbon concentration	$[\mathrm{mmol\,C\,m^{-3}}]$
Zoo2C	Macrozooplankton carbon concentration	$[\mathrm{mmol\,C\,m^{-3}}]$
DetN	Slow-sinking detritus nitrogen concentration	$[\mathrm{mmol\,N\,m^{-3}}]$
DetZ2N	Fast-sinking detritus nitrogen concentration	$[\mathrm{mmol\,N\,m^{-3}}]$
DetC	Slow-sinking detritus carbon concentration	$[\mathrm{mmol\,C\,m^{-3}}]$
DetZ2C	Fast-sinking detritus carbon concentration	$[\mathrm{mmol\,C\,m^{-3}}]$
DetCalc	Slow-sinking detritus calcite concentration	$[\mathrm{mmol\,CaCO_3\,m^{-3}}]$
DetZ2Calc	Fast-sinking detritus calcite concentration	$[\mathrm{mmol\,CaCO_3\,m^{-3}}]$
DetSi	Slow-sinking detritus silicon concentration	$[\mathrm{mmol\,Si\,m^{-3}}]$
DetZ2Si	Fast-sinking detritus silicon concentration	$[\mathrm{mmol\,Si\,m^{-3}}]$
DON	Extracellular dissolved organic nitrogen	$[\mathrm{mmol\,N\,m^{-3}}]$
DOC	Extracellular dissolved organic carbon	$[\mathrm{mmol\,C\,m^{-3}}]$
Oxy	Dissolved oxygen concentration	$[\mathrm{mmol\,O\,m^{-3}}]$

Table A2. List of benthic state variables in REcoM3.

Variable	Description	Unit
BenthosN	Vertically integrated N concentration	$[\mathrm{mmol\,N\,m^{-2}}]$
BenthosC	Vertically integrated C concentration	$[\mathrm{mmol\,C\,m^{-2}}]$
BenthosSi	Vertically integrated Si concentration	$[\mathrm{mmol\,Si\,m^{-2}}]$
BenthosCalc	Vertically integrated calcite concentration	$[\mathrm{mmol\,CaCO_3\,m^{-2}}]$

Table A3. Parameters for sources-minus-sinks equations.

Parameter	Value	Description	Unit
ψ	0.02	Calcite production ratio	[dimensionless]
γ_{zoo}	0.4	Fraction of grazing flux to small zooplankton pool	[dimensionless]
γ_{zoo2}	0.8	Fraction of grazing flux to macrozooplankton pool	[dimensionless]
m_{zoo}	0.05	Small zooplankton mortality rate	$[\mathrm{m^3\,mmol\,N^{-1}\,d^{-1}}]$
m_{zoo2}	0.003	Macrozooplankton mortality rate	$[\mathrm{m^3\,mmol\,N^{-1}\,d^{-1}}]$
ϕ_{phy}	0.015	Max aggregation loss parameter for phytoplankton N	$[\mathrm{m^3\,mmol\,N^{-1}\,d^{-1}}]$
ϕ_{det}	0.165	Max aggregation loss parameter for detritus N	$[\mathrm{m^3\,mmol\,N^{-1}\,d^{-1}}]$
w_0	20.0	Detritus sinking speed at surface	$[\mathrm{m\,d^{-1}}]$
f_{n}	0.104	N fecal pellet production rate constant	$[\mathrm{m^3\,mmol\,N^{-1}\,d^{-1}}]$
f_{c}	0.236	C fecal pellet production rate constant	$[\mathrm{m^3\,mmol\,C^{-1}\,d^{-1}}]$

Table A4. Parameters for iron calculations.

Parameter	Value	Description	Unit
$q^{\mathrm{Fe:N}}$	0.033	Intracellular Fe : N ratio	$[\mathrm{\mu mol\,Fe\,mmol\,N^{-1}}]$
$K_{\mathrm{Fe_L}}$	100.0	Iron stability constant	$[\mathrm{m^{-3}\,\mu mol}]$
$\mathrm{L_T}$	1.0	Total ligand concentration	$[\mathrm{\mu mol\,m^{-3}}]$
κ_{Fe}	0.07	Scavenging rate of iron	$[\mathrm{m^3\,mmol\,C^{-1}\,d^{-1}}]$
$q^{\mathrm{Fe:N}}$	0.033	Intracellular Fe : N ratio	$[\mathrm{\mu mol\,Fe\,mmol\,N^{-1}}]$

Table A5. Model variables.

Variable	Description	Unit
Agg	Aggregation rate constant [d^{-1}]	
$\mathrm{Diss}_{\mathrm{calc}}$	The dissolution rate constant for slow-sinking detritus	[d^{-1}]
$\mathrm{Diss}_{\mathrm{calc2}}$	The dissolution rate constant for fast-sinking detritus	[d^{-1}]
$\mathrm{Diss}_{\mathrm{calc\_guts}}$	Dissolution of calcium carbonate in guts constant	[d^{-1}]
w_{det}	Sinking velocity of detritus	[$\mathrm{m\,d}^{-1}$]
f_T	Temperature dependence of rates	[dimensionless]
f_{Tzoo2}	Temperature dependence of macrozooplankton grazing rates	[dimensionless]
G_{tot}	Total zooplankton grazing rate	[$\mathrm{mmol\,N\,m}^{-3}\,\mathrm{d}^{-1}$]
G_{small}	Small phytoplankton specific zooplankton grazing rate	[$\mathrm{mmol\,N\,m}^{-3}\,\mathrm{d}^{-1}$]
G_{dia}	Diatom specific zooplankton grazing rate	[$\mathrm{mmol\,N\,m}^{-3}\,\mathrm{d}^{-1}$]
PAR	Photosynthetically Available Radiation	[$\mathrm{W\,m}^{-2}$]
$P_{\mathrm{small}}, P_{\mathrm{dia}}$	C-specific actual rate constant of photosynthesis [d^{-1}]	
P_{max}	C-specific light saturated rate constant of photosynthesis	[d^{-1}]
r_{small}	Small phytoplankton respiration rate constant	[d^{-1}]
r_{dia}	Diatoms respiration rate constant	[d^{-1}]
r_{zoo}	small zooplankton respiration rate constant	[d^{-1}]
r_{zoo2}	Macrozooplankton respiration rate constant	[d^{-1}]
R_{f}	Macrozooplankton feeding activity factor	[d^{-1}]
R_{a}	Macrozooplankton respiration activity factor	[d^{-1}]
$S_{\mathrm{small}}^{\mathrm{chl}}, S_{\mathrm{dia}}^{\mathrm{chl}}$	Rate of chlorophyll a synthesis	[$\mathrm{mg\,Chl\,mmol\,C}^{-1}\,\mathrm{d}^{-1}$]
T	Local temperature	[K]
$\mathrm{V}_{\mathrm{small}}^{\mathrm{N}}, \mathrm{V}_{\mathrm{dia}}^{\mathrm{N}}$	N-assimilation	[$\mathrm{mmol\,N\,mmol\,C}^{-1}\,\mathrm{d}^{-1}$]
ρ_{Si}^{T}	Temperature dependent remineralization rate constant of Si	[d^{-1}]
V^{Si}	Si-assimilation	[$\mathrm{mmol\,Si\,mmol\,C}^{-1}\,\mathrm{d}^{-1}$]

Table A6. Parameters for limitation functions.

Parameter	Value	Description	Unit
$K_{\text{small}}^{\text{Fe}}$	0.04	Half saturation constant for small phytoplankton Fe uptake	[µmol Fe m^{-3}]
$K_{\text{dia}}^{\text{Fe}}$	0.12	Half saturation constant for diatom Fe uptake	[µmol Fe m^{-3}]
$q_{\text{small}}^{\text{N:Cmin}}$	0.04	Minimum intracellular N : C ratio for small phytoplankton	[mmol N mmol C^{-1}]
$q_{\text{dia}}^{\text{N:Cmin}}$	0.04	Minimum intracellular N : C ratio for diatoms	[mmol N mmol C^{-1}]
$q_{\text{small}}^{\text{N:Cmax}}$	0.2	Maximum intracellular N : C ratio for small phytoplankton	[mmol N mmol C^{-1}]
$q_{\text{dia}}^{\text{N:Cmax}}$	0.2	Maximum intracellular N : C ratio for diatoms	[mmol N mmol C^{-1}]
$q^{\text{Si:Cmin}}$	0.04	Minimum intracellular Si : C ratio for diatoms	[mmol Si mmol C^{-1}]
$q^{\text{Si:Cmax}}$	0.8	Maximum intracellular Si : C ratio for diatoms	[mmol Si mmol C^{-1}]
$\theta_{\text{min}}^{\text{N}}$	50	Minimum limiter regulater for N	[mmol C mmol N^{-1}]
$\theta_{\text{max}}^{\text{N}}$	1000	Maximum limiter regulater for N	[mmol C mmol N^{-1}]
$\theta_{\text{min}}^{\text{Si}}$	1000	Minimum limiter regulater for Si	[mmol C mmol N^{-1}]
$\theta_{\text{max}}^{\text{Si}}$	1000	Maximum limiter regulater for Si	[mmol C mmol N^{-1}]
T_{ref}	288.15	Reference temperature for Arrhenius function	[K]

Table A7. Parameters for phytoplankton processes.

Parameter	Value	Description	Unit
α_{small}	0.14	Light harvesting efficiency for small phytoplankton	[mmol C m^2 (mg Chl W d)$^{-1}$]
α_{dia}	0.19	Light harvesting efficiency for diatoms	[mmol C m^2 (mg Chl W d)$^{-1}$]
$\mu_{\text{C,small}}^{\text{max}}$	3.0	Rate constant of C-specific photosynthesis	[d^{-1}]
$\mu_{\text{C,dia}}^{\text{max}}$	3.5	Rate constant of C-specific photosynthesis	[d^{-1}]
$\text{res}_{\text{small}}$	0.01	Maintenance respiration rate constant	[d^{-1}]
res_{dia}	0.01	Maintenance respiration rate constant	[d^{-1}]
ζ	2.33	Cost of biosynthesis of N	[mmol C mmol N^{-1}]
$q_{\text{max,small}}^{\text{Chl:N}}$	3.15	Maximum Chl:N ratio for phytoplankton	[mg Chl mmol N^{-1}]
$q_{\text{max,dia}}^{\text{Chl:N}}$	4.2	Maximum Chl:N ratio for phytoplankton	[mg Chl mmol N^{-1}]
$K_{\text{small}}^{\text{N}}$	0.55	Half saturation constant for small phytoplankton N uptake	[mmol N m^{-3}]
$K_{\text{dia}}^{\text{N}}$	1.00	Half saturation constant for diatom N uptake	[mmol N m^{-3}]
$V_{\text{cm}}^{\text{small}}$	0.7	scaling factor for C-specific N-uptake for small phytoplankton	[dimensionless]
$V_{\text{cm}}^{\text{dia}}$	0.7	scaling factor for C-specific N-uptake for diatoms	[dimensionless]
$\sigma_{\text{N:C}}^{\text{small}}$	0.2	Maximum uptake ratio N : C for small phytoplankton	[mmol N mmol C^{-1}]
$\sigma_{\text{N:C}}^{\text{dia}}$	0.2	Maximum uptake ratio N : C for diatoms	[mmol N mmol C^{-1}]
K_{Si}	4.00	Half saturation constant for diatom Si uptake	[mmol Si m^{-3}]
$\sigma_{\text{Si:C}}$	0.2	Maximum uptake ratio Si : C	[mmol Si mmol C^{-1}]

Table A8. Degradation parameters for sources-minus-sinks equations.

Parameter	Value	Description	Unit
$\epsilon_{\mathrm{phy}}^{\mathrm{N}}$	0.05	Small phytoplankton excretion constant of organic N	$[\mathrm{d}^{-1}]$
$\epsilon_{\mathrm{dia}}^{\mathrm{N}}$	0.05	Diatoms excretion constant of organic N	$[\mathrm{d}^{-1}]$
$\epsilon_{\mathrm{phy}}^{\mathrm{C}}$	0.1	Small phytoplankton excretion constant of organic C	$[\mathrm{d}^{-1}]$
$\epsilon_{\mathrm{dia}}^{\mathrm{C}}$	0.1	Diatoms excretion constant of organic C	$[\mathrm{d}^{-1}]$
$\epsilon_{\mathrm{zoo}}^{\mathrm{N}}$	0.15	small zooplankton excretion constant of organic N	$[\mathrm{d}^{-1}]$
$\epsilon_{\mathrm{zoo2}}^{\mathrm{N}}$	0.02	Macrozooplankton excretion constant of organic N	$[\mathrm{d}^{-1}]$
$\epsilon_{\mathrm{zoo}}^{\mathrm{C}}$	0.15	small zooplankton excretion constant of organic C	$[\mathrm{d}^{-1}]$
$\epsilon_{\mathrm{zoo2}}^{\mathrm{C}}$	0.02	Macrozooplankton excretion constant of organic C	$[\mathrm{d}^{-1}]$
$\rho_{\mathrm{ben}}^{\mathrm{N}}$	0.005	Remineralization rate constant for benthos N	$[\mathrm{d}^{-1}]$
$\rho_{\mathrm{ben}}^{\mathrm{Si}}$	0.005	Remineralization rate constant for benthos Si	$[\mathrm{d}^{-1}]$
$\rho_{\mathrm{ben}}^{\mathrm{C}}$	0.005	Remineralization rate constant for benthos C	$[\mathrm{d}^{-1}]$
ρ_{DON}	0.11	Remineralization constant of DON	$[\mathrm{d}^{-1}]$
ρ_{DOC}	0.1	Remineralization constant of DOC	$[\mathrm{d}^{-1}]$
ρ_{DetN}	0.165	Degradation constant of DetN	$[\mathrm{d}^{-1}]$
ρ_{DetZ2N}	0.165	Degradation constant of DetZ2N	$[\mathrm{d}^{-1}]$
ρ_{DetC}	0.15	Degradation constant of DetC	$[\mathrm{d}^{-1}]$
ρ_{DetZ2C}	0.15	Degradation constant of DetZ2C	$[\mathrm{d}^{-1}]$
$\mathrm{deg}_{\mathrm{small}}^{\mathrm{chl}}$	0.2	Small phytoplankton chlorophyll a degradation rate constant	$[\mathrm{d}^{-1}]$
$\mathrm{deg}_{\mathrm{dia}}^{\mathrm{chl}}$	0.2	Diatom chlorophyll a degradation rate constant	$[\mathrm{d}^{-1}]$
$\mathrm{Diss}_{\mathrm{calc\_rate}}$	0.005714	Dissolution of calcium carbonate constant	$[\mathrm{d}^{-1}]$

Table A9. Parameters for macrozooplankton grazing.

Parameter	Value	Description	Unit
Q_a	28145	Temperatures for the uninhibited reaction kinetics	$[^{\circ}\mathrm{K}]$
Q_h	105234	Temperatures for the inhibited reaction kinetics	$[^{\circ}\mathrm{K}]$
T_r	272.5	Intrinsic optimum temperature	$[^{\circ}\mathrm{K}]$
T_h	274.5	Temperature above which inhibitive processes dominate	$[^{\circ}\mathrm{K}]$

Table A10. Parameters for zooplankton processes.

Parameter	Value	Description	Unit
ξ_{zoo}	2.4	Maximum grazing rate constant, small zooplankton	$[\mathrm{d}^{-1}]$
ξ_{zoo2}	0.1	Maximum grazing rate constant, macrozooplankton	$[\mathrm{d}^{-1}]$
σ_{zoo}	0.35	Half saturation constant, small zooplankton	$[(\mathrm{mmol\,N\,m}^{-3})^2]$
σ_{zoo2}	0.0144	Half saturation constant, macrozooplankton	$[(\mathrm{mmol\,N\,m}^{-3})^2]$
τ	0.01	Time scale constant for zooplankton respiration	$[\mathrm{d}^{-1}]$
R_s	0.0107	Standard respiration rate constant	$[\mathrm{d}^{-1}]$
		small zooplankton	
p'_{small}	1.0	Initial grazing preference for small phytoplankton	[dimensionless]
p'_{dia}	0.5	Initial grazing preference for diatoms	[dimensionless]
p'_{det}	0.5	Initial grazing preference for slow-sinking detritus	[dimensionless]
p'_{detZ2}	0.5	Initial grazing preference for fast-sinking detritus	[dimensionless]
		Macrozooplankton	
p'_{small}	0.5	Initial grazing preference for small phytoplankton	[dimensionless]
p'_{dia}	1.0	Initial grazing preference for diatoms	[dimensionless]
p'_{zoo}	0.8	Initial grazing preference for zooplankton	[dimensionless]
p'_{det}	0.5	Initial grazing preference for slow-sinking detritus	[dimensionless]
p'_{detZ2}	0.5	Initial grazing preference for fast-sinking detritus	[dimensionless]

Table A11. Benthos variables.

Variable	Description	Unit
$\mathrm{BenF_{Alk}}$	Flux of alkalinity from benthos to bottom water	$[\mathrm{mmol\,m}^{-2}\,\mathrm{d}^{-1}]$
$\mathrm{BenF_{DIC}}$	Flux of C from benthos to bottom water	$[\mathrm{mmol\,C\,m}^{-2}\,\mathrm{d}^{-1}]$
$\mathrm{BenF_{DIN}}$	Flux of N from benthos to bottom water	$[\mathrm{mmol\,N\,m}^{-2}\,\mathrm{d}^{-1}]$
$\mathrm{BenF_{DSi}}$	Flux of Si from benthos to bottom water	$[\mathrm{mmol\,Si\,m}^{-2}\,\mathrm{d}^{-1}]$
$\mathrm{BenF_{DetCalc}}$	Flux of slow-sinking detritus calcite from the water to the benthos	$[\mathrm{mmol\,CaCO_3\,m}^{-2}\,\mathrm{d}^{-1}]$
$\mathrm{BenF_{DetC}}$	Flux of slow-sinking detritus C from the water to the benthos	$[\mathrm{mmol\,C\,m}^{-2}\,\mathrm{d}^{-1}]$
$\mathrm{BenF_{DetN}}$	Flux of slow-sinking detritus N from the water to the benthos	$[\mathrm{mmol\,N\,m}^{-2}\,\mathrm{d}^{-1}]$
$\mathrm{BenF_{DetSi}}$	Flux of slow-sinking detritus Si from the water to the benthos	$[\mathrm{mmol\,Si\,m}^{-2}\,\mathrm{d}^{-1}]$
$\mathrm{BenF_{DetZ2Calc}}$	Flux of fast-sinking detritus calcite from the water to the benthos	$[\mathrm{mmol\,CaCO_3\,m}^{-2}\,\mathrm{d}^{-1}]$
$\mathrm{BenF_{DetZ2C}}$	Flux of fast-sinking detritus C from the water to the benthos	$[\mathrm{mmol\,C\,m}^{-2}\,\mathrm{d}^{-1}]$
$\mathrm{BenF_{DetZ2N}}$	Flux of fast-sinking detritus N from the water to the benthos	$[\mathrm{mmol\,N\,m}^{-2}\,\mathrm{d}^{-1}]$
$\mathrm{BenF_{DetZ2Si}}$	Flux of fast-sinking detritus Si from the water to the benthos	$[\mathrm{mmol\,Si\,m}^{-2}\,\mathrm{d}^{-1}]$

References

Albani, S., Mahowald, N. M., Perry, A. T., Scanza, R. A., Zender, C. S., Heavens, N. G., Maggi, V., Kok, J. F., and Otto-Bliesner, B. L.:
1035   Improved dust representation in the Community Atmosphere Model, Journal of Advances in Modeling Earth Systems, 6, 541–570,
https://doi.org/10.1002/2013MS000279, 2014.

Álvarez, E., Thoms, S., and Völker, C.: Chlorophyll to Carbon Ratio Derived From a Global Ecosystem Model With Photodamage, Global
Biogeochemical Cycles, 32, 799–816, https://doi.org/10.1029/2017GB005850, 2018.

Anderson, L. G., Jutterström, S., Hjalmarsson, S., Wåhlström, I., and Semiletov, I. P.: Out-gassing of CO2 from Siberian Shelf seas by
1040   terrestrial organic matter decomposition, Geophysical Research Letters, 36, https://doi.org/https://doi.org/10.1029/2009GL040046, 2009.

Anderson, T. R., Gentleman, W. C., and Sinha, B.: Influence of grazing formulations on the emergent properties of
a complex ecosystem model in a global ocean general circulation model, Progress in Oceanography, 87, 201–213,
https://doi.org/https://doi.org/10.1016/j.pocean.2010.06.003, 3rd GLOBEC OSM: From ecosystem function to ecosystem prediction,
2010.

1045   Aumont, O., Orr, J. C., Monfray, P., Ludwig, W., Amiotte-Suchet, P., and Probst, J.-L.: Riverine-driven interhemispheric transport of carbon,
Global Biogeochemical Cycles, 15, 393–405, https://doi.org/https://doi.org/10.1029/1999GB001238, 2001.

Aumont, O., Maier-Reimer, E., Blain, S., and Monfray, P.: An ecosystem model of the global ocean including Fe, Si, P colimitations, Global
Biogeochemical Cycles, 17, https://doi.org/https://doi.org/10.1029/2001GB001745, 2003.

Aumont, O., Ethé, C., Tagliabue, A., Bopp, L., and Gehlen, M.: PISCES-v2: an ocean biogeochemical model for carbon and ecosystem
1050   studies, Geoscientific Model Development, 8, 2465–2513, https://doi.org/10.5194/gmd-8-2465-2015, 2015.

Bakker, D., De Baar, H., and Bathmann, U.: Changes of carbon dioxide in surface waters during spring in the Southern Ocean, Deep Sea
Research Part II: Topical Studies in Oceanography, 44, 91–127, https://doi.org/https://doi.org/10.1016/S0967-0645(96)00075-6, 1997.

Bakker, D. C. E., Pfeil, B., Landa, C. S., Metzl, N., O'Brien, K. M., Olsen, A., Smith, K., Cosca, C., Harasawa, S., Jones, S. D., Nakaoka, S.,
Nojiri, Y., Schuster, U., Steinhoff, T., Sweeney, C., Takahashi, T., Tilbrook, B., Wada, C., Wanninkhof, R., Alin, S. R., Balestrini, C. F.,
1055   Barbero, L., Bates, N. R., Bianchi, A. A., Bonou, F., Boutin, J., Bozec, Y., Burger, E. F., Cai, W.-J., Castle, R. D., Chen, L., Chierici, M.,
Currie, K., Evans, W., Featherstone, C., Feely, R. A., Fransson, A., Goyet, C., Greenwood, N., Gregor, L., Hankin, S., Hardman-Mountford,
N. J., Harlay, J., Hauck, J., Hoppema, M., Humphreys, M. P., Hunt, C. W., Huss, B., Ibánhez, J. S. P., Johannessen, T., Keeling, R., Kitidis,
V., Körtzinger, A., Kozyr, A., Krasakopoulou, E., Kuwata, A., Landschützer, P., Lauvset, S. K., Lefèvre, N., Lo Monaco, C., Manke, A.,
Mathis, J. T., Merlivat, L., Millero, F. J., Monteiro, P. M. S., Munro, D. R., Murata, A., Newberger, T., Omar, A. M., Ono, T., Paterson,
1060   K., Pearce, D., Pierrot, D., Robbins, L. L., Saito, S., Salisbury, J., Schlitzer, R., Schneider, B., Schweitzer, R., Sieger, R., Skjelvan, I.,
Sullivan, K. F., Sutherland, S. C., Sutton, A. J., Tadokoro, K., Telszewski, M., Tuma, M., van Heuven, S. M. A. C., Vandemark, D., Ward,
B., Watson, A. J., and Xu, S.: A multi-decade record of high-quality fCO$_2$ data in version 3 of the Surface Ocean CO$_2$ Atlas (SOCAT),
Earth System Science Data, 8, 383–413, https://doi.org/10.5194/essd-8-383-2016, 2016.

Ballantyne, A. P., Alden, C. B., Miller, J. B., Tans, P. P., and White, J. W. C.: Increase in observed net carbon dioxide uptake by land and
1065   oceans during the past 50 years, Nature, 488, 70–72, https://doi.org/10.1038/nature11299, 2012.

Behrenfeld, M. J. and Falkowski, P. G.: A consumer's guide to phytoplankton primary productivity models, Limnology and Oceanography,
42, 1479–1491, https://doi.org/10.1038/s41586-019-1098-2, 1997.

Blondeau-Patissier, D., Gower, J. F., Dekker, A. G., Phinn, S. R., and Brando, V. E.: A review of ocean color remote sensing methods and statistical techniques for the detection, mapping and analysis of phytoplankton blooms in coastal and open oceans, Progress in Oceanography, 123, 123–144, https://doi.org/https://doi.org/10.1016/j.pocean.2013.12.008, 2014.

Bopp, L., Resplandy, L., Orr, J. C., Doney, S. C., Dunne, J. P., Gehlen, M., Halloran, P., Heinze, C., Ilyina, T., Séférian, R., Tjiputra, J., and Vichi, M.: Multiple stressors of ocean ecosystems in the 21st century: projections with CMIP5 models, Biogeosciences, 10, 6225–6245, https://doi.org/10.5194/bg-10-6225-2013, 2013.

Boyd, P., Claustre, H., Levy, M., Siegel, D. A., and Weber, T.: Multi-faceted particle pumps drive carbon sequestration in the ocean, Nature, 568, 327–335, https://doi.org/10.1038/s41586-019-1098-2, 2019.

Boye, M., van den Berg, C. M., de Jong, J. T., Leach, H., Croot, P., and de Baar, H. J.: Organic complexation of iron in the Southern Ocean, Deep Sea Research Part I: Oceanographic Research Papers, 48, 1477–1497, https://doi.org/https://doi.org/10.1016/S0967-0637(00)00099-6, 2001.

Buitenhuis, E., Rivkin, R. B., Séailley, S., and Le Quéré, C.: Biogeochemical fluxes through microzooplankton, Global Biogeochemical Cycles, 24, https://doi.org/10.1029/2009GB003601, 2010.

Bunsen, F.: Impact of recent climate variability on oceanic CO2 uptake in a global ocean biogeochemistry model, Master's thesis, Kiel University Christian-Albrechts-Universität, Faculty of Mathematics and Natural Sciences, 2022.

Bushinsky, S. M., Landschützer, P., Rödenbeck, C., Gray, A. R., Baker, D., Mazloff, M. R., Resplandy, L., Johnson, K. S., and Sarmiento, J. L.: Reassessing Southern Ocean air-sea CO2 flux estimates with the addition of biogeochemical float observations., Global Biogeochemical Cycles, 33, 1370–1388, https://doi.org/10.1029/2019GB006176, 2019.

Butzin, M. and Pörtner, H. O.: Thermal growth potential of Atlantic cod by the end of the 21st century, Global Change Biology, 22, 4162–4168, https://doi.org/10.1111/gcb.13375, 2016.

Campin, J.-M., Adcroft, A. J., Hill, C., and Marshall, J.: Conservation of properties in a free-surface model, Ocean Modelling, 6, 221–244, https://doi.org/10.1016/S1463-5003(03)00009-X, 2004.

Canadell, J., Monteiro, P., Costa, M., Cotrim da Cunha, L., Cox, P., Eliseev, A., Henson, S., Ishii, M., Jaccard, S., Koven, C., Lohila, A., Patra, P., Piao, S., Rogelj, J., Syampungani, S., Zaehle, S., and Zickfeld, K.: Global Carbon and other Biogeochemical Cycles and Feedbacks, p. 673–816, Cambridge University Press, Cambridge, United Kingdom and New York, NY, USA, https://doi.org/10.1017/9781009157896.007, 2021.

Carr, M.-E., Friedrichs, M. A., Schmeltz, M., Noguchi Aita, M., Antoine, D., Arrigo, K. R., Asanuma, I., Aumont, O., Barber, R., Behrenfeld, M., Bidigare, R., Buitenhuis, E. T., Campbell, J., Ciotti, A., Dierssen, H., Dowell, M., Dunne, J., Esaias, W., Gentili, B., Gregg, W., Groom, S., Hoepffner, N., Ishizaka, J., Kameda, T., Le Quéré, C., Lohrenz, S., Marra, J., Mélin, F., Moore, K., Morel, A., Reddy, T. E., Ryan, J., Scardi, M., Smyth, T., Turpie, K., Tilstone, G., Waters, K., and Yamanaka, Y.: A comparison of global estimates of marine primary production from ocean color, Deep Sea Research Part II: Topical Studies in Oceanography, 53, 741–770, https://doi.org/https://doi.org/10.1016/j.dsr2.2006.01.028, the US JGOFS Synthesis and Modeling Project: Phase III, 2006.

Chau, T. T. T., Gehlen, M., and Chevallier, F.: A seamless ensemble-based reconstruction of surface ocean pCO$_2$ and air–sea CO$_2$ fluxes over the global coastal and open oceans, Biogeosciences, 19, 1087–1109, https://doi.org/10.5194/bg-19-1087-2022, 2022.

Ciais, P., Sabine, C., Bala, G., Bopp, L., Brovkin, V., Canadell, J., Chhabra, A., DeFries, R., Galloway, J., Heimann, M., Le Quéré, C., Myneni, R., Piao, S., and Thornton, P.: Carbon and other biogeochemical cycles, in: Climate change 2013: the physical science basis. Contribution of Working Group I to the Fifth Assessment Report of the Intergovernmental Panel on Climate Change, pp. 465–570, Cambridge University Press, 2014.

Claquin, P., Martin-Jézéquel, V., Kromkamp, J. C., Veldhuis, M. J. W., and Kraay, G. W.: Uncoupling of Silicon Compared With Carbon and Nitrogen Metabolisms and the Role of the Cell Cycle in Continuous Cultures of Thalassiosira Pseudonana (Bacillariophyceae) Under Light, Nitrogen, and Phosphorus Control, Journal of Phycology, 38, 922–930, https://doi.org/10.1046/j.1529-8817.2002.t01-1-01220.x, 2002.

1110 Cocco, V., Joos, F., Steinacher, M., Frölicher, T. L., Bopp, L., Dunne, J., Gehlen, M., Heinze, C., Orr, J., Oschlies, A., Schneider, B., Segschneider, J., and Tjiputra, J.: Oxygen and indicators of stress for marine life in multi-model global warming projections, Biogeosciences, 10, 1849–1868, https://doi.org/10.5194/bg-10-1849-2013, 2013.

Cram, J. A., Weber, T., Leung, S. W., McDonnell, A. M. P., Liang, J.-H., and Deutsch, C.: The Role of Particle Size, Ballast, Temperature, and Oxygen in the Sinking Flux to the Deep Sea, Global Biogeochemical Cycles, 32, 858–876,
1115 https://doi.org/https://doi.org/10.1029/2017GB005710, 2018.

Danilov, S.: Ocean modeling on unstructured meshes, Ocean Modelling, 69, 195–210, https://doi.org/https://doi.org/10.1016/j.ocemod.2013.05.005, 2013.

Danilov, S., Wang, Q., Timmermann, R., Iakovlev, N., Sidorenko, D., Kimmritz, M., Jung, T., and Schröter, J.: Finite-Element Sea Ice Model (FESIM), version 2, Geosci. Model Dev., 8, 1747–1761, https://doi.org/10.5194/gmd-8-1747-2015, 2015.

1120 Danilov, S., Sidorenko, D., Wang, Q., and Jung, T.: The Finite-volumE Sea ice–Ocean Model (FESOM2), Geoscientific Model Development, 10, 765–789, https://doi.org/10.5194/gmd-10-765-2017, 2017.

de Baar, H. J., de Jong, J. T., Nolting, R. F., Timmermans, K. R., van Leeuwe, M. A., Bathmann, U., Rutgers van der Loeff, M., and Sildam, J.: Low dissolved Fe and the absence of diatom blooms in remote Pacific waters of the Southern Ocean, Marine Chemistry, 66, 1–34, https://doi.org/https://doi.org/10.1016/S0304-4203(99)00022-5, 1999.

1125 Denman, K. L., Brasseur, G., Chidthaisong, A., Ciais, P., Cox, P. M., Dickinson, R. E., Hauglustaine, D., Heinze, C., Holland, E., Jacob, D., Lohmann, U., Ramachandran, S., Leite da Silva Dias, P., Wofsy, S. C., and Zhang, X.: Couplings Between Changes in the Climate System and Biogeochemistry, in: Climate Change 2007: The Physical Science Basis. Contribution of Working Group I to the Fourth Assessment Report of the Intergovernmental Panel on Climate Change, edited by Solomon, S., Qin, D., Manning, M., Marquis, M., Averyt, K., Tignor, M. M. B., Miller, H. L., and Chen, Z. L., p. 499–587, Cambridge University Press, Cambridge, UK and New York, USA, 2007.

1130 DeVries, T., Le Quéré, C., Andrews, O., Berthet, S., Hauck, J., Ilyina, T., Landschützer, P., Lenton, A., Lima, I. D., Nowicki, M., Schwinger, J., and Séférian, R.: Decadal trends in the ocean carbon sink, Procedings of the National Academy of Sciences of the United States of America, 116, 11 646–11 651, https://doi.org/10.1073/pnas.1900371116, 2019.

Doney, S. C., Lindsay, K., Moore, J. K., Dutkiewicz, S., Friedrichs, M. A. M., and Matear, R. J.: Marine Biogeochemical Modeling: Recent Advances and Future Challenges, Oceanography, 14, 93–107, https://doi.org/10.5670/oceanog.2001.10, 2001.

1135 Du, J., Ye, Y., Zhang, X., Völker, C., and Tian, J.: Southern Control of Interhemispheric Synergy on Glacial Marine Carbon Sequestration, Geophysical Research Letters, 49, e2022GL099 048, https://doi.org/https://doi.org/10.1029/2022GL099048, e2022GL099048 2022GL099048, 2022.

Dunne, J. P., Sarmiento, J. L., and Gnanadesikan, A.: A synthesis of global particle export from the surface ocean and cycling through the ocean interior and on the seafloor, Global Biogeochem. Cycles, 21, GB4006, https://doi.org/10.1029/2006GB002907, 2007.

1140 Elrod, V. A., Berelson, W. M., Coale, K. H., and Johnson, K. S.: The flux of iron from continental shelf sediments: a missing source for global budgets, Geophysical Research Letters, 31, L12 307, https://doi.org/doi:10.1029/2004GL020216, 2004.

Fasham, M. J., Ducklow, H. W., and McKelvie, S. M.: A nitrogen-based model of plankton dynamics in the oceanic mixed layer, Journal of Marine Research, 48, 591–639, https://doi.org/https://doi.org/10.1357/002224090784984678, 1990.

Fay, A. R. and McKinley, G. A.: Observed Regional Fluxes to Constrain Modeled Estimates of the Ocean Carbon Sink, Geophysical Research Letters, 48, https://doi.org/10.1029/2021GL095325, 2021.

Fay, A. R., Gregor, L., Landschützer, P., McKinley, G. A., Gruber, N., Gehlen, M., Iida, Y., Laruelle, G. G., Rödenbeck, C., Roobaert, A., and Zeng, J.: SeaFlux: harmonization of air–sea CO_2 fluxes from surface pCO_2 data products using a standardized approach, Earth System Science Data, 13, 4693–4710, https://doi.org/10.5194/essd-13-4693-2021, 2021.

Fennel, K., Mattern, J. P., Doney, S. C., Bopp, L., Moore, A. M., Wang, B., and Yu, L.: Ocean biogeochemical modelling, Nature Reviews Methods Primers, 2, 76, https://doi.org/10.1038/s43586-022-00154-2, 2022.

Friedlingstein, P., Dufresne, J.-L., Cox, P. M., and Rayner, P. J.: How positive is the feedback between climate change and the carbon cycle?, Tellus B, 55, 692–700, https://doi.org/10.1034/j.1600-0889.2003.01461.x, 2003.

Friedlingstein, P., Jones, M. W., O'Sullivan, M., Andrew, R. M., Bakker, D. C. E., Hauck, J., Le Quéré, C., Peters, G. P., Peters, W., Pongratz, J., Sitch, S., Canadell, J. G., Ciais, P., Jackson, R. B., Alin, S. R., Anthoni, P., Bates, N. R., Becker, M., Bellouin, N., Bopp, L., Chau, T. T. T., Chevallier, F., Chini, L. P., Cronin, M., Currie, K. I., Decharme, B., Djeutchouang, L. M., Dou, X., Evans, W., Feely, R. A., Feng, L., Gasser, T., Gilfillan, D., Gkritzalis, T., Grassi, G., Gregor, L., Gruber, N., Gürses, Ö., Harris, I., Houghton, R. A., Hurtt, G. C., Iida, Y., Ilyina, T., Luijkx, I. T., Jain, A., Jones, S. D., Kato, E., Kennedy, D., Klein Goldewijk, K., Knauer, J., Korsbakken, J. I., Körtzinger, A., Landschützer, P., Lauvset, S. K., Lefèvre, N., Lienert, S., Liu, J., Marland, G., McGuire, P. C., Melton, J. R., Munro, D. R., Nabel, J. E. M. S., Nakaoka, S.-I., Niwa, Y., Ono, T., Pierrot, D., Poulter, B., Rehder, G., Resplandy, L., Robertson, E., Rödenbeck, C., Rosan, T. M., Schwinger, J., Schwingshackl, C., Séférian, R., Sutton, A. J., Sweeney, C., Tanhua, T., Tans, P. P., Tian, H., Tilbrook, B., Tubiello, F., van der Werf, G. R., Vuichard, N., Wada, C., Wanninkhof, R., Watson, A. J., Willis, D., Wiltshire, A. J., Yuan, W., Yue, C., Yue, X., Zaehle, S., and Zeng, J.: Global Carbon Budget 2021, Earth System Science Data, 14, 1917–2005, https://doi.org/10.5194/essd-14-1917-2022, 2022a.

Friedlingstein, P., O'Sullivan, M., Jones, M. W., Andrew, R. M., Gregor, L., Hauck, J., Le Quéré, C., Luijkx, I. T., Olsen, A., Peters, G. P., Peters, W., Pongratz, J., Schwingshackl, C., Sitch, S., Canadell, J. G., Ciais, P., Jackson, R. B., Alin, S. R., Alkama, R., Arneth, A., Arora, V. K., Bates, N. R., Becker, M., Bellouin, N., Bittig, H. C., Bopp, L., Chevallier, F., Chini, L. P., Cronin, M., Evans, W., Falk, S., Feely, R. A., Gasser, T., Gehlen, M., Gkritzalis, T., Gloege, L., Grassi, G., Gruber, N., Gürses, O., Harris, I., Hefner, M., Houghton, R. A., Hurtt, G. C., Iida, Y., Ilyina, T., Jain, A. K., Jersild, A., Kadono, K., Kato, E., Kennedy, D., Klein Goldewijk, K., Knauer, J., Korsbakken, J. I., Landschützer, P., Lefèvre, N., Lindsay, K., Liu, J., Liu, Z., Marland, G., Mayot, N., McGrath, M. J., Metzl, N., Monacci, N. M., Munro, D. R., Nakaoka, S.-I., Niwa, Y., O'Brien, K., Ono, T., Palmer, P. I., Pan, N., Pierrot, D., Pocock, K., Poulter, B., Resplandy, L., Robertson, E., Rödenbeck, C., Rodriguez, C., Rosan, T. M., Schwinger, J., Séférian, R., Shutler, J. D., Skjelvan, I., Steinhoff, T., Sun, Q., Sutton, A. J., Sweeney, C., Takao, S., Tanhua, T., Tans, P. P., Tian, X., Tian, H., Tilbrook, B., Tsujino, H., Tubiello, F., van der Werf, G. R., Walker, A. P., Wanninkhof, R., Whitehead, C., Willstrand Wranne, A., Wright, R., Yuan, W., Yue, C., Yue, X., Zaehle, S., Zeng, J., and Zheng, B.: Global Carbon Budget 2022, Earth System Science Data, 14, 4811–4900, https://doi.org/10.5194/essd-14-4811-2022, 2022b.

Frölicher, T. L., Rodgers, K. B., Stock, C. A., and Cheung, W. W. L.: Sources of uncertainties in 21st century projections of potential ocean ecosystem stressors: UNCERTAINTIES IN STRESSOR PROJECTIONS, Global Biogeochemical Cycles, 30, 1224–1243, https://doi.org/10.1002/2015GB005338, 2016.

Galbraith, E. D. and Skinner, L. C.: The Biological Pump During the Last Glacial Maximum, Annual Review of Marine Science, 12, 559–586, https://doi.org/10.1146/annurev-marine-010419-010906, pMID: 31899673, 2020.

1180   Garcia, H. E., Locarnini, R. A., Boyer, T. P., Antonov, J. I., Baranova, O. K., Zweng, M. M., Reagan, J. R., and Johnson, D. R.: World Ocean Atlas 2013, Volume 4: Dissolved Inorganic Nutrients (phosphate, nitrate, silicate). S. Levitus, Ed., A. Mishonov Technical Ed., Tech. rep., NOAA Atlas NESDIS 76, 2014.

Garcia, H. E., Weathers, K. W., Paver, C. R., Smolyar, I., Boyer, T. P., Locarnini, R. A., Zweng, M. M., Mishonov, A. V., Baranova, O. K., Seidov, D., and Reagan, J. R.: World Ocean Atlas 2018, Volume 3: Dissolved Oxygen, Apparent Oxygen Utilization, and Oxygen

1185   Saturation. A. Mishonov Technical Editor, Tech. rep., NOAA Atlas NESDIS 83, 2019a.

Garcia, H. E., Weathers, K. W., Paver, C. R., Smolyar, I., Boyer, T. P., Locarnini, R. A., Zweng, M. M., Mishonov, A. V., Baranova, O. K., Seidov, D., and Reagan, J. R.: World Ocean Atlas 2018, Volume 4: Dissolved Inorganic Nutrients (phosphate, nitrate, silicate). A. Mishonov Technical Editor, Tech. rep., NOAA Atlas NESDIS 84, 2019b.

Geider, R. J. and La Roche, J.: The role of iron in phytoplankton photosynthesis, and the potential for iron-limitation of primary productivity

1190   in the sea, Photosynthesis Research, 39, 275–301, https://doi.org/10.1007/BF00014588, 1994.

Geider, R. J., MacIntyre, H. L., and Kana, T. M.: A dynamic regulatory model of phytoplanktonic acclimation to light, nu- trients, and temperature, Limnol. Oceanogr., 43, 679–694, https://doi.org/doi:10.4319/lo.1998.43.4.0679, 1998.

Gent, P. and McWilliams, J.: Isopycnal Mixing in Ocean Circulation Models, J. Phys. Oceanogr., 20, 150–155, 1990.

Gray, A., Johnson, K. S., Bushinsky, S. M., Riser, S. C., Russell, J. L., Talley, L. D., Wanninkhof, R., Williams, N. L., and Sarmiento,

1195   J. L.: Autonomous biogeochemical floats detect significant carbon dioxide outgassing in the high-latitude Southern Ocean., Geophysical Research Letters,, 45, 9049–9057, https://doi.org/10.1029/2018GL078013, 2018.

Gregor, L., Lebehot, A. D., Kok, S., and Scheel Monteiro, P. M.: A comparative assessment of the uncertainties of global surface ocean CO_2 estimates using a machine-learning ensemble (CSIR-ML6 version 2019a) – have we hit the wall?, Geoscientific Model Development, 12, 5113–5136, https://doi.org/10.5194/gmd-12-5113-2019, 2019.

1200   Griffies, S.: The Gent-McWilliams Skew Flux, J. Phys. Oceanogr., 28, 831–841, https://doi.org/10.1175/1520-0485(1998)028<0831:TGMSF>2.0.CO;2, 1998.

Gruber, N., Gloor, M., Mikaloff Fletcher, S. E., Doney, S. C., Dutkiewicz, S., Follows, M. J., Gerber, M., Jacobson, A. R., Joos, F., Lindsay, K., Menemenlis, D., Mouchet, A., Müller, S. A., Sarmiento, J. L., and Takahashi, T.: Oceanic sources, sinks, and transport of atmospheric CO2, Global Biogeochemical Cycles, 23, GB1005, https://doi.org/10.1029/2008GB003349, 2009.

1205   Gruber, N., Clement, D., Carter, B. R., Feely, R. A., van Heuven, S., Hoppema, M., Ishii, M., Key, R. M., Kozyr, A., Lauvset, S. K., Monaco, C. L., Mathis, J. T., Murata, A., Olsen, A., Perez, F. F., Sabine, C. L., Tanhua, T., and Wanninkhof, R.: The oceanic sink for anthropogenic CO_2 from 1994 to 2007, Science, 363, 1193–1199, https://doi.org/10.1126/science.aau5153, 2019.

Hauck, J., Völker, C., Wang, T., Hoppema, M., Losch, M., and Wolf Gladrow, D. A.: Seasonally different carbon flux changes in the Southern Ocean in response to the southern annular mode, Global Biogeochemical Cycles, 27, 1236–1245, https://doi.org/0.1002/2013GB004600,

1210   2013.

Hauck, J., Völker, C., Wolf-Gladrow, D. A., Laufkötter, C., Vogt, M., Aumont, O., Bopp, L., Buitenhuis, E. T., Doney, S. C., Dunne, J., Gruber, N., Hashioka, T., John, J., Quéré, C. L., Lima, I. D., Nakano, H., Séférian, R., and Totterdell, I.: On the Southern Ocean CO_2 uptake and the role of the biological carbon pump in the 21st century, Global Biogeochemical Cycles, 29, 1451–1470, https://doi.org/10.1002/2015GB005140, 2015.

1215   Hauck, J., Köhler, P., Wolf-Gladrow, D., and Völker, C.: Iron fertilisation and century-scale effects of open ocean dissolution of olivine in a simulated CO2 removal experiment, Environmental Research Letters, 11, 024 007, https://doi.org/10.1088/1748-9326/11/2/024007, 2016.

Hauck, J., Zeising, M., Le Quéré, C., Gruber, N., Bakker, D. C. E., Bopp, L., Chau, T. T. T., Gürses, Ö., Ilyina, T., Landschützer, P., Lenton, A., Resplandy, L., Rödenbeck, C., Schwinger, J., and Séférian, R.: Consistency and Challenges in the Ocean Carbon Sink Estimate for the Global Carbon Budget, Frontiers in Marine Science, 7, https://doi.org/10.3389/fmars.2020.571720, 2020.

1220 Hauck, J., Lenton, A., Langlais, C., and Matear, R.: The Fate of Carbon and Nutrients Exported Out of the Southern Ocean, Global Biogeo-chemical Cycles, 32, 1556–1573, https://doi.org/10.1029/2018GB005977, 2018.

Henson, S. A., Sanders, R., Madsen, E., Morris, P. J., Le Moigne, F., and Quartly, G. D.: A reduced estimate of the strength of the ocean's biological carbon pump, Geophys. Res. Lett., 38, L04 606, https://doi.org/10.1029/2011GL046735, 2011.

Henson, S. A., Laufkötter, C., Leung, S., Giering, S. L. C., Palevsky, H. I., and Cavan, E. L.: Uncertain response of ocean biological carbon
1225 export in a changing world, Nature Geoscience, 15, 248–254, https://doi.org/10.1038/s41561-022-00927-0, 2022.

Ho, D. T., Law, C. S., Smith, M. J., Schlosser, P., Harvey, M., and Hill, P.: Measurements of air-sea gas exchange at high wind speeds in the Southern Ocean: Implications for global parameterizations, Geophysical Research Letters, 33, L16 611, https://doi.org/10.1029/2006GL026817, 2006.

Hohn, S.: Coupling and decoupling of biogeochemical cycles in marine ecosystems, Ph.D. thesis, Universität Bremen, Fachbereich Biologie,
1230 2009.

Huang, Y., Tagliabue, A., and Cassar, N.: Data-Driven Modeling of Dissolved Iron in the Global Ocean, Frontiers in Marine Science, 9, 1–14, https://doi.org/10.3389/fmars.2022.837183, 2022.

Johnson, R., Strutton, P. G., Wright, S. W., McMinn, A., and Meiners, K. M.: Three improved Satellite Chlorophyll algorithms for the Southern Ocean, Journal of Geophysical Research: Oceans, 118, 3694 – 3703, https://doi.org/doi:10.1002/jgrc.20270, 2013.

1235 Joos, F. and Spahni, R.: Rates of change in natural and anthropogenic radiative forcing over the past 20,000 years, Proceedings of the National Academy of Sciences, 105, 1425–1430, https://doi.org/10.1073/pnas.0707386105, 2008.

Juricke, S., Danilov, S., Koldunov, N., Oliver, M., and Sidorenko, D.: Ocean Kinetic Energy Backscatter Parametrization on Unstructured Grids: Impact on Global Eddy-Permitting Simulations, Journal of Advances in Modeling Earth Systems, 12, https://doi.org/10.1029/2019MS001855, 2020.

1240 Karakuş, O., Völker, C., Iversen, M., Hagen, W., Wolf-Gladrow, D., Fach, B., and Hauck, J.: Modeling the Impact of Macrozooplankton on Carbon Export Production in the Southern Ocean, Journal of Geophysical Research: Oceans, 126, https://doi.org/10.1029/2021JC017315, 2021.

Karakuş, O., Völker, C., Iversen, M., Hagen, W., and Hauck, J.: The Role of Zooplankton Grazing and Nutrient Recycling for Global Ocean Biogeochemistry and Phytoplankton Phenology, Journal of Geophysical Research: Biogeosciences, 127, e2022JG006 798,
1245 https://doi.org/https://doi.org/10.1029/2022JG006798, e2022JG006798 2022JG006798, 2022.

Keerthi, M. G., Prend, C. J., Aumont, O., and Lévy, M.: Annual variations in phytoplankton biomass driven by small-scale physical processes, Nature Geoscience, https://doi.org/10.1038/s41561-022-01057-3, 2022.

Keppler, L., Landschützer, P., Gruber, N., Lauvset, S. K., and Stemmler, I.: Seasonal Carbon Dynamics in the Near-Global Ocean, Global Biogeochemical Cycles, 34, e2020GB006 571, https://doi.org/https://doi.org/10.1029/2020GB006571, e2020GB006571
1250 10.1029/2020GB006571, 2020.

Koeve, W., Duteil, O., Oschlies, A., Kähler, P., and Segschneider, J.: Methods to evaluate CaCO$_3$ cycle modules in coupled global biogeo-chemical ocean models, Geoscientific Model Development, 7, 2393–2408, https://doi.org/10.5194/gmd-7-2393-2014, 2014.

Koldunov, N. V., Aizinger, V., Rakowsky, N., Scholz, P., Sidorenko, D., Danilov, S., and Jung, T.: Scalability and some optimization of the Finite-volumE Sea ice–Ocean Model, Version 2.0 (FESOM2), Geoscientific Model Development, 12, 3991–4012, https://doi.org/10.5194/gmd-12-3991-2019, 2019.

Kriest, I. and Oschlies, A.: On the treatment of particulate organic matter sinking in large-scale models of marine biogeochemical cycles, Biogeosciences, 5, 55–72, https://doi.org/10.5194/bg-5-55-2008, 2008.

Kulk, G., Platt, T., Dingle, J., Jackson, T., Jönsson, B. F., Bouman, H. A., Babin, M., Brewin, R. J. W., Doblin, M., Estrada, M., Figueiras, F. G., Furuya, K., González-Benítez, N., Gudfinnsson, H. G., Gudmundsson, K., Huang, B., Isada, T., Kovac, Z., Lutz, V. A., Marañón, E., Raman, M., Richardson, K., Rozema, P. D., Poll, W. H. v. d., Segura, V., Tilstone, G. H., Uitz, J., Dongen-Vogels, V. v., Yoshikawa, T., and Sathyendranath, S.: Primary Production, an Index of Climate Change in the Ocean: Satellite-Based Estimates over Two Decades, Remote Sensing, 12, https://doi.org/10.3390/rs12050826, 2020.

Kwiatkowski, L., Torres, O., Bopp, L., Aumont, O., Chamberlain, M., Christian, J. R., Dunne, J. P., Gehlen, M., Ilyina, T., John, J. G., Lenton, A., Li, H., Lovenduski, N. S., Orr, J. C., Palmieri, J., Santana-Falcón, Y., Schwinger, J., Séférian, R., Stock, C. A., Tagliabue, A., Takano, Y., Tjiputra, J., Toyama, K., Tsujino, H., Watanabe, M., Yamamoto, A., Yool, A., and Ziehn, T.: Twenty-first century ocean warming, acidification, deoxygenation, and upper-ocean nutrient and primary production decline from CMIP6 model projections, Biogeosciences, 17, 3439–3470, https://doi.org/10.5194/bg-17-3439-2020, 2020.

Kwon, E. Y., Primeau, F., and Sarmiento, J. L.: The impact of remineralization depth on the air–sea carbon balance, Nature Geoscience, 2, 630–635, https://doi.org/110.1038/ngeo612, 2009.

Köhler, P., Abrams, J. F., Völker, C., Hauck, J., and Wolf-Gladrow, D. A.: Geoengineering impact of open ocean dissolution of olivine on atmospheric CO2, surface ocean pH and marine biology, Environmental Research Letters, 8, 014 009, https://doi.org/10.1088/1748-9326/8/1/014009, 2013.

Lacroix, F., Ilyina, T., and Hartmann, J.: Oceanic CO_2 outgassing and biological production hotspots induced by pre-industrial river loads of nutrients and carbon in a global modeling approach, Biogeosciences, 17, 55–88, https://doi.org/10.5194/bg-17-55-2020, 2020.

Large, W. G. and Yeager, S. G.: The global climatology of an interannually varying air-sea flux data set., Clim Dyn, 33, 341–364, https://doi.org/10.1007/s00382-008-0441-3, 2009.

Large, W. G., McWilliams, J. C., and Doney, S. C.: Oceanic vertical mixing: A review and a model with a nonlocal boundary layer parameterization, Reviews of Geophysics, 32, https://doi.org/10.1029/94RG01872, 1994.

Lauderdale, J. M. and Cael, B. B.: Impact of remineralization profile shape on the air-sea carbon balance, Geophysical Research Letters, 48, e2020GL091 746., https://doi.org/https://doi. org/10.1029/2020GL091746, 2021.

Laufkötter, C., Vogt, M., Gruber, N., Aita-Noguchi, M., Aumont, O., Bopp, L., Buitenhuis, E., Doney, S. C., Dunne, J., Hashioka, T., Hauck, J., Hirata, T., John, J., Le Quéré, C., Lima, I. D., Nakano, H., Seferian, R., Totterdell, I., Vichi, M., and Völker, C.: Drivers and uncertainties of future global marine primary production in marine ecosystem models, Biogeosciences, 12, 6955–6984, https://doi.org/10.5194/bg-12-6955-2015, 2015.

Lauvset, S. K., Key, R. M., Olsen, A., van Heuven, S., Velo, A., Lin, X., Schirnick, C., Kozyr, A., Tanhua, T., Hoppema, M., Jutterström, S., Steinfeldt, R., Jeansson, E., Ishii, M., Perez, F. F., Suzuki, T., and Watelet, S.: A new global interior ocean mapped climatology: the $1° \times 1°$ GLODAP version 2, Earth System Science Data, 8, 325–340, https://doi.org/10.5194/essd-8-325-2016, 2016.

Le Quéré, C., Takahashi, T., Buitenhuis, E. T., Rödenbeck, C., and Sutherland, S. C.: Impact of climate change and variability on the global oceanic sink of CO_2, Global Biogeochemical Cycles, 24, 1–10, https://doi.org/10.1029/2009GB003599, 2010.

1290   Lee, Z. and Marra, J. F.: The Use of VGPM to Estimate Oceanic Primary Production: A "Tango"Difficult to Dance, Journal of Remote Sensing, 2022, 9851 013, https://doi.org/10.34133/2022/9851013, 2022.

Lenton, A., Tilbrook, B., Law, R. M., Bakker, D., Doney, S. C., Gruber, N., Ishii, M., Hoppema, M., Lovenduski, N. S., Matear, R. J., McNeil, B. I., Metzl, N., Mikaloff Fletcher, S. E., Monteiro, P. M. S., Rödenbeck, C., Sweeney, C., and Takahashi, T.: Sea–air CO_2 fluxes in the Southern Ocean for the period 1990-2009, Biogeosciences, 10, 4037–4054, https://doi.org/10.5194/bg-10-4037-2013, 2013.

1295   Lewis, K. M. and Arrigo, K. R.: Ocean Color Algorithms for Estimating Chlorophyll a, CDOM Absorption, and Particle Backscattering in the Arctic Ocean, Journal of Geophysical Research: Oceans, 125, e2019JC015 706, https://doi.org/https://doi.org/10.1029/2019JC015706, e2019JC015706 2019JC015706, 2020.

Lewis, K. M., van Dijken, G. L., and Arrigo, K. R.: Changes in phytoplankton concentration now drive increased Arctic Ocean primary production, Science, 369, 198–202, https://doi.org/10.1126/science.aay8380, 2020.

1300   Long, M. C., Moore, J. K., Lindsay, K., Levy, M., Luo, J. Y., Krumhardt, K. M., Letscher, R. T., and Sylvester, Z. T.: Simulations with the Marine Biogeochemistry Library (MARBL), Journal of Advances in Modeling Earth Systems, 13, e2021MS002 647, https://doi.org/10.1029/2021MS002647, 2021a.

Long, M. C., Stephens, B. B., McKain, K., Sweeney, C., Keeling, R. F., Kort, E. A., Morgan, E. J., Bent, J. D., Chandra, N., Chevallier, F., Commane, R., Daube, B. C., Krummel, P. B., Loh, Z., Luijkx, I. T., Munro, D., Patra, P., Peters, W., Ramonet, M., Rödenbeck, C.,
1305   Stavert, A., Tans, P., and Wofsy, S. C.: Strong Southern Ocean carbon uptake evident in airborne observations, Science, 374, 1275–1280, https://doi.org/10.1126/science.abi4355, 2021b.

Losch, M., Strass, V., B. Cisewski, C. K., and Bellerby, R. G.: Ocean state estimation from hydrography and velocity observations during EIFEX with a re- gional biogeochemical ocean circulation model, J. Mar. Sys., 129, 437–451, https://doi.org/10.1016/j.jmarsys.2013.09.003, 2014.

1310   Lévy, M., Franks, P. J. S., and Smith, K. S.: The role of submesoscale currents in structuring marine ecosystems, Nature Communications, 9, 47–58, https://doi.org/10.1038/s41467-018-07059-3, 2018.

Maerz, J., Six, K. D., Stemmler, I., Ahmerkamp, S., and Ilyina, T.: Microstructure and composition of marine aggregates as co-determinants for vertical particulate organic carbon transfer in the global ocean, Biogeosciences, 17, 1765–1803, https://doi.org/10.5194/bg-17-1765-2020, 2020.

1315   Mahowald, N., Luo, C., del Corral, J., and Zender, C. S.: Interannual variability in atmospheric mineral aerosols from a 22-year model simulation and observational data, Journal of Geophysical Research: Atmospheres, 108, https://doi.org/https://doi.org/10.1029/2002JD002821, 2003.

Maier-Reimer, E., Mikolajewicz, U., and Winguth, A.: Future ocean uptake of CO2: interaction between ocean circulation and biology, Climate Dynamics, 12, 711–722, https://doi.org/10.1007/s003820050138, 1996.

1320   Maritorena, S., Siegel, D. A., and Peterson, A. R.: Optimization of a semianalytical ocean color model for global-scale applications, Appl. Opt., 41, 2705–2714, https://doi.org/10.1364/AO.41.002705, 2002.

Marshall, J., Adcroft, A., Hill, C., Perelman, L., and Heisey, C.: A finite-volume, incompressible Navier Stokes model for studies of the ocean on parallel computers, Journal of Geophysical Research, 102, 5753–5766, 1997.

Matsuoka, A., Bricaud, A., Benner, R., Para, J., Sempéré, R., Prieur, L., Bélanger, S., and Babin, M.: Tracing the transport of colored
1325   dissolved organic matter in water masses of the Southern Beaufort Sea: relationship with hydrographic characteristics, Biogeosciences, 9, 925–940, https://doi.org/10.5194/bg-9-925-2012, 2012.

McWilliams, J. C.: Submesoscale currents in the ocean, Proceedings of the Royal Society A: Mathematical, Physical and Engineering Sciences, 472, 20160 117, https://doi.org/10.1098/rspa.2016.0117, 2016.

Metzl, N., Brunet, C., Jabaud-Jan, A., Poisson, A., and Schauer, B.: Summer and winter air–sea CO2 fluxes in the Southern Ocean, Deep
1330   Sea Research Part I: Oceanographic Research Papers, 53, 1548–1563, https://doi.org/https://doi.org/10.1016/j.dsr.2006.07.006, 2006.

Misumi, K., Tsumune, D., Yoshida, Y., Uchimoto, K., Nakamura, T., Nishioka, J., Mitsudera, H., Bryan, F. O., Lindsay, K., Moore, J. K., and Doney, S. C.: Mechanisms controlling dissolved iron distribution in the North Pacific: A model study, Journal of Geophysical Research, 116, 1–17, https://doi.org/10.1029/2010JG001541, 2011.

Mitchell, B.: Predictive bio-optical relationships for polar oceans and marginal ice zones, Journal of Marine Systems, 3, 91–105,
1335   https://doi.org/https://doi.org/10.1016/0924-7963(92)90032-4, 1992.

Mongwe, N. P., Vichi, M., and Monteiro, P. M. S.: The seasonal cycle of pCO$_2$ and CO$_2$ fluxes in the Southern Ocean: diagnosing anomalies in CMIP5 Earth system models, Biogeosciences, 15, 2851–2872, https://doi.org/10.5194/bg-15-2851-2018, 2018.

Moore, C. M., Mills, M. M., Arrigo, K. R., Berman-Frank, I., Bopp, L., Boyd, P. W., Galbraith, E. D., Geider, R. J., Guieu, C., Jaccard, S. L., Jickells, T. D., La Roche, J., Lenton, T. M., Mahowald, N. M., Marañón, E., Marinov, I., Moore, J. K., Nakatsuka, T., Oschlies, A., Saito,
1340   M. A., Thingstad, T. F., Tsuda, A., and Ulloa, O.: Processes and patterns of oceanic nutrient limitation, Nature Geoscience, 6, 701–710, https://doi.org/10.1038/ngeo1765, 2013.

Moriarty, R. and O'Brien, T. D.: Distribution of mesozooplankton biomass in the global ocean, Earth System Science Data, 5, 45–55, https://doi.org/10.5194/essd-5-45-2013, 2013.

Moriarty, R., Buitenhuis, E. T., and Le Quéré, C.: Distribution of known macrozooplankton abundance and biomass in the global ocean,
1345   Earth System Science Data, 5, 241–257, https://doi.org/10.5194/essd-5-241-2013, 2013.

Munhoven, G.: Mathematics of the total alkalinity–pH equation - pathway to robust and universal solution algorithms: the SolveSAPHE package v1.0.1, Geoscientific Model Development, 6, 1367–1388, https://doi.org/10.5194/gmd-6-1367-2013, 2013.

Mustapha, S. B., Bélanger, S., and Larouche, P.: Evaluation of ocean color algorithms in the southeastern Beaufort Sea, Canadian Arctic: New parameterization using SeaWiFS, MODIS, and MERIS spectral bands, Canadian Journal of Remote Sensing, 38, 535–556,
1350   https://doi.org/10.5589/m12-045, 2012.

Nevison, C. D., Keeling, R. F., Kahru, M., Manizza, M., Mitchell, B. G., and Cassar, N.: Estimating net community production in the Southern Ocean based on atmospheric potential oxygen and satellite ocean color data, Global Biogeochem. Cycles, 26, GB1020, https://doi.org/10.1029/2011GB004040, 2012.

Nielsdóttir, M. C., Moore, C. M., Sanders, R., Hinz, D. J., and Achterberg, E. P.: Iron limitation of the postbloom phytoplankton communities
1355   in the Iceland Basin, Global Biogeochemical Cycles, 23, 1–13, https://doi.org/10.1029/2008GB003410, 2009.

Nissen, C., Timmermann, R., Hoppema, M., Gürses, Ö., and Hauck, J.: Abruptly attenuated carbon sequestration with Weddell Sea dense waters by 2100, Nature Communications, 13, 3402, https://doi.org/10.1038/s41467-022-30671-3, 2022.

Orr, J. C.: On ocean carbon-cycle model comparison, Tellus B: Chemical and Physical Meteorology, 51, 509–510, https://doi.org/10.3402/tellusb.v51i2.16334, 1999.

1360 Orr, J. C. and Epitalon, J.-M.: Improved routines to model the ocean carbonate system: mocsy 2.0, Geoscientific Model Development, 8, 485–499, https://doi.org/10.5194/gmd-8-485-2015, 2015.

Oziel, L., Schourup-Kristensen, V., Wekerle, C., and Hauck, J.: The pan-Arctic continental slope as an intensifying conveyer belt for nutrients in the central Arctic Ocean (1985–2015), Global Biogeochemical Cycles, p. e2021GB007268, https://doi.org/10.1029/2021GB007268, 2022.

1365   Pagnone, A., Völker, C., and Ye, Y.: Processes affecting dissolved iron across the Subtropical North Atlantic: a model study, Ocean Dynamics, 69, 989–1007, https://doi.org/10.1007/s10236-019-01288-w, 2019.

Parekh, P., Follows, M. J., and E., B.: Modeling the global ocean iron cycle, Global Biogeochem. Cycles, 18, GB1002, https://doi.org/doi:10.1029/2003GB002061, 2004.

Pradhan, H. K., Völker, C., Losa, S. N., Bracher, A., and Nerger, L.: Assimilation of Global Total Chlorophyll OC-CCI Data and Its Impact on

1370   Individual Phytoplankton Fields, Journal of Geophysical Research: Oceans, 124, 470–490, https://doi.org/10.1029/2018JC014329, 2019.

Prowe, A. F., Pahlow, M., Dutkiewicz, S., Follows, M., and Oschlies, A.: Top-down control of marine phytoplankton diversity in a global ecosystem model, Progress in Oceanography, 101, 1–13, https://doi.org/https://doi.org/10.1016/j.pocean.2011.11.016, 2012.

Raven, J. A.: The iron and molybdenum use efficiencies of plant growth with different energy, carbon and nitrogen sources, New Phytologist, 109, 279–287, 1988.

1375   Redfield, A., Ketchum, B., and Richards, F.: The influence of organisms on the composition of sea water, in: The Sea, edited by Hill, M., vol. 2, pp. 26–77, Interscience, 1963.

Redi, M.: Oceanic Isopycnal Mixing by Coordinate Rotation, J. Phys. Oceanogr., 12, 1154–1158, 1982.

Regnier, P., Resplandy, L., Najjar, R. G., and Ciais, P.: The land-to-ocean loops of the global carbon cycle, Nature, 603, 401–410, https://doi.org/10.1038/s41586-021-04339-9, 2022.

1380   Resplandy, L., Keeling, R. F., Roedenbeck, C., Stephens, B. B., Khatiwala, S., Rodgers, K. B., Long, M. C., Bopp, L., and Tans, P. P.: Revision of global carbon fluxes based on a reassessment of oceanic and riverine carbon transport, Nature Geoscience, 11, 504–509, https://doi.org/10.1038/s41561-018-0151-3, 2018.

Rohr, T., Richardson, A. J., Lenton, A., and Shadwick, E.: Recommendations for the formulation of grazing in marine biogeochemical and ecosystem models, Progress in Oceanography, 208, 102 878, https://doi.org/10.1016/j.pocean.2022.102878, 2022.

1385   Sabine, C. L., Feely, R. A., Gruber, N., Key, R. M., Lee, K., Bullister, J. L., Wanninkhof, R., Wong, C. S., Wallace, D. W. R., Tilbrook, B., Millero, F. J., Peng, T.-H., Kozyr, A., Ono, T., and Rios, A. F.: The Oceanic Sink for Anthropogenic CO_2, Science, 305, 367–371, https://doi.org/10.1126/science.1097403, 2004.

Sarmiento, J. . L. and Gruber, N.: Ocean Biogeochemical Dynamics, Princeton University Press, Princeton, NJ, 2006.

Sathyendranath, S., Brewin, R. J., Brockmann, C., Brotas, V., Calton, B., Chuprin, A., Cipollini, P., Couto, A. B., Dingle, J., Doerffer, R.,

1390   Donlon, C., Dowell, M., Farman, A., Grant, M., Groom, S., Horseman, A., Jackson, T., Krasemann, H., Lavender, S., Martinez-Vicente, V., Mazeran, C., Mélin, F., Moore, T. S., Müller, D., Regner, P., Roy, S., Steele, C. J., Steinmetz, F., Swinton, J., Taberner, M., Thompson, A., Valente, A., Zühlke, M., Brando, V. E., Feng, H., Feldman, G., Franz, B. A., Frouin, R., Gould, R. W., Hooker, S. B., Kahru, M., Kratzer, S., Mitchell, B. G., Muller-Karger, F. E., Sosik, H. M., Voss, K. J., Werdell, J., and Platt, T.: An Ocean-Colour Time Series for Use in Climate Studies: The Experience of the Ocean-Colour Climate Change Initiative (OC-CCI), Sensors, 19, https://doi.org/10.3390/s19194285, 2019.

1395   Scaife, A. A., Copsey, D., Gordon, C., Harris, C., Hinton, T., Keeley, S., O'Neill, A., Roberts, M., and Williams, K.: Improved Atlantic winter blocking in a climate model, Geophysical Research Letters, 38, https://doi.org/https://doi.org/10.1029/2011GL049573, 2011.

Schartau, M., Engel, A., Schröter, J., Thoms, S., Völker, C., and Wolf-Gladrow, D.: Modelling carbon overconsumption and the formation of extracellular particulate organic carbon, Biogeosciences, 4, 433–454, https://doi.org/10.5194/bg-4-433-2007, 2007.

Schlitzer, R.: Carbon export fluxes in the Southern Ocean: results from inverse modeling and comparison with satellite-based estimates, Deep

1400   Sea Research Part II: Topical Studies in Oceanography, 49, 1623–1644, https://doi.org/https://doi.org/10.1016/S0967-0645(02)00004-8, the Southern Ocean I: Climatic Changes in the Cycle of Carbon in the Southern Ocean, 2002.

Schlitzer, R.: Export Production in the Equatorial and North Pacific Derived from Dissolved Oxygen, Nutrient and Carbon Data, Journal of
Oceanography, 60, 53–62, https://doi.org/10.1023/B:JOCE.0000038318.38916.e6, 2004.

Schlitzer, R., Anderson, R. F., Dodas, E. M., Lohan, M. C., Geibert, W., Tagliabue, A., Bowie, A. R., Jeandel, C., Maldonado, M. T., Landing,
W. M., Cockwell, D., Abadie, C., Abouchami, W., Achterberg, E. P., Agather, A. M., Aguilar-Islas, A. M., van Aken, H. M., Andersen,
M., Archer, C., Auro, M., de Baar, H. J. W., Baars, O., Baker, A. R., Bakker, K., Basak, C., Baskaran, M., Bates, N. R., Bauch, D., van
Beek, P., Behrens, M. K., Black, E., Bluhm, K., Bopp, L., Bouman, H. A., Bowman, K., Bown, J., Boyd, P. W., Boye, M., Boyle, E. A.,
Branellec, P., Bridgestock, L., Brissebrat, G., Browning, T. J., Bruland, K. W., Brumsack, H. J., Brzezinski, M. A., Buck, C. S., Buck,
K. N., Buesseler, K. O., Bull, A., Butler, E., Cai, P., Mor, P. C., Cardinal, D., Carlson, C., Carrasco, G., Casacuberta, N., Casciotti, K. L.,
Castrillejo, M., Chamizo, E., Chance, R., Charette, M. A., Chaves, J. E., Cheng, H., Chever, F., Christl, M., Church, T. M., Closset, I.,
Colman, A., Conway, T. M., Cossa, D., Croot, P. L., Cullen, J. T., Cutter, G. A., Daniels, C., Dehairs, F., Deng, F., Dieu, H. T., Duggan,
B., Dulaquais, G., Dumousseaud, C., Echegoyen-Sanz, Y., Edwards, R. L., Ellwood, M., Fahrbach, E., Fitzsimmons, J. N., Russell Flegal,
A., Fleisher, M. Q., van de Flierdt, T., Frank, M., Friedrich, J., Fripiat, F., Fröllje, H., Galer, S. J., Gamo, T., Ganeshram, R. S., Garcia-
Orellana, J., Garcia-Solsona, E., Gault-Ringold, M., George, E., Gerringa, L. J., Gilbert, M., Godoy, J. M., Goldstein, S. L., Gonzalez,
S. R., Grissom, K., Hammerschmidt, C., Hartman, A., Hassler, C. S., Hathorne, E. C., Hatta, M., Hawco, N., Hayes, C. T., Heimbürger,
L. E., Helgoe, J., Heller, M., Henderson, G. M., Henderson, P. B., van Heuven, S. M. A. C., Ho, P., Horner, T. J., Hsieh, Y. T., Huang,
K. F., Humphreys, M. P., Isshiki, K., Jacquot, J. E., Janssen, D. J., Jenkins, W. J., John, S., Jones, E. M., Jones, J. L., Kadko, D. C., Kayser,
R., Kenna, T. C., Khondoker, R., Kim, T., Kipp, L., Klar, J. K., Klunder, M. B., Kretschmer, S., Kumamoto, Y., Laan, P., Labatut, M.,
Lacan, F., Lam, P. J., Lambelet, M., Lamborg, C. H., Le Moigne, F. A., Le Roy, E., Lechtenfeld, O. J., Lee, J. M., Lherminier, P., Little,
S., López-Lora, M., Lu, Y., Masque, P., Mawji, E., Mcclain, C. R., Measures, C., Mehic, S., Barraqueta, J. L. M., van der Merwe, P.,
Middag, R., Mieruch, S., Milne, A., Minami, T., Moffett, J. W., Moncoiffe, G., Moore, W. S., Morris, P. J., Morton, P. L., Nakaguchi, Y.,
Nakayama, N., Niedermiller, J., Nishioka, J., Nishiuchi, A., Noble, A. E., Obata, H., Ober, S., Ohnemus, D. C., van Ooijen, J., O'Sullivan,
J., Owens, S., Pahnke, K., Paul, M., Pavia, F., Pena, L. D., Peters, B. D., Planchon, F., Planquette, H. F., Pradoux, C., Puigcorbé, V.,
Quay, P., Queroue, F., Radic, A., Rauschenberg, S., Rehkämper, M., Rember, R., Remenyi, T. A., Resing, J. A., Rickli, J., Rigaud, S.,
Rijkenberg, M. J. A., Rintoul, S., Robinson, L. F., Roca-Martí, M., Rodellas, V., Roeske, T., Rolison, J. M., Rosenberg, M., Roshan, S.,
Rutgers van der Loeff, M. M., Ryabenko, E., Saito, M. A., Salt, L. A., Sanial, V., Sarthou, G., Schallenberg, C., Schauer, U., Scher, H.,
Schlosser, C., Schnetger, B., Scott, P., Sedwick, P. N., Semiletov, I., Shelley, R., Sherrell, R. M., Shiller, A. M., Sigman, D. M., Singh,
S. K., Slagter, H. A., Slater, E., Smethie, W. M., Snaith, H., Sohrin, Y., Sohst, B., Sonke, J. E., Speich, S., Steinfeldt, R., Stewart, G.,
Stichel, T., Stirling, C. H., Stutsman, J., Swarr, G. J., Swift, J. H., Thomas, A., Thorne, K., Till, C. P., Till, R., Townsend, A. T., Townsend,
E., Tuerena, R., Twining, B. S., Vance, D., Velazquez, S., Venchiarutti, C., Villa-Alfageme, M., Vivancos, S. M., Voelker, A. H., Wake,
B. D., Warner, M. J., Watson, R., van Weerlee, E., Alexandra Weigand, M., Weinstein, Y., Weiss, D. J., Wisotzki, A., Woodward, E. M. S.,
Wu, J., Wu, Y., Wuttig, K., Wyatt, N. J., Xiang, Y., Xie, R. C., Xue, Z., Yoshikawa, H., Zhang, J., Zhang, P., Zhao, Y., Zheng, L., Zheng,
X. Y., Zieringer, M., Zimmer, L. A., Ziveri, P., Zunino, P., and Zurbrick, C.: The GEOTRACES Intermediate Data Product 2017, Chemical
Geology, 493, 210–223, https://doi.org/10.1016/j.chemgeo.2018.05.040, publisher: Elsevier, 2018.

Schmidtko, S., Stramma, L., and Visbeck, M.: Decline in global oceanic oxygen content during the past five decades, Nature, 542, 335–339,
https://doi.org/10.1038/nature21399, 2017.

Schneider, B., Bopp, L., Gehlen, M., Segschneider, J., Frölicher, T. L., Cadule, P., Friedlingstein, P., Doney, S. C., Behrenfeld, M. J., and
Joos, F.: Climate-induced interannual variability of marine primary and export production in three global coupled climate carbon cycle
models, Biogeosciences, 5, 597–614, https://doi.org/10.5194/bg-5-597-2008, 2008.

1440   Scholz, P., Sidorenko, D., Gurses, O., Danilov, S., Koldunov, N., Wang, Q., Sein, D., Smolentseva, M., Rakowsky, N., and Jung, T.: Assessment of the Finite-volumE Sea ice-Ocean Model (FESOM2.0) – Part 1: Description of selected key model elements and comparison to its predecessor version, Geoscientific Model Development, 12, 4875–4899, https://doi.org/10.5194/gmd-12-4875-2019, 2019.

Scholz, P., Sidorenko, D., Danilov, S., Wang, Q., Koldunov, N., Sein, D., and Jung, T.: Assessment of the Finite VolumE Sea Ice Ocean Model (FESOM2.0), Part II: Partial bottom cells, embedded sea ice and vertical mixing library CVMIX, Geoscientific Model Development

1445   Discussions, 2021, 1–42, https://doi.org/10.5194/gmd-2021-94, 2021.

Schourup-Kristensen, V., Sidorenko, D., Wolf-Gladrow, D. A., and Völker, C.: A skill assessment of the biogeochemical model REcoM2 coupled to the Finite Element Sea-Ice Ocean Model (FESOM 1.3), Geosci. Model Dev., 7, 2769–2802, https://doi.org/10.5194/gmd-7-2769-2014, 2014.

Schourup-Kristensen, V., Wekerle, C., Wolf-Gladrow, D. A., and Völker, C.: Arctic Ocean biogeochemistry in the high resolution FESOM

1450   1.4-REcoM2 model, Progress in Oceanography, 168, 65–81, https://doi.org/10.1016/j.pocean.2018.09.006, 2018.

Séférian, R., Gehlen, M., Bopp, L., Resplandy, L., Orr, J. C., Marti, O., Dunne, J. P., Christian, J. R., Doney, S. C., Ilyina, T., Lindsay, K., Halloran, P. R., Heinze, C., Segschneider, J., Tjiputra, J., Aumont, O., and Romanou, A.: Inconsistent strategies to spin up models in CMIP5: implications for ocean biogeochemical model performance assessment, Geoscientific Model Development, 9, 1827–1851, https://doi.org/10.5194/gmd-9-1827-2016, 2016.

1455   Seifert, M., Nissen, C., Rost, B., and Hauck, J.: Cascading effects augment the direct impact of CO2 on phytoplankton growth in a biogeochemical model, Elementa: Science of the Anthropocene, 10, https://doi.org/10.1525/elementa.2021.00104, 00104, 2022.

Sidorenko, D., Rackow, T., Jung, T., Semmler, T., Barbi, D., Danilov, S., Dethloff, K., Dorn, W., Fieg, K., Gößling, H. F., et al.: Towards multi-resolution global climate modeling with ECHAM6–FESOM. Part I: model formulation and mean climate, Climate Dynamics, 44, 757–780, https://doi.org/10.1007/s00382-014-2290-6, 2015.

1460   Siegel, D. A., Buesseler, K. O., Doney, S. C., Sailley, S. F., Behrenfeld, M. J., and Boyd, P. W.: Global assessment of ocean carbon export by combining satellite observations and food-web models, Global Biogeochem. Cycles, 28, 181–196, https://doi.org/doi:10.1002/2013GB004743, 2014.

Steele, M., Morley, R., and Ermold, W.: PHC: a global ocean hydrography with a high-quality Arctic Ocean, J. Climate, 14, 2079–2087, https://doi.org/10.1175/1520-0442(2001)014<2079:PAGOHW>2.0.CO;2, 2001.

1465   Stewart, K., Kim, W., Urakawa, S., Hogg, A., Yeager, S., Tsujino, H., Nakano, H., Kiss, A., and Danabasoglu, G.: JRA55-do-based repeat year forcing datasets for driving ocean–sea-ice models, Ocean Modelling, 147, 101 557, https://doi.org/https://doi.org/10.1016/j.ocemod.2019.101557, 2020.

Storkey, D., Blaker, A. T., Mathiot, P., Megann, A., Aksenov, Y., Blockley, E. W., Calvert, D., Graham, T., Hewitt, H. T., Hyder, P., Kuhlbrodt, T., Rae, J. G. L., and Sinha, B.: UK Global Ocean GO6 and GO7: a traceable hierarchy of model resolutions, Geoscientific Model

1470   Development, 11, 3187–3213, https://doi.org/10.5194/gmd-11-3187-2018, 2018.

Sundquist, E. T.: Geological Perspectives on Carbon Dioxide and the Carbon Cycle, pp. 55–59, American Geophysical Union (AGU), https://doi.org/https://doi.org/10.1029/GM032p0005, 1985.

Sutton, A. J., Williams, N. L., and Tilbrook, B.: Constraining Southern Ocean CO2 flux uncertainty using uncrewed surface vehicle observations., Geophysical Research Letters, 48, e2020GL091 748, https://doi.org/10.1029/2020GL091748, 2021.

1475   Séférian, R., Berthet, S., Yool, A., Palmiéri, J., Bopp, L., Tagliabue, A., Kwiatkowski, L., Aumont, O., Christian, J., Dunne, J., Gehlen, M., Ilyina, T., John, J. G., Li, H., Long, M. C., Luo, J. Y., Nakano, H., Romanou, A., Schwinger, J., Stock, C., Santana-Falcón, Y., Takano, Y.,

Tjiputra, J., Tsujino, H., Watanabe, M., Wu, T., Wu, F., and Yamamoto, A.: Tracking Improvement in Simulated Marine Biogeochemistry Between CMIP5 and CMIP6, Current Climate Change Reports, 6, 95–119, https://doi.org/10.1007/s40641-020-00160-0, 2020.

Tagliabue, A. and Völker, C.: Towards accounting for dissolved iron speciation in global ocean models, Biogeosciences, 8, 3025–3039, https://doi.org/10.5194/bg-8-3025-2011, 2011.

Tagliabue, A., Mtshali, T., Aumont, O., Bowie, A. R., Klunder, M. B., Roychoudhury, A. N., and Swart, S.: A global compilation of dissolved iron measurements: focus on distributions and processes in the Southern Ocean, Biogeosciences, 9, 1–17, https://doi.org/10.5194/bg-9-1-2012, 2012.

Tagliabue, A., Aumont, O., DeAth, R., Dunne, J. P., Dutkiewicz, S., Galbraith, E., Misumi, K., Moore, J. K., Ridgwell, A. J., Sherman, E., Stock, C. A., Vichi, M., Völker, C., and Yool, A.: How well do global ocean biogeochemistry models simulate dissolved iron distributions?, Global Biogeochemical Cycles, 30, https://doi.org/10.1002/2015GB005289, 2016.

Tagliabue, A., Kwiatkowski, L., Bopp, L., Butenschön, M., Cheung, W., Lengaigne, M., and Vialard, J.: Persistent Uncertainties in Ocean Net Primary Production Climate Change Projections at Regional Scales Raise Challenges for Assessing Impacts on Ecosystem Services, Frontiers in Climate, 3, 738 224, https://doi.org/10.3389/fclim.2021.738224, 2021.

Takahashi, T., Sutherland, S. C., Wanninkhof, R., Sweeney, C., Feely, R. A., Chipman, D. W., Hales, B., Friederich, G., Chavez, F., Sabine, C., Watson, A., Bakker, D. C., Schuster, U., Metzl, N., Yoshikawa-Inoue, H., Ishii, M., Midorikawa, T., Nojiri, Y., Körtzinger, A., Steinhoff, T., Hoppema, M., Olafsson, J., Arnarson, T. S., Tilbrook, B., Johannessen, T., Olsen, A., Bellerby, R., Wong, C., Delille, B., Bates, N., and de Baar, H. J.: Climatological mean and decadal change in surface ocean pCO2, and net sea–air CO2 flux over the global oceans, Deep Sea Research Part II: Topical Studies in Oceanography, 56, 554–577, https://doi.org/10.1016/j.dsr2.2008.12.009, 2009.

Taylor, M. H., Losch, M., and Bracher, A.: On the drivers of phytoplankton blooms in the Antarctic marginal ice zone: A modeling approach, Journal of Geophysical Research, 118, 63–75, https://doi.org/doi:10.1029/2012JC008418, 2013.

Timmermann, R. and Beckmann, A.: Parameterization of vertical mixing in the Weddell Sea, Ocean Modelling, 6, 83–100, https://doi.org/10.1016/S1463-5003(02)0061-6, 2004.

Timmermann, R., Danilov, S., Schröter, J., Böning, C., Sidorenko, D., and Rollenhagen, K.: Ocean circulation and sea ice distribution in a finite element global sea ice–ocean model, Ocean Modelling, 27, 114–129, https://doi.org/https://doi.org/10.1016/j.ocemod.2008.10.009, 2009.

Timmermann, R., Wang, Q., and Hellmer, H.: Ice-shelf basal melting in a global finite-element sea-ice/ice-shelf/ocean model, Annals of Glaciology, 53, 303–314, https://doi.org/10.3189/2012AoG60A156, 2012.

Tjiputra, J. F., Schwinger, J., Bentsen, M., Morée, A. L., Gao, S., Bethke, I., Heinze, C., Goris, N., Gupta, A., He, Y.-C., Olivié, D., Seland, Ø., and Schulz, M.: Ocean biogeochemistry in the Norwegian Earth System Model version 2 (NorESM2), Geoscientific Model Development, 13, 2393–2431, https://doi.org/10.5194/gmd-13-2393-2020, 2020.

Tohjima, Y., Mukai, H., Machida, T., Hoshina, Y., and Nakaoka, S.-I.: Global carbon budgets estimated from atmospheric O_2/N_2 and CO_2 observations in the western Pacific region over a 15-year period, Atmospheric Chemistry and Physics, 19, 9269–9285, https://doi.org/10.5194/acp-19-9269-2019, 2019.

Tréguer, P. J., Sutton, J. N., Brzezinski, M., Charette, M. A., Devries, T., Dutkiewicz, S., Ehlert, C., Hawkings, J., Leynaert, A., Liu, S. M., Llopis Monferrer, N., López-Acosta, M., Maldonado, M., Rahman, S., Ran, L., and Rouxel, O.: Reviews and syntheses: The biogeochemical cycle of silicon in the modern ocean, Biogeosciences, 18, 1269–1289, https://doi.org/10.5194/bg-18-1269-2021, 2021.

Tsujino, H., Urakawa, S., Nakano, H., Small, R. J., Kim, W. M., Yeager, S. G., Danabasoglu, G., Suzuki, T., Bamber, J. L., Bentsen, M., Böning, C. W., Bozec, A., Chassignet, E. P., Curchitser, E., Boeira Dias, F., Durack, P. J., Griffies, S. M., Harada, Y., Ilicak, M., Josey,

S. A., Kobayashi, C., Kobayashi, S., Komuro, Y., Large, W. G., Le Sommer, J., Marsland, S. J., Masina, S., Scheinert, M., Tomita, H.,
Valdivieso, M., and Yamazaki, D.: JRA-55 based surface dataset for driving ocean–sea-ice models (JRA55-do), Ocean Modelling, 130,
79–139, https://doi.org/https://doi.org/10.1016/j.ocemod.2018.07.002, 2018.

Völker, C. and Tagliabue, A.: Modeling organic iron-binding ligands in a three-dimensional biogeochemical ocean model, Marine Chemistry,
173, 67–77, https://doi.org/10.1016/j.marchem.2014.11.008, 2015.

Völker, C. and Köhler, P.: Responses of ocean circulation and carbon cycle to changes in the position of the Southern Hemisphere westerlies
at Last Glacial Maximum, Paleoceanography, 28, 726–739, https://doi.org/https://doi.org/10.1002/2013PA002556, 2013.

Waite, A. M., Thompson, P. A., and Harrison, P. J.: Does energy control the sinking rates of marine diatoms?, Limnology and Oceanography,
37, 468–477, https://doi.org/https://doi.org/10.4319/lo.1992.37.3.0468, 1992.

Wang, Q., Danilov, S., Sidorenko, D., Timmermann, R., Wekerle, C., Wang, X., Jung, T., and Schröter, J.: The Finite Element Sea Ice-Ocean
Model (FESOM) v.1.4: formulation of an ocean general circulation model, Geosci. Model Dev., 7, 663–693, https://doi.org/10.5194/gmd-
7-663-2014, 2014.

Wanninkhof, R.: Relationship between wind speed and gas exchange over the ocean revisited, Limnology and Oceanography: Methods, 12,
351–362, https://doi.org/10.4319/lom.2014.12.351, 2014.

Wanninkhof, R., Park, G. H., Takahashi, T., Sweeney, C., Feely, R., Nojiri, Y., Gruber, N., Doney, S. C., McKinley, G. A., Lenton, A.,
Le Quéré, C., Heinze, C., Schwinger, J., Graven, H., and Khatiwala, S.: Global ocean carbon uptake: magnitude, variability and trends,
Biogeosciences, 10, 1983–2000, https://doi.org/10.5194/bg-10-1983-2013, 2013.

Wekerle, C., Wang, Q., Danilov, S., Schourup-Kristensen, V., von Appen, W.-J., and Jung, T.: Atlantic Water in the Nordic Seas: locally
eddy-permitting ocean simulation in a global setup, J. Geophys. Res. Oceans, https://doi.org/10.1002/2016JC012121, 2017.

Westberry, T., Behrenfeld, M. J., Siegel, D. A., and Boss, E.: Carbon-based primary productivity modeling with vertically resolved photoac-
climation, Global Biogeochemical Cycles, 22, GB2024, https://doi.org/doi:10.1029/2007GB003078, 2008.

Wolf-Gladrow, D. A., Zeebe, R. E., Klaas, C., Körtzinger, A., and Dickson, A. G.: Total alkalinity: The ex-
plicit conservative expression and its application to biogeochemical processes, Marine Chemistry, 106, 287–300,
https://doi.org/https://doi.org/10.1016/j.marchem.2007.01.006, special issue: Dedicated to the memory of Professor Roland Wol-
last, 2007.

Yamanaka, Y. and Tajika, E.: The role of the vertical fluxes of particulate organic matter and calcite in the oceanic carbon cycle : Studies using
an ocean biogeochemical general circulation model, Global Biogeochemical Cycles, 10, 361–382, https://doi.org/10.1029/96GB00634,
1996.

Ye, Y. and Völker, C.: On the Role of Dust-Deposited Lithogenic Particles for Iron Cycling in the Tropical and Subtropical Atlantic, Global
Biogeochemical Cycles, 31, 1543–1558, https://doi.org/10.1002/2017GB005663, 2017.

Ye, Y., Völker, C., and Gledhill, M.: Exploring the Iron-Binding Potential of the Ocean Using a Combined pH and DOC Parameteri-
zation, Global Biogeochemical Cycles, 34, e2019GB006 425, https://doi.org/https://doi.org/10.1029/2019GB006425, e2019GB006425
10.1029/2019GB006425, 2020.

Zhang, R. and Vallis, G. K.: The Role of Bottom Vortex Stretching on the Path of the North Atlantic Western Boundary Current and on the
Northern Recirculation Gyre, Journal of Physical Oceanography, 37, 2053 – 2080, https://doi.org/10.1175/JPO3102.1, 2007.